



Skolkovo Institute of Science and Technology

ASSEMBLING NETWORKS OF SINGLE-WALLED CARBON NANOTUBES FOR
ELECTRONIC AND OPTICAL APPLICATIONS

Doctoral Thesis

by

ILYA NOVIKOV

DOCTORAL PROGRAM IN MATERIALS SCIENCE AND ENGINEERING

Supervisor
Professor Albert Nasibulin
Co-supervisors
Professor Tanja Kallio
Assistant Professor Dmitry Krasnikov
Assistant Professor Fedor Fedorov

Moscow - 2023

© Ilya Novikov 2023

I hereby declare that the work presented in this thesis was carried out by myself at Skolkovo Institute of Science and Technology, Moscow, except where due acknowledgement is made, and has not been submitted for any other degree.

Candidate (Ilya Novikov)

Supervisor (Prof. Albert Nasibulin)

Abstract

Single-walled carbon nanotubes (SWCNTs) are unique material with outstanding physical properties, which make them a great candidate for electronic applications. The majority of electronic applications involve SWCNTs in the form of a random network while the performance of the SWCNT networks is determined by structural features of both nanotubes and their ensembles. In particular, high nanotube length (or, aspect ratio) and homogeneity of nanotube spatial distribution result in an increase in SWCNT network conductivity required for their high performance in specific electronic devices. Meanwhile, in the macroscale, SWCNT networks can be realized in (quasi-) two-dimensional (2D) from – thin SWCNT films – and three-dimensional (3D) one assembled within host polymer – SWCNT/polymer nanocomposites. The current thesis is devoted to the controllable fabrication of SWCNT networks with tunable properties for their high performance in electronic and optical applications.

The first direction of the work is devoted to CO-based aerosol chemical vapor deposition (CVD) synthesis of thin SWCNT films (“2D” networks) utilized as transparent conductive films (TCFs). The goal of the research is to improve the performance of SWCNT films as a key component of TCFs (equivalent sheet resistance, R_{90}) and the synthesis productivity (yield). New reactor chemical engineering approaches were developed. The first one is based on controllable adjustment of residence time (τ , by flow rate control) which allows maintaining the catalyst activation stage and varying nanotube growth, this way optimizing R_{90} (51 Ω/\square was achieved for doped films). The second one is related to the introduction of rarely employed H_2 as a reducing agent, which was demonstrated to increase synthesis yield by 15 times. Furthermore, the inversed approach to residence time tuning of R_{90} was used to develop a new methodology for fast evaluation of nanotube growth kinetics based on analysis of R_{90} -vs- τ trends. As a result, the CO_2 (used as a growth promoter) effect on catalyst deactivation rate was first studied.

The second part of the thesis concerns the problems of the 3D organization of SWCNT networks within a polymer. SWCNT/polymer nanocomposites were fabricated using commercial SWCNTs with moderate (~ 3000 aspect ratio). Appropriate

manufacturing techniques allowed for reaching ultralow percolation threshold values: unprecedented 0.006 wt% for elastic SWCNT/polyurethane nanocomposites and 0.001 – 0.003 wt% for SWCNT/epoxy ones. Elastic nanocomposites had state-of-the-art performance in electronic applications (strain sensing and electromagnetic interference shielding) at very low concentrations, which provides strong economic benefits for nanocomposite production, while for thermoset nanocomposites, a new approach to use densely packed briquette-shaped SWCNT powders was proposed, which significantly simplify the nanocomposite manufacturing process.

Publications

1. **Ilya V. Novikov**, Eldar M. Khabushev, Dmitry V. Krasnikov, Anton V. Bubis, Anastasia E. Goldt, Sergey D. Shandakov, and Albert G. Nasibulin. Residence time effect on single-walled carbon nanotube synthesis in an aerosol CVD reactor // *Chemical Engineering Journal* 420 (2021) 129869. DOI: 10.1016/j.cej.2021.129869.
Author's contribution: Fabrication of samples, electrical and optical characterization, data processing, writing the manuscript.
2. **Ilya V. Novikov**, Dmitry V. Krasnikov, Anton M. Vorobei, Yaroslav I. Zuev, Hassaan A. Butt, Fedor S. Fedorov, Sergey A. Guse1, Alexander A. Safonov, Eugene V. Shulga, Stepan D. Konev, Ivan V. Sergeichev, Sergey S. Zhukov, Tanja Kallio, Boris P. Gorshunov, Olga O. Parenago, Albert G. Nasibulin. Multifunctional elastic nanocomposites with extremely low concentrations of single-walled carbon nanotubes // *ACS Applied Materials and Interfaces* 14 (2022) 18866–18876. DOI: 10.1021/acsami.2c01086.
Author's contribution: Fabrication of samples, electrical characterization, data processing, writing the manuscript.
3. Hassaan A. Butt, **Ilya V. Novikov**, Dmitry V. Krasnikov, Artem V. Sulimov, Amit K. Pal, Stanislav A. Evlashin, Anton M. Vorobei, Yaroslav I. Zuev, Dmitry Ostrizhiniy, Dmitry Dzhurinskiy, Yuri A. Popov, Olga O. Parenago, Albert G. Nasibulin. Binder-free, pre-consolidated single-walled carbon nanotubes for manufacturing thermoset nanocomposites // *Carbon* 202 (2023) 450-463. DOI: 10.1016/j.carbon.2022.10.088.

Author's contribution: Fabrication of samples (50%; together with H.A. Butt), electrical characterization (AC conductivity tests, DC conductivity tests (50%; together with H.A. Butt)), data processing (50%, together with H.A. Butt), editing the (original draft was written by H.A. Butt) and writing the part devoted to electrical characterization.

4. Javier A. Ramirez B., Dmitry V. Krasnikov, Vladimir V. Gubarev, **Ilya V. Novikov**, Vladislav A. Kondrashov, Andrei V. Starkov, Mikhail S. Krivokorytov, Vyacheslav V. Medvedev, Yuriy G. Gladush, Albert G. Nasibulin. Renewable single-walled carbon nanotube membranes for extreme ultraviolet pellicle applications // *Carbon* 198 (2023) 364-370. DOI: 10.1016/j.carbon.2022.07.014.

Author's contribution: Synthesis of SWCNTs and optimization of their properties.

5. Tatiana N. Kurtukova, Daria S. Kopylova, Nikita I. Raginov, Eldar M. Khabushev, **Ilya V. Novikov**, Svetlana I. Serebrennikova, Dmitry V. Krasnikov, and Albert G. Nasibulin. Plasma-treated carbon nanotubes for fast infrared bolometers // *Applied Physics Letter* 122 (2023) 093501. DOI: 10.1063/5.0140030.

Author's contribution: Synthesis of SWCNTs and optimization of their properties.

Acknowledgements

The research presented in the thesis would be impossible without many people who contributed to this work. First, I would like to thank my supervisor, Prof. Albert Nasibulin, who guided and motivated me throughout my PhD study, greatly contributed to the development of me as a scientist, and helped me with all the difficulties I faced during my studies. Also, I am grateful to my co-supervisor Prof. Dmitry Krasnikov for creating a highly productive research atmosphere, teaching me how to conduct high-level research, and supporting me in and out of work. I highly appreciate the help provided by my co-supervisors Prof. Tanja Kallio and Prof. Fedor Fedorov, including their valuable advice and ideas which greatly fostered my research progress.

I also would like to express my deep gratitude to my Jury Members and Individual Doctoral Committee for taking care of my thesis and Skoltech for the inspiring research atmosphere.

I am thankful to the Laboratory of Nanomaterials led by Prof. Albert Nasibulin, especially to my colleagues and coauthors Dr. E.M. Khabushev, Mr. H.A. Butt, Mrs. A.R. Bogdanova, Mr. N.I. Raginov, Ms. V.S. Shestakova, Dr. A.E. Goldt, Mr. J.A. Ramirez B., Dr. D.S. Kopylova, Mr. A.V. Bubis, and many others. Besides, I wish to acknowledge the help of my collaborators from different laboratories and institutions, especially Mr. A.M. Vorobei and Prof. O.O. Parenago from IGIC RAS; Dr. M. Mousavihashem from Aalto University; Prof. S.A. Evlashin, Dr. S.A. Gusev, Prof. A.A. Safonov, Dr. S.D. Konev, and Prof. I.V. Sergeichev from Skoltech CMT; Dr. S.S. Zhukov and Prof. B.P. Gorshunov from MIPT.

Last but not least, I would like to thank my family, especially my bride and mother, who supported me all my way as a doctoral student.

The work was supported by Russian Science Foundation Grants 20-73-10256 (mechanism of nanotube growth) and 22-13-00436 (role of hydrogen) and Council on Grants of the President of the Russian Federation grant number HIII-1330.2022.1.3.

Table of Contents

Abstract.....	3
Publications.....	5
Acknowledgements.....	7
Table of Contents.....	9
List of Symbols, Abbreviations	12
Chapter 1. Introduction.....	15
Chapter 2. Networks of single-walled carbon nanotubes	19
2.1. Single-walled carbon nanotubes.....	19
2.1.1. SWCNT structure and electronic nature.....	19
2.1.2. SWCNT networks. Structure-dependent conductivity.....	23
2.2. 2D SWCNT networks – thin films.....	28
2.2.1. SWCNT-based transparent conductive films	28
2.2.2. CNT synthesis. Aerosol chemical vapor deposition method for SWCNT film synthesis	31
2.3. 3D networks: SWCNT/polymer nanocomposites.....	36
2.3.1. SWCNT/polymer nanocomposites: percolation threshold, conductivity, and prospects for electronic applications.....	36
2.3.2. Fabrication of CNT/polymer nanocomposites. CNT dispersion degree.....	42
2.4. Summary: general routs on optimization of SWCNT networks for electronic applications	45

Chapter 3. Methods.....	47
3.1. Material synthesis and fabrication.....	47
3.1.1. CO-based aerosol CVD synthesis of SWCNTs	47
3.1.2. Fabrication of SWCNT/polymer nanocomposites	51
3.2. Conductivity tests.....	55
3.2.1. Sheet resistance of SWCNT film	55
3.2.2. Nanocomposite conductivity. Impedance spectroscopy.....	57
3.3. Optical characterization.....	58
3.3.1. Optical absorbance spectroscopy.....	58
3.3.2. Raman spectroscopy	60
3.4. Electron microscopy.....	63
3.4.1. Scanning electron microscopy	63
3.4.2. Transmission electron microscopy	64
3.5. Tensile tests and mechanical sensitivity measurements for elastic nanocomposites.....	64
3.6. THz spectroscopy for EMI-shielding efficiency estimation	65
Chapter 4. Aerosol CVD synthesis of SWCNT films.....	66
4.1. Chemical engineering of CO-based aerosol CVD reactor	66
4.1.1. Residence time control to tune the properties of SWCNT films.....	66
4.1.2. Boosting the synthesis with hydrogen	76
4.2. Fast evaluation of nanotube growth kinetics.....	88
Chapter 5. Fabrication of SWCNT/polymer nanocomposites	98

5.1. Multifunctional elastic SWCNT/TPU nanocomposites	98
5.2. Nanotube bulk density optimization for SWCNT/thermoset nanocomposites	110
Chapter 6. Conclusions	116
Bibliography	119
Appendices.....	135
Appendix 1. Bundling degree dependency on number of nanotubes and residence time	
135	
Appendix 2. Thermodynamic calculations for CO/H ₂ atmosphere.	136
Appendix 3. Effects of nitrogen and residence time in H ₂ -assisted aerosol CVD	
nanotube synthesis.	141
Appendix 4. Supporting figures for nanotube kinetics evaluation study	142
Appendix 5. Supporting figures for the investigation of SWCNT/polymer	
nanocomposites.....	147

List of Symbols, Abbreviations

0D – zero-dimensional

1D – one-dimensional

2D – two-dimensional

3D – three-dimensional

AC – alternative current

BET – Brauner-Emmett-Teller method

BWF – Breit-Wigner-Fano

CFD – computational fluid dynamics

CNT – carbon nanotube

CP – coagulation precipitation

CVD – chemical vapor deposition

DC – direct current

DMA – differential mobility analyzer

DMSO – dimethyl sulfoxide

EMI – electromagnetic interference

GF – gauge factor

high-T – high-temperature (regime)

ITO – indium tin oxide

low-T – low-temperature (regime)

MB – masterbatch

MFC – mass flow controller

m-SWCNT – metallic single-walled carbon nanotube

MWCNT – multiwalled carbon nanotube

NIPS – nonsolvent induced phase separation

NIR – near-infrared

NP – nanoparticle

OLED – organic light-emitting diode

RBM – radial breathing mode

RESS – rapid expansion of supercritical suspensions

SEM – scanning electron microscopy

s-SWCNT – semiconductive single-walled carbon nanotube

STM – scanning tunnelling microscopy

SWCNT – single-walled carbon nanotube

TCF – transparent conductive films

TEM – transmission electron microscopy

TPU – thermoplastic polyurethane

UV – ultraviolet

vis – visible

c_{CO_2} – carbon dioxide volumetric concentration

c_{H_2} – hydrogen volumetric concentration

d – nanotube diameter

I_G/I_D – ratio of Raman G and D mode intensities

L – nanotube/bundle length

R_{90} – equivalent sheet resistance

S_{11} , S_{22} , M_{11} , *etc.* – transitions between van Hove singularities in SWCNTs

τ – residence time

φ_c – percolation threshold

Chapter 1. Introduction

Raising the quality of life is an everlasting and growing human demand, which is impossible without scientific and technological progress. This tendency in combination with the growing human population and limited planet resources pushes researchers worldwide for the development of new materials, which might allow this rapid technological advancement. Meanwhile, nanotechnologies and nanomaterials are highly promising for this purpose. Together with innovations in energy and biomedical fields, nanomaterials are capable to begin a new chapter in technologies for modern electronic and optical devices, including those accompanying a person daily. Meanwhile, carbon nanotubes (CNTs) may be regarded as one of the most encouraging representatives of nanomaterials for electronic and optical applications.

Carbon nanotubes were re-discovered soon after the fullerene appearance and resonated in the broad scientific community immediately. Although the first mentions of rod-shaped hollow carbon structures in the nanometer range date back to the 50s-70s (first observations of such structures were reported by Radushkevich and Lukyanovich in 1952) [1,2], it was Sumio Iijima who first attracted much attention to this nanoobject [3]. After his famous publication, carbon nanotubes became an extremely popular investigation object for researchers from different fields of physics and chemistry. The nineties and early two-thousands are deservedly considered a golden age in the development of carbon nanotubes. Especial attention was paid to single-walled CNTs (SWCNTs), mainly, because of their unique physical properties, such as exceptionally high electrical and thermal conductivity, outstanding mechanical properties implying very high Young's modulus and

tensile strength, extremely high specific surface area and aspect ratio (up to 10^8), and some other properties. Moreover, depending on the chirality angle, they can behave either as a semiconductor or as a metal, which is absolutely unique for essentially the same material.

As soon as the enormous potential of SWCNTs in future technologies was realized, researchers switched focus to the practical sides of nanotubes, first and foremost, in electronics. There are plenty of works emphasizing the high applicability of nanotubes in different forms: nanotube forests, for example, as close-to-absolute blackbody absorbers (based on vertically aligned nanotube arrays) [4,5], densely packed fibers as electrodes or reinforcing agents [6,7], or even isolated SWCNTs for biomedical applications [8]. Yet, the majority of electronic applications involve SWCNTs in the form of randomly oriented isotropic networks. This is the way to transfer the unique conductivity and optical properties of SWCNTs to the macroscale. Among the SWCNT network-based macromaterials, thin films and polymer nanocomposites are of great interest.

Because of the combination of conductivity and transparency, thin SWCNT films are great candidates for utilization as transparent conductive films (TCFs), which can be used in liquid-crystal displays, organic light-emitting diodes (OLEDs), touchscreens, solar panels, and some others. Typically, such devices are based on metal-oxide semiconductors, primarily, indium tin oxide (ITO). Nevertheless, its brittleness and depleting resources of indium push researchers to investigate alternative materials, such as the abovementioned SWCNT-based thin films. The most appropriate production method for SWCNT films is the aerosol (a particular case of floating catalyst) chemical vapor deposition (CVD) process since it is a one-stage liquid-free and scalable technique. However, SWCNT films still do

not meet industrial requirements despite their flexibility and potentially high scalability of their production. The moderate performance of SWCNT-based thin films is mainly due to limited control of SWCNT network structural properties during the synthesis process. SWCNT network conductivity was repeatedly shown to be determined by both intra- and inter-nanotube structural features, such as length and diameter distribution, defectiveness, dispersion, and bundling degrees. Thus, tuning the processes of SWCNT synthesis and/or SWCNT-based film fabrication for yielding controllable structural properties is key to the development of SWCNT-based TCFs and their employment in the industry.

A similar problem concerns 3D networks – CNT/polymer nanocomposites. Although nanocomposites are one of the most developed industry fields of nanotubes, their performance in electronic applications, such as mechanical and chemical sensors, antistatic coatings, electromagnetic interference (EMI) shielding devices, *etc.*, is strongly dependent on nanotube dispersibility within a polymer, that is, features of CNT network morphology in a polymer matrix. Adjustment of nanotube networks in a polymer is a complex task related to the nanocomposite fabrication process and depends on many factors, including initial nanotube state and entanglement degree, aspect ratio and defectiveness, and nanotube-polymer interaction. Moreover, a significantly higher share of studies was devoted to polymer nanocomposites based on multi-walled CNTs (MWCNTs), which is mostly explained by their higher availability and believed higher dispersibility. Nonetheless, recent industrial growth of SWCNT production in combination with their fundamentally greater prospects for utilization in polymer associated with their light weight and higher aspect ratio might change this balance and enhance the nanocomposite industry

as a whole. Yet, the problem of SWCNT dispersibility in polymer for effective assembling of SWCNT networks is still a challenging task.

Thus, on the one hand, SWCNTs possess a uniquely broad spectrum of properties that could be applied in various electronic and optical applications. Nevertheless, on the other hand, their remarkable potential has not been reached yet, which is attributed to still insufficiently developed approaches to the synthesis of SWCNTs and assembling their networks. This thesis has an ambitious goal to improve the situation.

The current work is focused on assembling SWCNT networks in (quasi-) 2D and 3D forms. The first half of the work is devoted to the aerosol CVD synthesis of SWCNTs and the development of SWCNT network-based thin films utilized as TCFs. The second half is aimed at the improvement of SWCNT/polymer nanocomposite fabrication methods, where the main attention is paid to the interrelation between SWCNT network morphology, the conductivity of nanocomposites, and their performance in strain sensing and electromagnetic interference (EMI) shielding.

Chapter 2. Networks of single-walled carbon nanotubes

2.1. Single-walled carbon nanotubes

2.1.1. SWCNT structure and electronic nature

Carbon nanomaterials as materials based on carbon where a single unit at least in one dimension is sized between 1 and 100 nm traditionally include fullerenes as a zero-dimensional (0D) nanoobject, carbon nanotubes as a one-dimensional (1D) nanoobject, and graphene as a two-dimensional (2D) nanoobject. These nanomaterials are based on a hexagonal honeycomb crystal lattice constructed from sp^2 -hybridized carbon atoms. sp^2 -hybridization results in π -electron conjugation determining the unique conductivity nature of carbon nanomaterials. This π -conjugated structure is responsible for graphite conductivity.

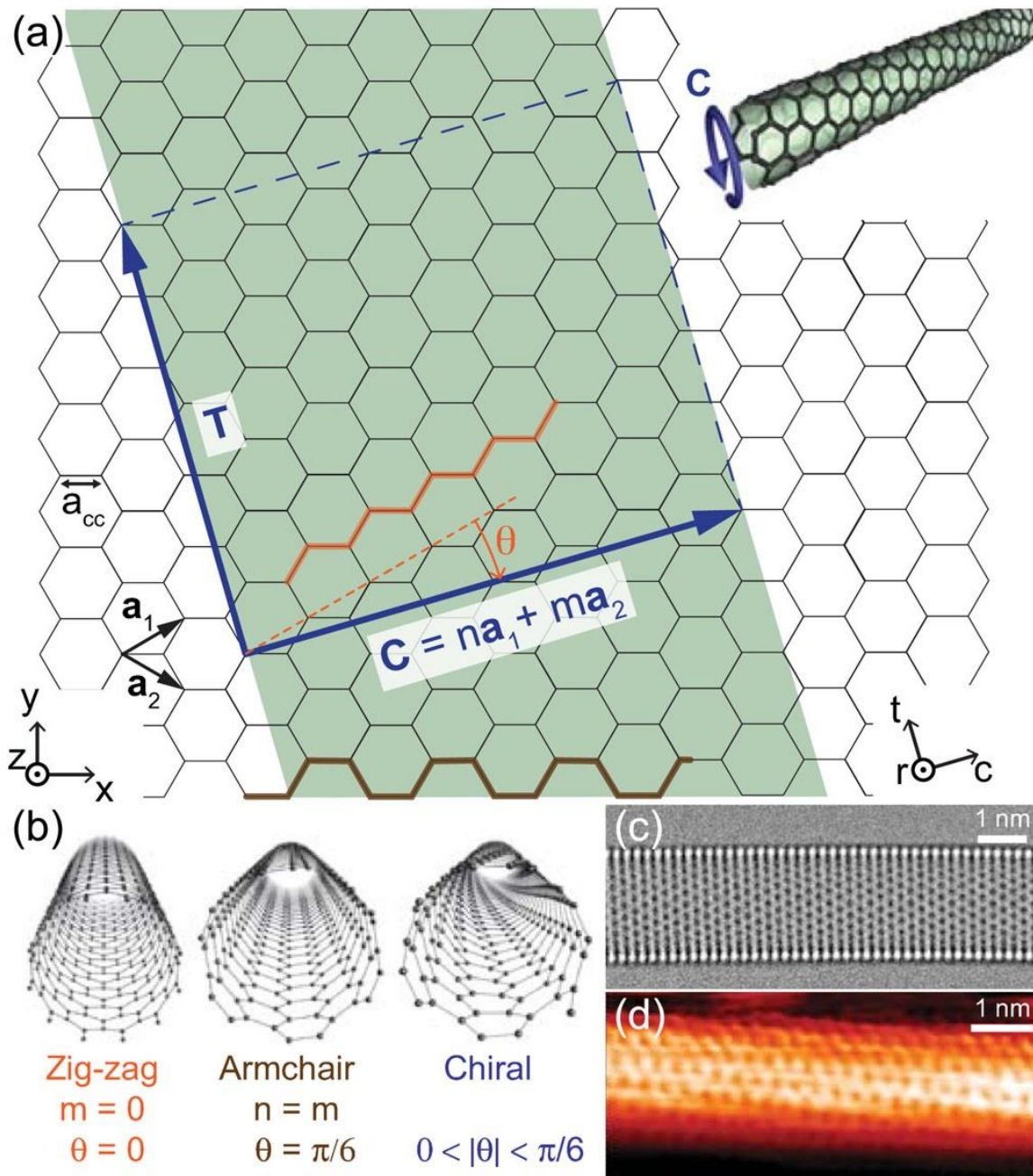


Figure 1. Illustration of the structure of (a) graphene honeycomb crystal lattice with specified chirality vector \vec{C} , primitive lattice translation vectors \vec{a}_1 and \vec{a}_2 , and carbon-carbon distance a_{C-C} ; the inset in upper right corner represents rolling a graphene sheet along a vector \vec{C} ; (b) nanotubes with different chirality: zig-zag, armchair, and chiral; typical high-resolution (c) TEM and (d) STM images of SWCNTs. Reused with permission from [9]. Copyright (2015) by the American Physical Society.

Description of carbon nanomaterial structure is logical to start with graphene - 2D allotrope modification of carbon representing single-layer hexagonal lattice (although it was discovered last [10]) (**Figure 1a**). This structure leads to its unique electronic structure: graphene is a zero-gap semiconductor with linear energy dispersion relation in which valence and conduction bands meet at the Dirac point. Nevertheless, the electronic properties of carbon nanotubes are even more exotic.

SWCNT is traditionally represented as a graphene sheet that is rolled in a hollow cylinder along one of the Bravais lattice vectors (**Figure 1**). Definitely, nanotubes cannot be obtained by rolling graphene, which will be discussed below, however, graphene crystal lattice is useful for nanotube structure characterization. The direction of this vector \vec{C}_h determines chiral angle, or, chirality (**Figure 1**) of nanotubes:

$$\vec{C}_h = n\vec{a}_1 + m\vec{a}_2, \quad (1)$$

where \vec{a}_1 and \vec{a}_2 are primitive lattice translation vectors, and the pair of integer coordinates (n, m) are nanotube chiral indices or chirality. Chiral indices determine nanotube diameter and chiral angle:

$$d = \frac{L_c}{\pi} = \frac{a}{\pi} \sqrt{n^2 + nm + m^2}, \quad (2)$$

$$\theta = \tan^{-1} \frac{\sqrt{3}m}{2n + m}, \quad (3)$$

where L_c is a nanotube circumference and $a = |\vec{a}_i| = \sqrt{3}a_{c-c} = 2.46 \text{ \AA}$ ($a_{c-c} = 1.421 \text{ \AA}$ is the carbon-carbon distance in graphene hexagonal lattice). Traditionally, nanotubes with $\theta = 0^\circ$ (or, when $m = 0$) are called “zig-zag” nanotubes, nanotubes with $\theta = 30^\circ$ (or, when $m = n$) – “armchair” nanotubes, and intermediate case with $0^\circ < \theta < 30^\circ$ refers to

“chiral” nanotubes (**Figure 1b**) [11]. **Figure 1c-d** represents typical high-resolution transmission electron microscopy (TEM) and scanning tunneling microscopy (STM) images of individual SWCNTs, respectively.

The cylindrical shape of SWCNTs imposes periodic boundary conditions resulting in quantization (a discrete set of possible values) of the circumferentially directed wavevector (perpendicularly to the nanotube axis), which leads to a general 1D energy gap structure and introduces a band gap, the width of which is dependent on the nanotube chirality: if $(n - m) \div 3$, bandgap is zero, the dispersion relation is analogous to graphene and SWCNT is nominally metallic; otherwise, (if $n - m$ is not multiple of 3), SWCNT is semiconductive with a bandgap of a few hundreds of meV [12]. In fact, only nanotubes with armchair chirality are truly metallic while the other “metallic” nanotubes possess a narrow bandgap of ~ 10 meV, which can be neglected at room temperature [9]. Thus, one-third of SWCNTs have metallic conductivity, while the other two-thirds are semiconductors. For more information about the relationship between the geometry of nanotubes and their conductivity, see the reviews by Dresselhaus *et al.* [11] and Laird *et al.* [9].

One-dimensionality of SWCNT band structure results in the appearance of singularities in electron density of states (DOS) known as van Hove singularities peculiar to both semiconducting and metallic nanotubes [13,14]. Spike-like DOS leads to features in optical absorbance spectra caused by interband transitions between van Hove singularities in valence and conduction bands and reflected in pronounced peaks called S_{ii} for semiconducting SWCNTs and M_{ii} for metallic ones, where i refers to the number of

singularities from Fermi energy (discussed in the Methods section). Since, as discussed above, SWCNT band structure is determined by chirality, each nanotube chirality has its specific energy gap values (transition energies) and, hence, positions of S_{ii} and M_{ii} peaks in optical absorbance spectra. Moreover, energy gap values reflected in the transition peak positions were shown to be inversely proportional to SWCNT diameter and can be a useful tool for the characterization of nanotube diameter distribution. The dependency of transition energy S_{ii} and M_{ii} on SWCNT diameter now is known as the Kataura plot [15].

Thus, from the fundamental viewpoint of quantum physics, single-walled carbon nanotubes possess unique electronic and optical properties and, as a result, great prospects for utilization in electronic and optical applications, in the majority of which, SWCNTs are used as a macromaterial often representing a SWCNT random network. Below, features of SWCNT network construction and macro-properties (primarily, electrical conductivity) of SWCNT network arising from inter-tube interaction will be discussed.

2.1.2. SWCNT networks. Structure-dependent conductivity

Usually, a nanotube network is randomly oriented SWCNTs or their bundles (several nanotubes stacked together due to high van der Waals interactions between high-surface-area nanotubes) forming multiple inter-tube junctions. In a simplified form, a SWCNT network can be represented as series-connected resistors, two main types of which are a resistance of SWCNTs themselves R_{CNT} and junction resistance R_j . Thus, overall network resistance R_{net} is determined by these two contributions:

$$R_{net} = R_{CNT} + R_j. \quad (4)$$

Junctions between nanotubes may be classified according to inter-tube distance: with direct physical contact between two nanotubes – contact junction with resistance R_c – and with a small inter-tube gap commensurate with nanotube bundle diameter - tunnel junction with resistance R_t [16]. On average, junction resistance can be interpreted as a parallel connection of these two resistors:

$$\frac{1}{R_j} = \frac{1}{R_c} + \frac{1}{R_t}. \quad (5)$$

The contribution of the latter may be neglected when the SWCNT network is quite densely packed (nanotubes are mainly in physical contact with each other), since R_t exponentially increases with inter-tube distance:

$$R_t = R_0 e^{\alpha s}, \quad (6)$$

where s is inter-tube distance, and parameters R_0 and α depends on the height of the potential barrier above nanotube Fermi level K (assuming its rectangular shape; details can be found in [17]):

$$R_0 = \frac{1}{C_1} \frac{s}{\sqrt{K}}; \quad \alpha = C_2 \sqrt{K}, \quad (7)$$

where constants $C_1 = 3.16 \cdot 10^{10} \frac{\text{\AA}}{\Omega(\text{eV})^{1/2}}$, $C_2 = 1.025 \frac{1}{(\text{eV})^{1/2}}$ for potential barrier K in eV and inter-tube distance s in \AA [18]. Yet, tunneling resistance impact can be crucial when nanotube concentration is low (discussed in the following sections). Thus, for a well-developed (highly interconnected) SWCNT network, the overall resistance R_{net} approaches to:

$$R_{net} \approx R_{CNT} + R_c. \quad (8)$$

Depending on the use purposes (for instance, for polarizers), nanotubes can be aligned, and their electric transport properties become highly anisotropic [19]. Yet, here isotropic structure is out of consideration. **Figure 2** schematically illustrates a random nanotube network with highlighted contributions in overall network resistance.

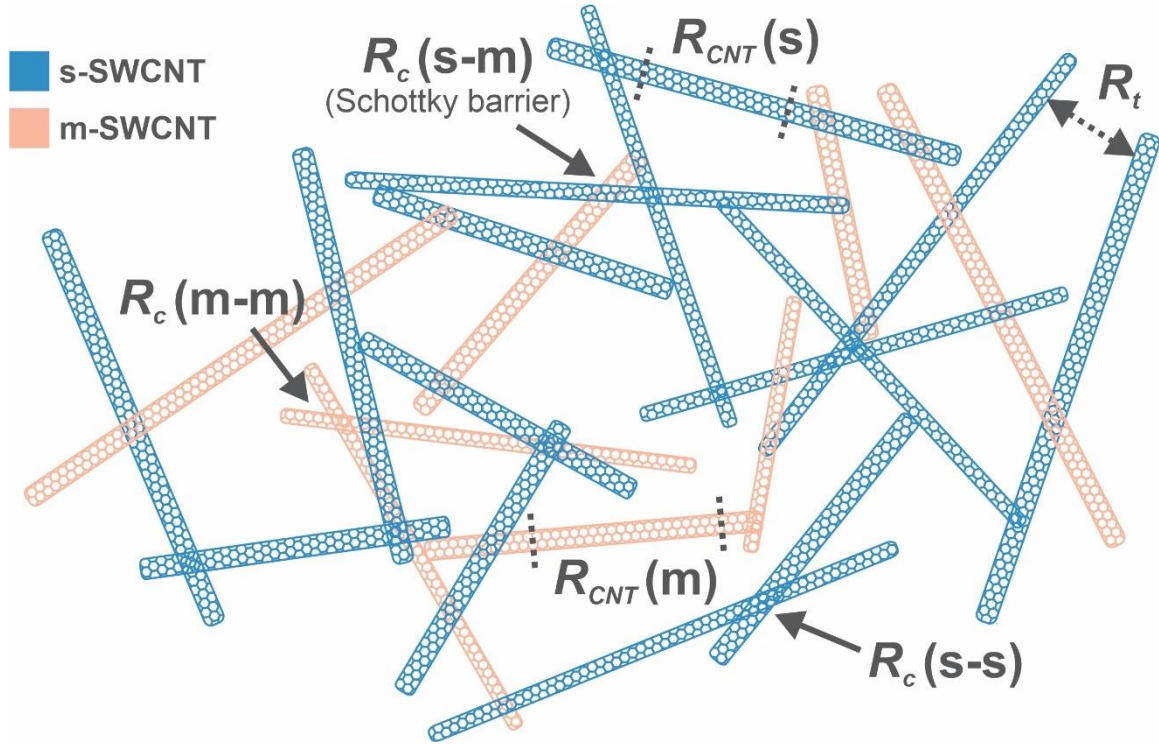


Figure 2. Schematic representation of SWCNT network with emphasized contributions in overall network resistance.

As mentioned above, SWCNTs can be different in diameter and chirality. To date, chirality-pure production of SWCNTs is being actively studied, nonetheless, this development is in its onset [20]. Therefore, typically, a SWCNT sample includes nanotubes with a finite set of diameters and chiralities, that is, in other words, SWCNTs with a certain diameter distribution and, in turn, chirality distribution are considered. As was discussed above, at random distribution, that is, any possible pair of chirality coordinates n and m ,

one third of nanotubes are metallic (m-SWCNTs), and two thirds are semiconductors (s-SWCNTs). For the usual moderate-broad chirality distribution, statistics are similar [21,22]. This leads to features in SWCNT network conductivity.

Resistance of SWCNTs themselves (or, intra-tube resistance R_{CNT}) mainly depends on nanotube chirality (evidently, semiconducting or metallic nature), diameter, and crystallinity. Obviously, m-SWCNT conductivity is higher, while thicker s-SWCNT conducts better as well because of higher charge carrier density caused by smaller bandgap [23]. Defectiveness of SWCNTs (concentration of lattice mismatches, defects in graphitic structure), as well as amorphous carbon impurities, may significantly lower conductivity as such sp^3 -hybridized carbon inclusions interrupt π -conjugated electron structure and scatter charge carriers [24].

Different types of conductors (s- or m-SWCNTs) result in different types of contacts in the SWCNT network with the proportions determined by metallic/semiconducting ratio of nanotubes: m-m ($\sim 1/9$ of contacts) (i), m-s ($\sim 4/9$ of contacts) (ii), and s-s ($\sim 4/9$ of contacts) (iii) (highlighted in **Figure 2**). While m-m and s-s contacts provide sufficiently good tunneling from one nanotube to another one due to comparable Fermi energy levels and work functions [25], the contribution of m-s contacts (in broad chirality distribution, almost half of the contacts) is the most crucial since, in addition to tunneling between nanotubes, it is governed by Schottky barriers [26]. Therefore, for optimization of SWCNT network conductivity, either assembling purely metallic or semiconductive networks or doping is required [27,28]. The latter can significantly decrease the Schottky barrier and saturate SWCNT with charge carriers, this

way, by these two processes, leading to remarkable improvement in SWCNT network conductivity [29]. An increase in nanotube/bundle diameter was shown to positively affect junction resistance [30]. Nevertheless, overall contact resistance (experimental observations demonstrate more than one order of magnitude domination of junction resistance over intra-tube one [30]) is the most considerable factor in nanotube network conductivity.

Since the SWCNT network is mainly determined by contact resistance (as well as semiconducting/metallic ratio, which, however, requires additional efforts to be tuned), nanotube length becomes a considerable factor affecting SWCNT network conductivity. Indeed, with an increase in average SWCNT length, the number of charge carrier pathways with a minimum fraction of junctions grows. Hecht *et al.* demonstrated an empirical power law describing the nanotube length effect on the network conductivity:

$$\sigma_s \sim L^{1.46}, \quad (9)$$

where σ_s is a sheet (in this case, network) conductivity and L is a mean SWCNT length [31]. In their work, the authors considered the bundling degree effect. Minimizing their surface energy, nanotubes form strong bundles this way statistically lowering the number of pathways for charge carriers. Thus, despite a nanotube or bundle diameter increase positively affects contact resistance, excessive bundling is to be avoided to provide uniformly distributed SWCNTs as wires in the network and, in turn, higher nanotube conductivity.

Thus, SWCNT network conductivity is highly dependent on nanotube structural features. Semiconducting/metallic ratio, distributions of nanotube length and diameter,

defectiveness, and bundling degree are the main factors. Generally, increases in nanotube length, diameter, quality, and spatial distribution uniformity are key directions for the optimization of SWCNT network conductivity [32]. Next, SWCNT thin films as a 2D extension of the SWCNT network are considered, where film conductivity/transparency interplay is significant.

2.2. 2D SWCNT networks – thin films

2.2.1. SWCNT-based transparent conductive films

Macroscale implementation of a 2D network of SWCNTs is a thin film. Definitely, it is a certain simplification since SWCNT-based thin films vary in thickness from 10 nm to 1 - 2 μm [33]. Nevertheless, usually, the in-plane sheet conductivity of such films is of interest which is measured in Ω/\square . Moreover, SWCNT-based films with low thicknesses (in the range of 5 – 100 nm) appear to be transparent in the visible light range (usually 550 nm wavelength used for characterization of thin film transparency as it is in the middle of the visible light range). Recently, Ermolaev *et al.* have found SWCNT film thickness in linear proportionality with film absorbance at 550 nm (A_{550}) [34]:

$$\text{thickness [nm]} \approx 239 \cdot A_{550}. \quad (10)$$

Thus, SWCNT thin films with tens to hundreds of nm thickness possess both conductivity and transparency which opens up a route for applying them in the high-demanding electronic field of transparent conductive films (TCFs).

TCFs are a prominent part of modern electronics utilized in such areas as touchscreens, liquid-crystal displays, OLEDs, touchscreens, solar cells, and some others.

Nowadays, matured industrial technology for TCF production is based on the employment of transparent conductive oxides, primarily, indium tin oxide (ITO). Despite its high performance (about $10 \Omega/\square$ at 90% transparency), the use of quite expensive and depleting indium as well as the brittleness of ITO (which limits the development of flexible transparent electronics) pushes researchers to develop alternative materials. Among the prospective ones, TCFs based on metals, such as sputtered metallic microgrids [35] or silver nanowire networks [36]. Nonetheless, the problem of bending and aging resistance still exists, as well as the high price of noble metals. Another group of materials investigated for ITO substitution is conductive conjugated polymers, such as PEDOT:PSS (poly(3,4-ethylenedioxythiophene) polystyrene sulfonate), polypyrrole, and others [37–39]. Yet, in spite of high flexibility and simple processing, the disadvantages of conjugated polymers are related to their relatively low tolerance toward humidity and high temperatures, and generally degradable conductivity [40,41]. Graphene-based TCFs have also attracted the interest of researchers, however, limited charge transfer through graphene grain boundaries limits its development [42,43]. Among all the abovementioned materials, CNT-based thin films stand out for their flexibility, close-to-industrial optoelectronic performance level, and high prospects for scalable production [23,44]. Yet, certain drawbacks and challenges in their development take place as well, which will be discussed below.

The performance of a TCF can be characterized by several figures of merits, however, equivalent sheet resistance R_{90} (Ω/\square) – film sheet resistance R_S at 90%

transmittance at 550 nm – have turned out to be the most widely used as it is quite simple for determination and illustrative [44]:

$$R_{90} = R_s \frac{A_{550}}{A_{550}(90\%)} = R_s \frac{A_{550}}{\log \frac{10}{9}}, \quad (11)$$

where $A_{550}(90\%) = \log \frac{10}{9}$ is the absorbance at 90% transmittance at 550 nm.

Sheet conductivity linearly grows with film thickness, yet, at the same time, according to equation (10), its absorbance increases too (*i.e.*, transparency declines), which leads to a tradeoff between conductivity and transmittance:

$$T = e^{-\frac{\alpha \rho}{R_s}} = 10^{-\frac{R_{90} \cdot \log \frac{10}{9}}{R_s}}, \quad (12)$$

where T , α , and ρ are film transmittance, absorption coefficient, and resistivity, respectively; the second equation is derived from equation (11).

R_{90} of SWCNT pristine films strongly depends on SWCNT structural properties (as discussed above on SWCNT network conductivity): it may range within the hundreds of Ω/\square to hundreds of $\text{k}\Omega/\square$ [32]. Nevertheless, even the lowest values are quite far from industrial requirements, therefore, often additional procedures are applied for the enhancement of film optoelectronic properties: tuning semiconducting/metallic ratio, doping, rational design, and some others [44]. Post-treatment doping of SWCNT films with such p-dopants as HNO_3 [45], AuCl_3 [29], HAuCl_4 [46–48], or electrochemical doping by ionic liquids [49] was shown to be quite effective in eliminating Schottky barrier and increasing charge carrier density, this way dropping R_{90} by up to one order of magnitude leading to values of $50 \Omega/\square$ and below [46–50].

Rational design, or, patterning, of continuous SWCNT films is another promising approach to R_{90} improvement [44]. Fukaya *et al.* proposed a technique for the one-stage fabrication of patterned mesh-shaped SWCNT film with optimized R_{90} [51], while Mitin *et al.* demonstrated the efficiency of the post-treatment lithography-based process for creating the rational design of continuous SWCNT film [52]. Overcoming the abovementioned tradeoff between film conductivity and transparency is due to the simultaneous presence of non- or low-transparent but, at the same time, highly conductive pathways and empty spaces which results in a decrease in total transparency at maintained conductivity.

Thus, SWCNT films possess quite high prospects for successful implementation as TCFs. Post-treatment procedures, such as doping and patterning may essentially enhance their performance. Nevertheless, SWCNT-based films are rather at the stage of laboratory-scale development and not so widespread in industry. This is because of quite moderate optoelectronic properties of pristine SWCNT films caused by poor control of nanotube structural parameters during the SWCNT synthesis process. Insufficient understanding of mechanisms behind nanotube growth limits SWCNT film development.

2.2.2. CNT synthesis. Aerosol chemical vapor deposition method for SWCNT film synthesis

Carbon nanotube synthesis methods can be generally classified into two big groups: physical and chemical ones. Physical methods were actively utilized in early pioneer works. Their principle is based on applying high energy to graphite for its sublimation, which may be implemented via arc discharge or laser ablation. Meanwhile, the addition of

catalysts was demonstrated to considerably improve the process. Nevertheless, these methods are pretty energy-consuming and obtained nanotube samples were often contaminated by carbon byproducts such as soot. This pushed researchers to switch their efforts to developing chemical methods.

Chemical methods imply the chemical vapor deposition (CVD) process where a catalyst (typically, transition metals, such as iron (Fe), nickel (Ni), or cobalt (Co)) is used for the transformation of carbon precursors (such as hydrocarbons, carbon monoxide, alcohols, and many other carbon-containing compounds) into carbon [53]. In contrast to physical methods, the CVD process occurs at relatively low temperatures. Meanwhile, in addition to reaction acceleration by lowering the energy barrier for carbon source dissociation, a catalyst is responsible for nanotube nucleation, *e.g.*, it determines the shape of nuclei and, hence, nanotube diameter and chirality, and provides subsequent nanotube growth. Now it is well-established that the CVD process is initiated with the formation of a graphitic cap on the catalyst surface (catalyst-assisted nanotube nucleation) and then continues by bulk and surface diffusion of carbon intermediates through catalytic nanoparticle (NP) toward a growing nanotube. Such a sequence of stages in nanotube growth is known as the yarmulke mechanism.

In turn, CVD synthesis of CNTs may be divided into substrate-supported (or, fixed-bed) and floating catalyst CVD (FCCVD) processes. Substrate-supported CVD implies the use of catalyst seeds on a substrate (often Al_2O_3 or SiO_2) exposed to gaseous carbon precursor at high temperatures. The resulting SWCNT samples have either a vertical alignment (densely packed arrays also known as nanotube forests) or a horizontal one (long

nanotubes laying on a substrate). Also, so-called kite growth is possible too when the catalyst soars off the substrate together with nanotubes, this way avoiding problems with carbon feedstock diffusion through forests which may result in ultralong (half-meter) nanotubes [54].

FCCVD method involves operation exclusively in the gas phase. A catalyst or catalyst precursor is delivered to the reactor hot zone together with the carbon source and other reactants. Catalyst activation and nanotube growth occur while the catalyst passes through the hot zone. Produced nanotubes can be collected from the reactor walls [55], withdrawn and directly spun in fiber form from the reactor [56], or gathered by aerosol filtration [57]. The second two processes are of high interest since they provide an opportunity for continuous operation with great prospects of scaling. FCCVD allows one-stage and liquid-free production of carbon nanotubes in various forms, including fibers, aerogels, aerosols, thin films, and even polymer composites [58–62].

As a particular case of FCCVD, the aerosol CVD process operates at extreme dilution of catalyst. The aerosol CVD process is one of the most promising techniques for SWCNT thin film production as because of significant catalyst dilution it suppresses undesirable inter-nanotube collisions leading to bundling degree increase. Moreover, the most crucial advantage is the SWCNT collection method: thin SWCNT films form immediately on the filter surface when aerosol flow passes through. Next, thanks to the high nanotube hydrophobicity and hydrophilic nature of the filter, SWCNT film can be easily transferred onto a substrate of practically any material, including glass, plastics, metals, and many others [61]. Moreover, transferred onto a frame, SWCNT film is turned

into a free-standing membrane that can be used as an effective filter for nanoaerosols, a transparent electrode, a saturable absorber for ultrafast lasers, an electrochemical sensor, and in some other devices [62].

Various designs of aerosol CVD processes for SWCNT synthesis have been proposed over the last almost two decades. Typically, it is a vertical quartz tube surrounded by a furnace. Hot zone temperature varies in the range of 700 – 1200 °C. Catalyst introduction into the reactor may be implemented by delivery of vapors of metalorganic precursors, such as ferrocene or iron pentacarbonyl for iron catalyst [63], with the subsequent decomposition of the precursor, formation of supersaturated vapor of metal and homogeneous nucleation of metallic NPs (*in situ* catalyst nucleation) or by direct supply of already formed metallic NPs by hot wire [57,64] or spark discharge generators [65,66] (*ex-situ* catalyst nucleation). In the vast majority of works, the first approach with ferrocene utilized as an iron catalyst precursor is used. Meanwhile, there are two general approaches to the delivery of ferrocene and carbon sources into the reactor. Highly volatile ferrocene (saturated vapor pressure ~ 1 Pa at room temperature) may be vaporized by passing a carrier gas (N₂, H₂, or gaseous carbon source) through the cartridge with ferrocene powder, which suits for gaseous carbon sources, such as carbon monoxide, methane, ethylene, *etc.*, and was numerically used for nanotube synthesis and appeared to be quite productive (i) [67–71]. Alternatively, ferrocene may be dissolved in a carbon source and the solution is delivered by a syringe pump into the reactor, which is appropriate for liquid carbon precursors (such as toluene, ethanol, xylene, *etc.*) [72–74] (ii).

Carbon monoxide (CO) is one of the most frequently used carbon sources in aerosol CVD synthesis of SWCNTs. Carbon release is realized by the carbon disproportionation mechanism (the Boudouard reaction). Being an extremely stable molecule (bond energy is one of the highest – more than 11 eV [75]) CO does not dissociate without catalyst assistance, which results in the absence of contaminating carbon byproducts (originated from pyrolysis, which takes place for less stable hydrocarbons) and high purity of SWCNT film. The CO-based process is highly tunable which is achieved by reactor design adjustment [69,76] and the addition of growth promoters (primarily, weak oxidizers, such as CO₂ and H₂O [64,77]) and lead to quite controlled structural properties of SWCNTs [67,68,78]. The latter implies controlled conductivity of SWCNT films – this is why one of the lowest R_{90} values are achieved for the CO-based process [46,47,50]. Nevertheless, the high stability of CO has its evident drawbacks: synthesis productivity is quite low, which deteriorates yield/ R_{90} ratio – a key parameter for industrial extension [74]. This pushes researchers to switch attention to other carbon feedstocks. Yet, there are still many gaps in CO-based synthesis optimization. For instance, reducing growth promoters, such as hydrogen, was shown to improve the CO-based nanotube synthesis, yet, its influence was not investigated in detail [70,79].

A more general problem in the aerosol CVD process is attributed to the fundamental mobility of catalyst particles, which does not allow to unambiguously distinguish stages in nanotube synthesis: catalyst activation (including catalyst particles' formation and nanotube nucleation) (i), steady nanotube growth (ii), and its termination usually caused by catalyst deactivation (iii). Therefore, there is no established general kinetic model for

the SWCNT growth, which hinders the targeted optimization of the synthesis process, including, transparent conductive film production.

In particular, this fundamental limitation is one of the crucial reasons for the limitations of aerosol CVD reactor scaling. Indeed, for this purpose, the nanotube growth termination stage should be precisely detected (that is, the catalyst lifetime should be accurately estimated). Typically, it requires the collection of SWCNT samples at different residence times and routine measurement of nanotube length (which usually assumes time-consuming gathering of statistics by measuring the length of individual nanotubes (or bundles) visualized by SEM or AFM [32,67]). Meanwhile, residence time variation often is possible only by scaling the reactor itself.

Thus, the separation of nanotube synthesis stages in aerosol CVD and evaluation of growth kinetics (which includes growth rate and catalyst lifetime), the key indicators of aerosol (and, essentially, floating catalyst) CVD process, are the main challenges for the advancement of aerosol CVD synthesis of SWCNT films. Meanwhile, the development of the CO-based aerosol CVD process, being one of the most promising methods, is impeded by its relatively low productivity, which also requires new approaches and solutions.

2.3. 3D networks: SWCNT/polymer nanocomposites.

2.3.1. SWCNT/polymer nanocomposites: percolation threshold, conductivity, and prospects for electronic applications

In addition to the quasi-2D form, SWCNT networks as a macroscale ensemble can be organized in 3D form. Truly 3D nanotube networks are aerogels, or, sponges, which can be used as scaffolds for catalysis, electrodes in supercapacitors, chemical and mechanical

sensors, absorbents for filtration, and in many other applications [80–83]. Nevertheless, a network-like organization of CNTs within an external matrix, primarily, polymer, has appeared to be of much higher scientific interest. Nowadays, CNT/polymer nanocomposites are considered one of the largest fractions in the carbon nanotube market [84]. The root cause of the development of this field is the idea to use such stiff material with high surface area and aspect ratio as carbon nanotubes for polymer reinforcement to improve the mechanical properties of the final material [85,86]. The idea is quite intuitive and early pioneer studies of such nanocomposites already date back to 1994 when Ajayan *et al.* fabricated MWCNT/epoxide-based resin [87]. Nevertheless, the purposes of CNT/polymer nanocomposite fabrication are not confined only to reinforcing polymers. The addition of conductive nanotubes into insulating polymer reveals fundamentally new features of the material, such as antistatic and conductive properties, as well as sensitivity to external stimuli.

The conductivity of SWCNT/polymers is a topic that has been investigated quite thoroughly over the last two decades [16,18,88]. Although the conductivity principles are the same as in pure CNT networks discussed above, nanotube/polymer interfaces play a considerable role in network formation and organization. As essentially, CNT/polymer nanocomposites are produced by mixing nanotubes in polymer solution/melt/precursor (discussed below), the formation of a uniform network is complicated by strong inter-nanotube attraction. Moreover, below a certain concentration, nanotubes cannot construct a network within the whole bulk of the polymer – that is, conductive pathways may be not

formed yet and the resulting conductivity of nanocomposite is comparable with neat polymer.

The features of CNT/polymer conductivity at such low nanotube concentrations are typically described by the percolation theory. The critical concentration required for the formation of a developed conductive network of nanotubes within the whole matrix is a percolation threshold [88]. Thus, the conductive nature of nanocomposite is strongly dependent on CNT concentration. Statistical percolation theory predicts a scaling law describing the conductivity (σ) dependency on the concentration of a filler φ :

$$\sigma \sim (\varphi - \varphi_c)^t, \quad (13)$$

where φ_c is a percolation threshold and t is a fitting parameter, which is ~ 2 for 3D and $\sim 4/3$ for 2D networks with an approximation of the ideal random distribution of straight fillers [16,88]. A typical representation of a percolation curve is represented in **Figure 3a**, while **Figure 3b** depicts a real experimental dependency of CNT/polymer conductivity on CNT concentration. Usually, dependency (13) is plotted in log-log scales where φ_c is varied incrementally until the best fitting is found (inset in **Figure 3b**). According to the percolation theory, based on the exclusive volume concept, at the uniform isotropic distribution of a rod-shaped filler, the percolation threshold is only determined by the filler aspect ratio η [89,90]:

$$\varphi_c \approx \frac{0.7d}{L} = \frac{0.7}{\eta}, \quad (14)$$

where L and d are a filler (nanotube) length and diameter, respectively. Nonetheless, experimental results may significantly deviate both to lower or higher values compared to

theoretically predicted ϕ_c . For instance, ultralow values of ~ 0.002 wt% of CNT loading were observed for MWCNT/epoxy nanocomposites at the CNT aspect ratio not exceeding 1000 [91,92]. This was explained by the reorganization of the nanotube network, so that conductive pathways are formed at lower concentrations than at homogeneous dispersion and, in some works, was attributed to the so-called kinetic (non-statistical) percolation threshold [93]. Higher values usually imply poor dispersibility of nanotubes in polymer, that is, high agglomeration degree, which is essentially the major issue in CNT/polymer fabrication processes.

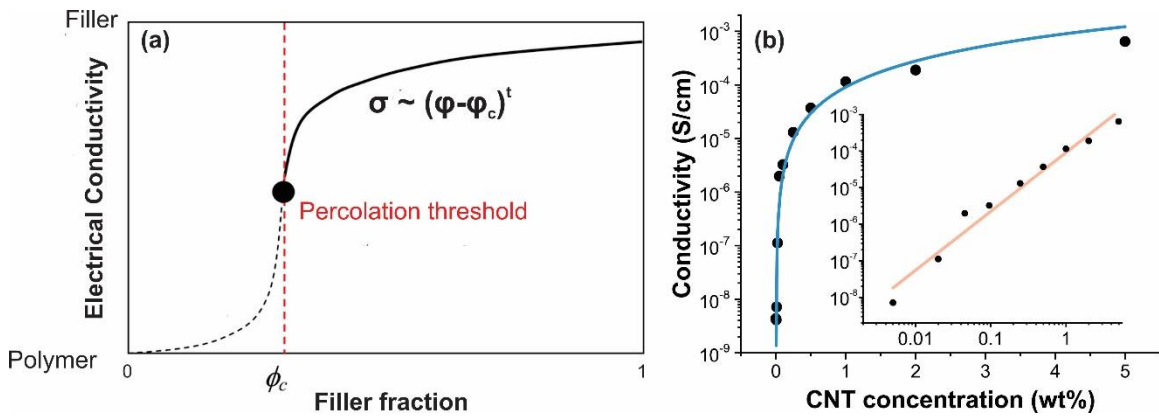


Figure 3. (a) Theoretical representation of percolation behavior of composite conductivity (with highlighted levels of neat polymer and filler conductivity) (modified from [16]). (b) Typical experimental percolation curve describing CNT/polymer nanocomposite conductivity dependency on CNT concentration; inset: the same dependency plotted in log-log scale.

The inclusion of conductive fillers as carbon nanotubes in insulating polymer opens up completely new application fields of polymer-based materials, starting from pretty simple as antistatic tires and finishing with high-tech ones, such as electromagnetic interference (EMI) shielding as well as chemical and mechanical sensors [94]. Especially, elastomer-based nanocomposites with CNTs are of high interest as such flexible and

stretchable conductive materials are excellent candidates for intensively developing soft electronics [95,96]. Thus, stretchable EMI shielding materials required for protection from information leakage and generally abnormal operation are highly demanding [97–99]. In particular, with the development of THz optics employed in imaging, wireless communication, diagnostics, and many other fields [100–102], EMI-shielding in the THz range, provided by lightweight and lower fabrication cost CNT/polymer nanocomposites, attracts high attention too [103–105].

A more unique feature of CNT/polymer conductivity is its sensitivity to external stimuli, which could be chemical environment, temperature, or mechanical exposure (pressure, strain, *etc.*). Such resistive response is induced by the reorganization of the nanotube network in polymer caused by chemical or mechanical perturbations. Major routes to CNT percolation network reorganization comprise general deformation of the CNT network and breakage of nanotubes (i), disruption of existing contact junctions or the emergence of new ones (ii), and average change of inter-nanotube distance (iii) [16,106]. The latter factor is a crucial one for slight stimuli since it implies changes in tunneling resistance in a network: exponential dependency on distance (equation (6)) results in enormous varying of nanocomposite resistivity. In particular, this is the case for chemical sensors where polymer swelling or, vice versa, drying/destruction under an external chemical environment leads to changes in gaps between nanotubes, this way, providing chemiresistive properties of CNT/polymer nanocomposites [107]. Mechanical impact may be significantly stronger enabling all the abovementioned contributions. It is worth noting that tunneling resistance contribution and formation/disruption of contact inter-tube

junctions are especially tangible at near-to-percolation threshold concentrations. Besides, lower agglomeration and entanglement degrees (higher dispersion degree) positively affect sensitivity because of higher overall changes in inter-nanotube distance [16,18]. Thus, low-concentrated CNT/polymer nanocomposites perform as resistive sensors better.

Mechanical sensors can be roughly divided into pressure and strain sensors. Resistance of former ones usually drops as many new conductive pathways form, while for strain sensors it increases rapidly for the opposite reason. Meanwhile, durability and stability over multiple loading cycles is important factor in real devices. The high efficiency of CNT/polymer nanocomposites as mechanical sensors (both pressure [108] and strain [109–112] ones) and their applicability in various sensor-based devices, such as human motion detectors [113,114] and health monitors [115,116], were repeatedly demonstrated and their outperformance over conventional metal- or semiconductor-based piezoresistive devices [16]. Mechanical sensing performance is characterized by gauge factor (GF) describing resistance change regarding deformation extent:

$$GF = \frac{\Delta R/R_0}{\Delta l/l_0} = \frac{\Delta R/R_0}{\varepsilon}, \quad (15)$$

where l_0 and R_0 are initial sensor length/width and resistance, respectively, Δl and $\Delta R/R_0$ are corresponding changes, and ε is strain.

Thus, 3D networks of carbon nanotubes formed within a polymer matrix introduce conductivity in initially insulating polymer making CNT/polymer nanocomposites highly attractive for soft electronic applications. Meanwhile, a homogeneous spatial distribution of nanotubes and a high aspect ratio are needed to provide high conductivity and low percolation threshold, the minimum nanotube concentration required for nanocomposite to

become conductive. Nevertheless, these two conditions often contradict each other in the fabrication of nanocomposites, which will be discussed below.

2.3.2. Fabrication of CNT/polymer nanocomposites. CNT dispersion degree.

CNT/polymer nanocomposite fabrication methods usually imply the mixing of nanotubes with polymer or its monomer with subsequent post-processing procedures. Three main groups in fabrication techniques can be highlighted: solution mixing (nanotubes are mixed in polymer solution) (i), melt blending (nanotubes are mixed in melted polymer) (ii), and *in situ* polymerization (polymerization occurs in the presence of admixed nanotubes) (iii) [117]. Meanwhile, the methods are varied according to the mixing techniques used: homogenization, ultrasonic treatment, shear mixing, extrusion, three-roll milling, and some others [94]. The selection of methods depends mostly on polymer type (foremost, thermoplastic or thermosetting) and the nanocomposite specification.

Solution mixing is one of the simplest and the most widespread techniques involving CNT dispersion in polymer solution by vigorous mechanical stirring (homogenization) and/or bath/probe ultrasonication coupled with a controlled solvent evaporation process, during which, however, the reverse process of nanotube re-agglomeration may take place [117,118]. Nanotube processing in polymer melt is suitable for insoluble thermoplastics and is usually accompanied by more powerful dispersion techniques, such as extrusion or high shear mixing, because of the high viscosity of polymer melt, which, however, may be damaging for nanotubes and result in nanotube breakage and defect introduction [94]. *In situ* polymerization usually yields a higher state of CNT dispersion, yet, its applicability is limited to thermally unstable and insoluble

polymers as well as polymerization may lead to accidental CNT functionalization or grafting polymers on the nanotube walls, while, at the same time, CNTs can significantly affect the polymerization process and resulting polymer structure [117,119]. Among others, three-roll milling is considered one of the most effective techniques for nanotube de-agglomeration and de-bundling resulting in their high dispersibility [120]. Nevertheless, it is quite expensive and resource-intensive as well as not may be not appropriate for certain polymers.

Alternatively, the solution mixing technique may be adapted in such a way as to avoid a long-time solvent elimination stage. Proposed by Du *et al.* [121], coagulation precipitation (CP), which is also known as nonsolvent induced phase separation (NIPS) engages the addition of anti- (or, poor) solvent into polymer solution causing instant precipitation of polymer chains wrapping carbon nanotubes, this way immediately forming CNT/polymer nanocomposite. At highly homogeneous CNT dispersion prepared preliminarily, a high rate of nanocomposite formation may result in improved spatial distribution of nanotubes in polymer resulting in better nanocomposite properties [122].

CNT/elastomer nanocomposite production typically employs solution mixing and melt blending techniques as commercial elastomers are often of interest because of their predictable good mechanical properties [123]. Among other elastomers, due to its high affinity to carbon nanomaterials, elasticity, and broad availability, thermoplastic polyurethane (TPU) is a promising polymer matrix for the fabrication of elastic functional CNT-based nanocomposites [124,125]. CP was rarely used for CNT/TPU nanocomposites,

yet, CNT uniform distribution originated from this technique was shown as well as high prospects for strain sensing, EMI shielding, and erosion resistance [99,122,126].

The vast majority of publications devoted to CNT/polymer nanocomposites refer to MWCNTs. The prevalence of MWCNT/polymer nanocomposites over SWCNT-based ones is explained by higher availability (lower production costs) and dispersibility. Nonetheless, fundamental advantages of SWCNTs, such as higher aspect ratio, lighter weight, and absence of interlayer slippage typical for MWCNTs [127], as well as the recent rapid growth of their production shifts MWCNT/SWCNT nanocomposites balance [84,128]. Many works report superior properties of SWCNT/polymer nanocomposites, including mechanical properties, electrical conductivity, and percolation threshold [106,129–131]. Recently, Shin *et al.*, have reported a thorough study comparing CP-prepared elastic CNT/TPU nanocomposite properties for different kinds of starting carbon nanotubes, including short MWCNTs, long MWCNTs, and long SWCNTs [99]. They have demonstrated the outperformance of nanocomposites based on long MWCNTs and SWCNTs in conductivity and related to it EMI-shielding efficiency, while, however, short MWCNTs worked better for strain sensing. It is worth noting that SWCNT used had an extremely high aspect ratio of orders of 10^5 - 10^6 , which evidently complicates nanotube dispersibility and likely led to relatively high percolation thresholds. This refers to a confrontation between dispersibility and high aspect ratio, which both are desirable for higher conductivity and associated electronic applications. Thus, new fabrication approaches that would be suitable for effective but non-destructive dispersion of moderate-

length SWCNTs and provide a desirable golden middle between CNT aspect ratio and spatial distribution are still highly demanding.

Another general issue in the fabrication of nanocomposites based on both multiwalled- and single-walled CNTs is the utilization of nanotube powders as a raw starting material, which ultralow bulk density and high aerosolization ability with potential health hazards significantly hamper scaling the production. These complications are the main drivers for high attention paid to nanotube masterbatches: highly concentrated (10 – 20 wt%) paste with embedded and pre-dispersed CNTs used as a precursor for subsequent nanocomposite material production by simple dilution in polymer melt/solution, which is considerably more appropriate for the production line [132]. Yet, in contrast to pristine SWCNT powders, masterbatches are polymer-specific and require extra storage conditions, which is reflected in their higher price. Thus, alternative universal solutions avoiding both specificity to polymer and aerosolization risks are of high research interest.

2.4. Summary: general routes on optimization of SWCNT networks for electronic applications

Thus, possessing a unique set of fundamentally unique properties, including electrical conductivity and optical features, SWCNTs are highly promising material for electronic and optical applications. Meanwhile, the majority of applications employ macromaterials based on random SWCNT networks. Among the most prominent ones, SWCNT-based TCFs and SWCNT/polymer nanocomposites

Nevertheless, an essential obstacle in the development of such materials is the controlled synthesis of SWCNTs and the assembling of their networks with tunable

properties. Foremost, nanotube length and uniform spatial distribution are highly desirable. Besides, the increase in fabrication process productivity and adjustment of high-level organization of SWCNT networks are of high scientific and practical interest. This thesis is aimed to propose certain solutions for this ambitious and broad but highly exciting task.

Chapter 3. Methods

3.1. Material synthesis and fabrication

3.1.1. CO-based aerosol CVD synthesis of SWCNTs

As discussed above, the aerosol CVD process is one of the most advantageous methods for the synthesis of thin SWCNT films. In this work, CO-based aerosol CVD synthesis of SWCNTs was employed. Among the other carbon feedstocks frequently used, CO provides the highest purity, low nanotube defectiveness, and one of the lowest equivalent sheet resistances (R_{90}). Carbon release occurs exclusively on the catalyst surface according to the Boudouard reaction (CO disproportionation):



In addition to the carbon source (CO), growth promoters, such as carbon dioxide (CO₂) and hydrogen (H₂) were added in some experiment sets. While CO₂ acts as a weak oxidizer and enhances nanotube growth by etching amorphous carbon poisoning catalyst surface according to reverse reaction (16), H₂ utilization may lead to an additional carbon-feeding reaction to the system with water (H₂O) formation:



as well as to carbon hydrogenation (methane (CH₄) formation):



The aerosol CVD reactor used in this work consists of a vertical quartz tube (72 mm diameter) surrounded by a three-zone furnace with an isothermal hot zone of ~ 60 cm and a gas supply system including gas cylinders, gas lines, and mass flow controllers

(MFC, Bronkhorst) (illustrated in **Figure 4**). Ferrocene (Sigma Aldrich, 98%) was used as an iron catalyst precursor and was supplied to the reactor by passing a carrier gas (CO, 99.99%) through the cartridge (“cartridge flow”, Q_{cart}) with ferrocene powder (with admixed SiO₂ granules facilitating flow pass) kept at the fixed temperature of 28 °C, so that ferrocene vapor pressure (p_{ferr}) was maintained at 1.34 Pa. To provide optimal (in terms of SWCNT properties/productivity) catalyst delivery rate, the reactor was supplemented with a thin injector (which tip ends at the beginning of the furnace), and the rate of the flow with ferrocene vapor was fixed at 2 lpm by adding “dilution flow” of CO (Q_{dil}) [69].

The rest of the CO flow (“main flow”, Q_{main}) was introduced via the main inlet into the reactor and its rate was adjusted to set a total flow rate (Q_{tot}) according to the residence time set. The total flow rate is inversely proportional to the residence time and a reactor temperature profile is taken into account (**Figure 4**; details are in SI of **Publication I**). The total flow rate of the 2.1 – 10 lpm range appeared to correspond 17.9 – 3.8 s residence time window.

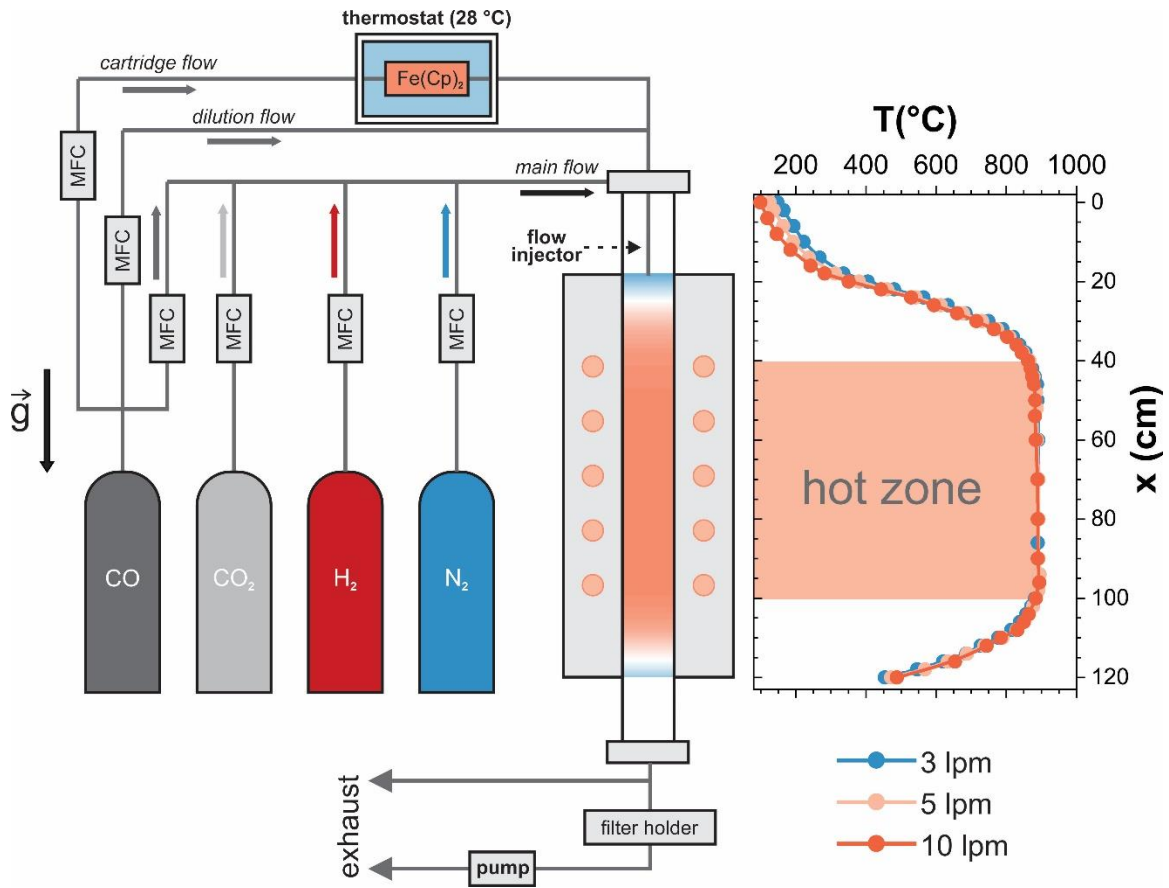


Figure 4. Schematic representation of aerosol CVD reactor. On the right, the reactor temperature profile at the set temperature of 880 °C at different total flow rates with highlighted hot isothermal zone are shown. Modified from **Publication I**.

Besides, in some experiments, growth promoters (CO₂ (99.995%) and H₂ (99.9999%)) and nitrogen (N₂) were added by admixing their flows to the “main flow”. The concentrations of additives were controlled by fixing flow rates of the corresponding gases by MFCs (Q_{add}) and calculated as follows:

$$c_{add} [\text{vol}\%] = \frac{Q_{add}}{Q_{tot}}. \quad (19)$$

Meanwhile, catalyst concentration was set by “cartridge flow” and estimated according to the p_{ferr} and taking into account that the reactor is operated at atmospheric pressure p_{atm} :

$$c_{cat} [\text{ppm}] = \frac{p_{ferr}}{p_{atm}} \cdot \frac{Q_{cart}}{Q_{tot}} \cdot 10^6, \quad (20)$$

and kept at 0.9 ppm unless otherwise stated. It is worth noting that the reactor system is located in the thermostated laboratory room and temperature deviations do not exceed 1-2 °C. Thus, temperature-caused inaccuracies of flow rate are below ~ 0.7%, which is comparable to the technical limitations of MFCs. Meanwhile, ferrocene vapor pressure is highly sensitive to temperature deviations (for instance, p_{ferr} is 1.00 Pa at 25 °C and 1.34 Pa at 28 °C, which is equal lead to ~ 30% difference in the catalyst concentration in the system). This is why the ferrocene cartridge is kept at the thermostat at a constant temperature of 28 °C.

The reactor hot zone temperature was mainly set at 880 °C (the most studied at optimal synthesis temperature for the CO-based CVD process [32,61,78]), yet, in some experiments it was reduced to 854 °C or elevated to 1000 °C.

SWCNT films were collected by filtering passing aerosol flow (mixed cellulose ester filters, HAWP, Merck), and the flow rate through the filter Q_{filter} was controlled and did not exceed Q_{tot} . After the synthesis, the SWCNT film was transferred onto a glass substrate for further measurements. To improve the optoelectronic properties of the films, for some samples, doping was applied. SWCNT films were doped by HAuCl_4 [46] using a dip-coating method [47]: SWCNT films on a glass substrate were dipped (Apex Instr. Co. Xdip-MV1) at the controlled speed of 300 mm/min for 2 min.

In some experiments, a differential mobility analyzer (DMA) coupled with a condensation particle counter (Scanning Mobility Particle Sizer Spectrometer 3938, TSI)

was used for measurements of aerosol particle concentration and size distribution. This technique allows obtaining aerosol particle number distributions (in the assumption of spherical charged particles) and distinguishing iron NPs (effective diameter < 20 nm) from nanotubes (effective diameter in 40 – 200 nm range) as well as estimating shifts in nanotube length/budling degree.

3.1.2. Fabrication of SWCNT/polymer nanocomposites

Another big object of the current research is SWCNT/polymer nanocomposites. Two different kinds of nanocomposites were investigated: elastic SWCNT/TPU nanocomposites and ones based on thermoset epoxide (SWCNT/epoxy nanocomposites). For both kinds, commercial SWCNT powders (Tuball©, OCSiAl) were used provided by the manufacturer parameters: length above 5 µm and diameter of 1.6 ± 0.4 nm [133] (aspect ratio is about 3000). The bulk density of the nanotube powder is estimated at 18 g/l.

SWCNT/TPU nanocomposites were manufactured using the coagulation precipitation (CP) technique. For this, commercially available TPU pellets (R130A70, Ravago) were vacuum-dried at 80 °C overnight and then dissolved in dimethyl sulfoxide (DMSO, chemically pure), so that TPU/DMSO solution was 45 g/l concentrated. Next, SWCNT powder was weighted according to a specific weight fraction (in the 0.005 – 1.00 wt% range), added to the TPU/DMSO system, and dispersed in this viscous solution by a homogenizer (T-25 digital Ultra-Turrax, IKA; 10 min, 8000 rpm) and by an ultrasonication tip (Branson Sonifier 450; 45 min, 200 W). The resulting SWCNT/TPU/DMSO suspension seemed uniformly black once pre-dispersion procedures were executed. Immediately after the pre-dispersion, the suspension was poured into intensively stirred water used as a TPU

antisolvent (suspension/water volume ratio was kept at around 1/15), which was followed by instant precipitation. The obtained spongy deposit was then washed in distilled water, vacuum-dried overnight (at 80 °C), and milled into small sub-millimeter scale granules in a frozen state (the sample was preliminarily frozen in liquid nitrogen). After that, the nanocomposite granules were subjected to a hot compression procedure (Collin P 300 P/M; 180 °C, 2 atm, 5 min) and molded into disk-shaped samples (0.5 mm thickness and 16 mm diameter: for conductivity measurements and morphology visualization) or 2 mm thick dumbbell-shaped ones (for tensile tests (ISO 37 standard)). **Figure 5** illustrates the whole fabrication process.

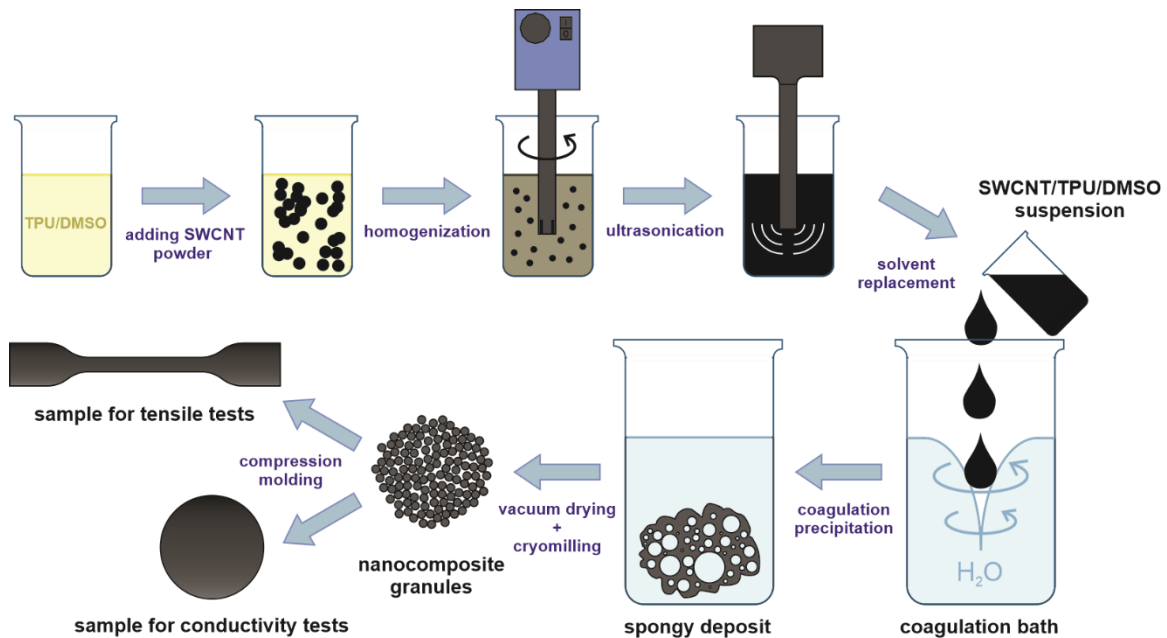


Figure 5. Schematic illustration of the fabrication of elastic SWCNT/TPU nanocomposites. Modified from **Publication II**.

Meanwhile, for thermoset SWCNT/epoxy nanocomposites, the nanotube powder bulk density effect on final nanocomposite properties was studied. In addition to pristine SWCNTs (the same as used for SWCNT/TPU nanocomposites; “pristine”), as a solution

for aerosolization-free raw nanotube material, briquette-shaped (“briquettes”) pre-consolidated form of SWCNT powder was proposed. For this, pneumatic compression was applied (Allied High-Tech Products; 6 atm, 5 min). Since compression could affect the resulting nanotube dispersion in polymer, for a reasonable comparison of bulk density (or, consolidation degree) effect on nanotube dispersion, the opposite procedure of powder expansion was performed. For this purpose, a rapid expansion of supercritical suspensions (RESS) technique was used [134,135]. This method involves exposure of SWCNT powder in supercritical fluid (nitrogen, 150 atm, 40 °C, 30 min) in the 25 ml high-pressure vessel followed by rapid injection of the suspension into the larger vessel (500 ml) kept at ambient pressure. High pressure difference results in rapid expansion accompanied by an effective decrease in the bulk density along with de-bundling. Finally, a fourth group of samples was prepared using commercially available nanotube masterbatches (“MB”) based on the same matrix (epoxy) (Tuball 301, OCSiAl) to compare SWCNT powders with different bulk densities. SWCNT powders with different bulk densities were further characterized by Raman spectroscopy (to provide information on possible structural damages caused by compression/expansion procedures expressed in I_G/I_D values (details are below)) and the Brauner-Emmett-Teller method (BET; NOVAtouch LX2, Quantachrome Instruments; to provide information on specific surface area extracted from liquid nitrogen adsorption/desorption isothermal curves). **Table 1** contains information on the structural properties of the initial SWCNT-based raw material used for further nanocomposite manufacturing.

Table 1. Parameters of SWCNT-based raw material for nanocomposite fabrication (* bulk density of SWCNTs in the masterbatch is estimated using the density of the material (0.97 g/cm³) and weight fraction of SWCNTs (10 wt%)).

Designation	Powder type	Bulk density (g/l)	Specific surface area (m ² /g)	I _G /I _D	Manufacturing
Briquettes	Consolidated	450	570	70 ± 40	SWCNTs subjected to pneumatic compression.
MB	Masterbatches	~ 97*	-	-	Commercial SWCNT masterbatch produced through three-roll milling.
Pristine	Unaltered	18	580	80 ± 20	SWCNTs, no pre-dispersion.
RESS	RESS-expanded	1.6	560	70 ± 10	SWCNTs subjected to RESS.

Nanocomposite sample fabrication was performed according to an optimized, standardized processing procedure, which includes SWCNT pre-dispersion in the solvent (acetone) in an ultrasonic bath (1 h) (alternatively, masterbatches were soaked in solvent), adding nanotube suspension (or, masterbatches) in polymer (bisphenol A/DGEBA epoxy resin; EPOLAM 2031, Axon) according to the intended weight concentration (in 0.005 – 2.00 wt% range), homogenization of nanotube suspension in polymer (7500 rpm, 45 min; and 10000 rpm, 15 min), ultrasonication (1 h), and vacuum degassing (20 min). Then, to SWCNT/epoxy suspension, a hardener in an appropriate amount was added and hand-stirred for 10 min. Next, the suspension was again degassed (5 min) and poured into silicone molds (8 × 1 × 0.4 cm³). Finally, samples were cured for 7 h at 60 °C with 12 h of oven cooling and post-cured for 5 h at 60 °C.

3.2. Conductivity tests

Conductivity σ of a sample is obtained from measurements of resistance R and derived according to an equation:

$$R = \rho \frac{l}{w \cdot h} = \frac{1}{\sigma} \cdot \frac{l}{w \cdot h}, \quad (21)$$

where $\rho = \frac{1}{\sigma}$ is sample resistivity, and l , w , h are dimensions (length, width, and thickness, respectively). If nanocomposite conductivity was calculated generally according to equation (21), for thin films, because of their high conductivity sheet geometry, another approach was used.

3.2.1. Sheet resistance of SWCNT film

For a square-shaped sample ($l = w$) with thickness h , equation (21) may be extended:

$$R = \rho \frac{l}{l \cdot h} = \frac{\rho}{h} \equiv R_s, \quad (22)$$

where R_s is a sheet resistance measured in Ω/\square . Thus, the sheet resistance is suitable for the characterization of thin films and is determined by film conductivity and thickness. To avoid dependency on thickness, equivalent sheet resistance R_{90} (sheet resistance at 90% transmittance) is used (introduced above, equation (11)). Therefore, R_{90} is determined only by film conductivity.

Sheet resistance is usually measured by a 4-probe station (Jandel RM3000), which operation principle is in using four equidistant (s) electrodes (probes), two of which act as a current source (I) and two inner ones – as a voltmeter (V) (depicted in **Figure 6**). Such

configuration allows subtracting probe-sample contact resistance. In consideration of a sample (thin film), which thickness is much smaller than inter-probe distance, which, in turn, much smaller than sample lateral dimensions ($h \ll s \ll l$), from differential Ohm's law and cylindrical geometry of current density front, R_s can be calculated from set I and measured V values:

$$R_s = \frac{V}{I} \frac{\pi}{\ln 2}. \quad (23)$$

In the current work, the sheet resistance of SWCNT films synthesized and transferred to a glass substrate was measured at least six times at different spots and angles (to avoid film non-uniformity and anisotropy contribution), and the averaged result was used for R_{90} calculations.

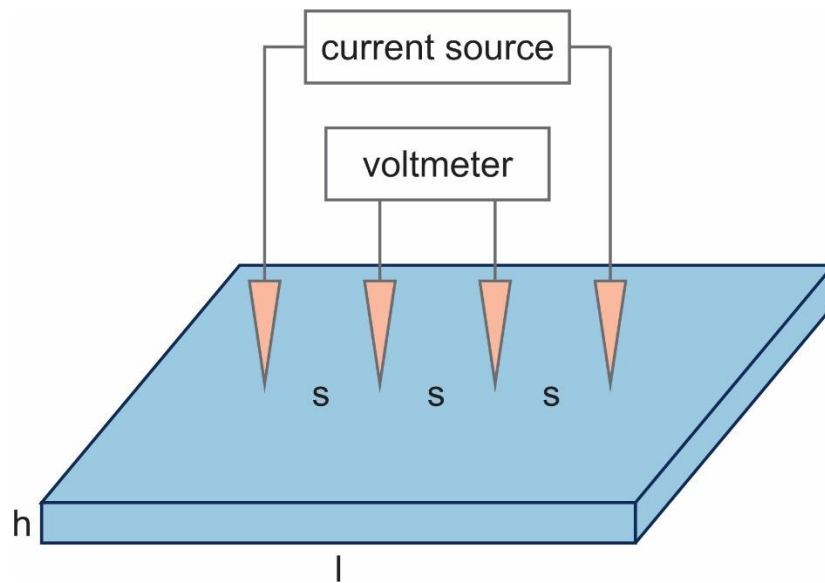


Figure 6. Operation principle of 4-probe station for sheet resistance measurements.

3.2.2. Nanocomposite conductivity. Impedance spectroscopy

The conductivity of nanocomposites was investigated by both direct current (DC) and alternative current (AC) tests. DC conductivity was calculated for SWCNT/epoxy samples (due to their general higher conductivity compared to SWCNT/TPU ones (discussed below)) by equation (21), where, for resistance measurements (Keithley 2400 source meter), conductive silver paste (Ted Pella) was applied onto the whole surface of brick-molded sample ends ($l = 8 \text{ cm}$, $w = 1 \text{ cm}$, and $h = 0.4 \text{ cm}$).

In addition to conductivity measurements, AC tests can provide useful information on SWCNT network morphology within a polymer, including percolation threshold, the contribution of tunneling resistance, and many others. AC tests were carried out with the impedance spectroscopy technique. SWCNT/epoxy nanocomposites were measured in the same two-electrode configuration, while a coin-cell setup was used for disk-shaped SWCNT/TPU samples. Impedance spectra (Bode charts) were recorded in 1 Hz – 1 MHz range at 200 mV amplitude using a VMP3 Bio-Logic potentiostat/galvanostat. For comparison to DC resistance measurements' results, the real part of the impedance Z_{real} at 1 Hz (the lowest frequency) was used. Conductivity was calculated according to the adapted version of equation (21):

$$\sigma = \frac{l}{Z_{real} \cdot A}, \quad (24)$$

where A is cross-sectional contact area: $A = w \cdot h$ for brick-molded SWCNT/epoxy nanocomposites; and $A = \frac{\pi \cdot d^2}{4}$ for disk-molded SWCNT/TPU nanocomposites ($d = 16 \text{ mm}$, and l from equation (24) is disk thickness (0.5 mm)).

3.3. Optical characterization

3.3.1. Optical absorbance spectroscopy

Optical absorbance spectroscopy in the ultraviolet (UV) – visible (vis) – near-infrared (NIR) range (UV-vis-NIR) is one of the most informative and main characteristic tools for SWCNT-based transparent thin films and suspensions. The most useful information that can be extracted from optical absorbance spectra is SWCNT chiralities and/or, at least, diameters of SWCNTs [15,136]. Besides, it can even provide additional information on nanotube bundling degree [137]. Being non-destructive, quick, universal, and quite simple for interpretation technique, optical absorbance spectroscopy is an essential part of SWCNT film investigation.

UV-vis-NIR light range ($\sim 200 - 3000$ nm) selection is due to absorbance peaks typical for nanotubes located in this range. As was mentioned above, SWCNTs have specific DOS with such features as van Hove singularities causing strong absorbance of SWCNT film/solution scanned at the wavelengths corresponding to inter-singularity transition energies resulting in pronounced peaks (S_{11} , S_{22} , M_{11} , *etc.*). These transition energies are specific for each SWCNT chirality. Besides, a collective oscillation of π -electrons excited by irradiation results in the most pronounced peak in the UV region. **Figure 7** represents typical SWCNT film optical absorbance spectra in the UV-vis-NIR range and van Hove singularities with highlighted peaks (transitions between singularities) peculiar to SWCNTs.

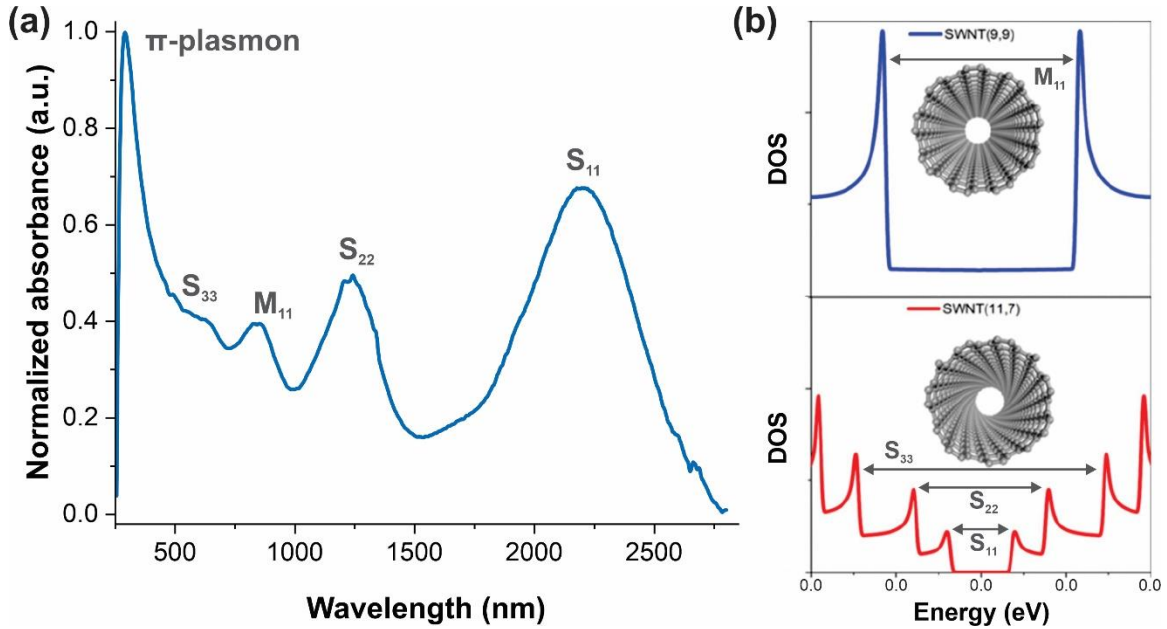


Figure 7. (a) Typical UV-vis-NIR optical absorbance spectrum of SWCNT film with highlighted peaks peculiar to SWCNTs. (b) Illustration of SWCNT DOS for m-SWCNT (top) and s-SWCNT (bottom) with highlighted transitions between van Hove singularities. Adapted with permission from [138]. Copyright (2020) by the American Chemical Society.

In addition to the characterization of SWCNT diameter distribution, absorbance at 550 nm is used for the normalization of sheet resistance for R_{90} determination (equation (11)). This arises from linear proportionality between film thickness and absorbance (equation (10)) originating from the Beer-Lambert law (often used for solution characterization):

$$T = \frac{I}{I_0} = e^{-\epsilon ch} = 10^{-A}, \quad (25)$$

where ϵ is an extinction coefficient, c is solution concentration (not applicable for thin films) and h is an optical path in the absorbing sample, *e.g.*, the film thickness. In addition to the estimation of equivalent sheet resistance, proportionality between SWCNT film thickness and absorbance (equation (10)) is used for the characterization of aerosol CVD

synthesis productivity of SWCNTs, that is, nanotube yield. Indeed, the microgram scale of SWCNT film weight (50% transparent nanotube film density was estimated as $5.5 \mu\text{g}/\text{cm}^2$ [139]) requires ultrafine weight sensitivity, meanwhile, for TCF production, film transparency is of higher interest than its weight. Moreover, at 550 nm (middle of the visible light range), the contribution of the abovementioned SWCNT peaks is significantly higher than plasmonic peaks of metal nanoparticles (always present in SWCNT samples obtained in a CVD process) [140–142], while their weight could be even comparable to SWCNTs' one. Thus, in this work, SWCNT film synthesis *yield* [cm^2L^{-1}] is defined as the 90% transparent film area collected for a time $\tau_{colleciton}$:

$$\text{Yield} [\text{cm}^2\text{L}^{-1}] = \frac{A_{550} \cdot S_{filter}}{A_{550}(90\%) \cdot \tau_{colleciton} \cdot Q_{filter}} = \frac{A_{550} \cdot S_{filter}}{\log \frac{10}{9} \cdot \tau_{colleciton} \cdot Q_{filter}}, \quad (26)$$

where S_{filter} is the filter area and the rate of the flow passed through the filter is Q_{filter} . That is, the real absorbance of the obtained film is normalized to 90% transparency.

3.3.2. Raman spectroscopy

Another important for nanotube science optical spectroscopy technique is Raman spectroscopy. Based on resonant Stokes scattering, it provides crucial information on nanotube structural features extracted from recorded phonon spectra. A typical Raman spectrum of SWCNTs is shown in **Figure 8**.

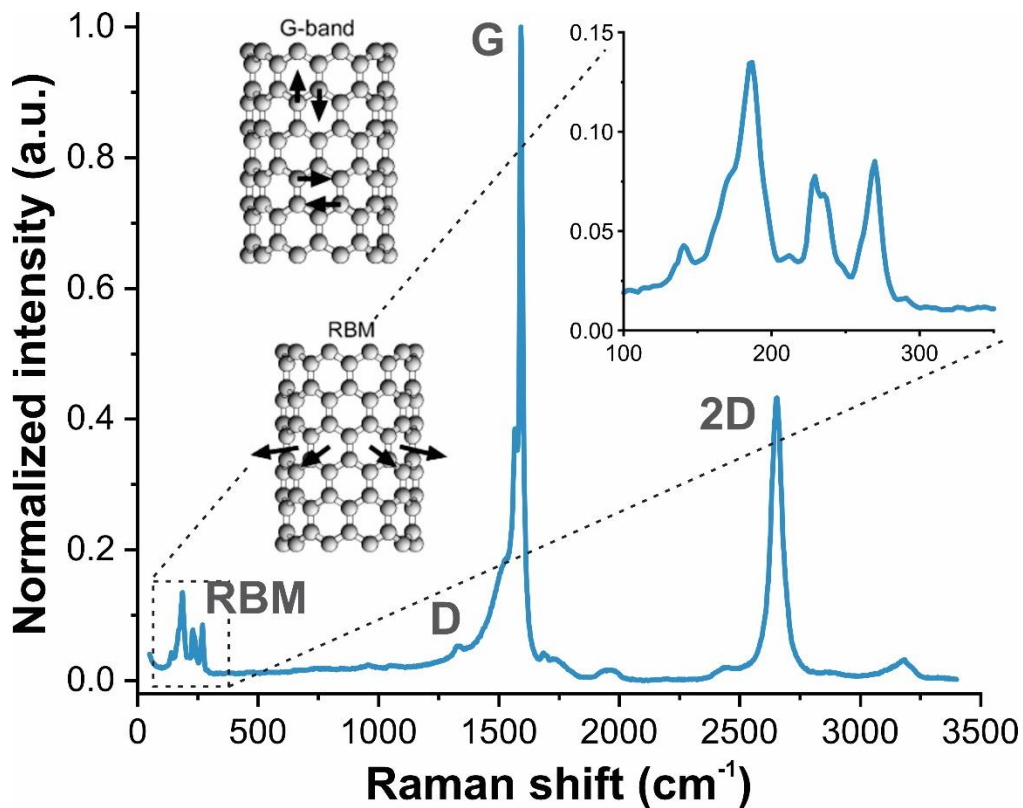


Figure 8. Typical Raman spectrum of SWCNT films with highlighted modes and enlarged RBM peaks; insets illustrate in-plane (G) and out-of-plane (RBM) vibration modes [143].

The dominant peak at $\sim 1590 \text{ cm}^{-1}$ is associated with an in-plane vibration mode, typical for all graphitic materials, and called the G band. Nevertheless, CNTs have a feature of split G peak (G^+ and G^-), which is caused by nanotube curvature and slight deviations between axial and transverse directions of in-plane vibrations. While the higher-energy Lorentzian G^+ band is independent of both nanotube diameter and chirality, the G^- band is a narrow Lorentzian peak for s-SWCNTs, a broad peak with asymmetrical Breit-Wigner-Fano (BWF) line shape for m-SWCNTs, and absent for armchair nanotubes. Second-order scattering events may occur with phonons scattered by sp^3 -hybridized carbon, which might be inconsistencies in a hexagonal lattice, generally referred to as defects (vacancies,

functional groups, and others), and amorphous carbon. This disorder-induced band (D band) appears as a small peak near 1350 cm^{-1} . SWCNT quality/purity is usually characterized as a ratio of intensities of G and D modes (hereinafter, I_G/I_D), used in this work too. The two-phonon process results in a 2D band. The last noticeable modes are attributed to out-of-plane vibrations and are peculiar only to closed graphitic structures as nanotubes – radial breathing modes (RBM, since nanotube diameter oscillations can be imagined as “breathing”). Theoretical and experimental studies show inverse proportionality between RBM frequency ω_{RBM} and nanotube diameter d [144]:

$$\omega_{RBM} [\text{cm}^{-1}] \cong \frac{228}{d [\text{nm}]} + 16. \quad (27)$$

Thus, if an ensemble of SWCNTs with a broad distribution of chiralities and diameters, such as a SWCNT film or a fiber, is measured, a series of RBM peaks are observed (as shown in **Figure 8**). It should be noted that since resonant scattering is several orders of magnitude more probable than non-resonant one, characteristic vibration modes are strongly dependent on laser excitation wavelength. Therefore, only a small fraction of nanotubes is in resonance and it is necessary to use several laser wavelengths for reasonable judgments upon nanotube diameter distribution in a sample based on RBM peaks, while optical absorbance spectroscopy employs all the wavelengths in the set range. Similarly, laser excitation wavelength affects G band shape. Since at different excitation frequencies, different nanotube ensembles appear to be in resonance (with different metallic/semiconducting ratios), which leads to different contributions of Lorentzian and BWF functions in the G band affecting its shape [145].

In this work, both SWCNT films synthesized at aerosol CVD reactor and commercial SWCNT powders were characterized by Raman spectroscopy (Thermoscientific DXRxi Raman Imaging microscope) at 532 nm excitation wavelength and radiation power not exceeding 0.5 mW. Spectra were collected at least 3 times per sample and the average I_G/I_D ratio was calculated (primarily fitted by Lorentz and BWF functions).

3.4. Electron microscopy

3.4.1. Scanning electron microscopy

Widespread in all materials science branches, electron microscopy is an integral part of the investigation tool pack for carbon nanotubes. In this work, scanning electron microscopy (SEM) was used for visualization of SWCNTs distribution in commercial powders and in nanocomposites. For the latter ones, both TPU- and epoxy-based nanocomposite samples were broken in liquid nitrogen, and the fracture surface (with sputtered gold) was visualized (FEI Teneo; secondary electron mode, 10 kV accelerating voltage).

In aerosol CVD synthesis of SWCNTs, SEM was used for nanotube bundle length measurements. For this, a silicon substrate was located on the surface of the filter used for SWCNT film collection, and nanotubes were collected directly onto it. Yet, the collection time was reduced significantly (from minutes to several seconds) to gather individual nanotubes/bundles and avoid nanotube network formation. Deposited SWCNTs/bundles were visualized by SEM (JEOL JSM-7001F; 1 kV accelerating voltage). Next, the contour

length of SWCNTs was measured with the use of ImageJ software, and statistics with a sample size of several hundred were collected.

3.4.2. *Transmission electron microscopy*

Transmission electron microscopy (TEM; FEI Tecnai G2 F20) was utilized for the visualization of nanotubes and their bundles. Measured bundle diameters were used for the assessment of the bundling degree in aerosol CVD synthesis. Samples for TEM characterization were collected similarly: TEM lacey Cu-300 grids (Merck) were placed onto the filter and nanotubes were collected directly on the substrate (collection time was shortened as well).

3.5. Tensile tests and mechanical sensitivity measurements for elastic nanocomposites

Since SWCNT/TPU nanocomposites were fabricated as a potentially multifunctional material for soft electronic applications, it was necessary to evaluate their mechanical properties. For this, tensile tests for dumbbell-molded elastic nanocomposites were conducted (Instron 5969 tensile machine) according to ISO 37 standard. Testing was conducted at various speeds: 5 mm/min until 4 mm elongation is reached (for Young's modulus estimation) and 500 mm/min until sample failure (or maximum traverse travel is reached), so that strain at break and tensile strength was recorded as well. A digital image correlation system (Correlated Solutions, dual 5-megapixel camera setup, VIC-3D software) was used for strain measurements in the elastic region. Young's (elasticity) modulus was calculated from the linear fitting of stress-strain data in the 5% strain range (limits of elastic behavior were determined by the point of intersecting tangent lines (first

one - to the initial part of the stress-strain curve and second one – to the part of the curve with pronounced plasticity behavior).

Mechanical sensitivity (piezoresistive response) of SWCNT/TPU nanocomposites was captured along with tensile tests. For this, resistance measurements were conducted according to the four-probe scheme with a 2 cm initial distance l_0 between inner electrodes (Keithley 2400). Strain-sensing efficiency was estimated using gauge factor (GF) according to equation (15). Meanwhile, two GF values were calculated: in the elastic range and the whole one (containing both elastic and plastic regions).

3.6. THz spectroscopy for EMI-shielding efficiency estimation

In addition to strain sensing, elastic SWCNT/TPU nanocomposites were evaluated in their performance for EMI-shielding in the THz range. Transmission spectra for samples with different nanotube loadings were obtained at a time-domain spectrometer (TeraView TPS 3000). Meanwhile, both disk-molded (0.5 mm thickness) and, for highly concentrated samples, thin films (0.1 – 0.2 mm thickness) were studied. Samples were fixed on metal holders with a 6 mm aperture. Spectra were collected in the range of 4 – 100 cm^{-1} , under vacuum. Shielding efficiency SE was normalized to a sample thickness h (nSE [dB mm^{-1}]) and calculated as:

$$nSE = \frac{SE}{h} = -\frac{10 \log T}{h}. \quad (28)$$

Chapter 4. Aerosol CVD synthesis of SWCNT films

4.1. Chemical engineering of CO-based aerosol CVD reactor

4.1.1. Residence time control to tune the properties of SWCNT films

As discussed above, the aerosol CVD method for the synthesis of SWCNTs is one of the most advanced approaches to the one-stage scalable production of nanotube-based thin transparent conductive films. Moreover, the stabilization of highly diluted catalyst and nanotubes in the aerosol phase suppresses nanotube agglomeration and bundling, which is crucial for subsequent utilization of SWCNTs.

To date, aerosol CVD synthesis with CO as a carbon source and ferrocene as an iron catalyst precursor has appeared to be one of the most studied and successful implementations of aerosol CVD processes for nanotube film production. Reasonable conclusions may be drawn on the effects of reactor design (including reactor scale-up [61,62] and catalyst precursor injection strategy [69]), temperature [32,146], catalyst concentration [50,147], the addition of growth promoters (*e.g.*, CO₂, H₂O [64,77,78]) or extra carbon sources (*e.g.*, C₂H₄ [70]) on the structural parameters of nanotubes obtained. In turn, the effect of the structural properties of aerosol-synthesized nanotubes, including nanotube length [61,67] and diameter distributions [32,67,78], defectiveness [32], semiconducting/metallic ratio [76], bundling degree [147], and some others on the performance of SWCNT films-based TCFs was thoroughly studied. In particular, nanotube lengthening was shown to positively affect nanotube conductivity, which agrees with the

general understanding of nanotube network conductivity (Section 2.1.2) and reported empirical dependencies (equation (9)).

In the CVD process, nanotube length can be considered as a function of nanotube growth rate and time [53]. If the former one is mainly determined by the synthesis environment (temperature, carbon source, growth promoters), growth time may be limited by catalyst lifetime (which also depends on synthesis conditions) or residence time in the flow reactor (which is a part of reactor design). Nevertheless, controllable nanotube lengthening by residence time extension is complicated by the fundamental problem of the aerosol CVD process related to catalyst mobility. Inseparable catalyst activation and nanotube growth stages do not allow tuning exclusively residence time. There are known approaches to residence time variation implemented by reactor scale-up [61,62], injector tip position [67], and adjustment of total flow rate [68]. While the first one is impeded by technical issues (since scale-up implies a new reactor with a longer or thicker quartz tube), the second two were shown to affect synthesis design: variation in injector position leads to altered gas velocity and temperature space distribution, while flow rate changes cause a shift in SWCNT diameter distribution.

In this work, a new strategy was proposed. The reactor design used (**Figure 4**) implies two routes for gas delivery: via the main inlet (i) and the thin injector (ii). In the recent work by our research group [69], it was shown that catalyst activation is mainly determined by flow rate through the injector, and the optimal (in terms of productivity) value of 2 lpm was found. Since the velocity of gas passed through the injector is much

higher than the velocity of one that passed through the main inlet, changes in “main flow” should not significantly affect ferrocene delivery to the reactor hot zone.

Thus, the goal of the current investigation was to develop a new strategy for controllable varying residence time at the unchanged catalyst activation stage. The idea was to maintain the injector flow rate at 2 lpm and catalyst concentration (by fixing “cartridge flow” to the total flow rate ratio) and vary the total flow rate by “main flow” rate.

The total flow rate was varied in the 2.1 – 10 lpm range (lower flow rates are impossible because of the catalyst delivery approach). CO₂ as a growth promoter was added at 0.74 vol% and the reactor hot zone temperature was set at 880 °C. Temperature measurements in the centerline at different flow rates (3.0, 5.0, and 10.0 lpm) did not show noticeable shifts in the profile, so the isothermal zone was kept constant at flow rate variation. Corresponding residence time τ_{res} was estimated using the temperature profile and the geometry of the reactor (details are in SI of **Publication I**) and the 2.1 – 10 lpm flow rate range corresponded to the 17.9 – 3.8 s residence time range.

To test the method proposed, UV-vis-NIR optical spectroscopy was applied to SWCNT film synthesized at different residence times (flow rates) for extraction of SWCNT diameter distribution information. Nanotube diameter was repeatedly demonstrated in both theoretical and experimental studies to correlate with catalyst particle diameters [148–150]. Thus, the estimation of SWCNT diameter distribution from optical absorbance spectra allows to judge upon catalyst diameter and, in turn, the catalyst

activation stage. **Figure 9** displays UV-vis-NIR recorded at different τ (Q_{tot}) and estimated diameter distribution histograms.

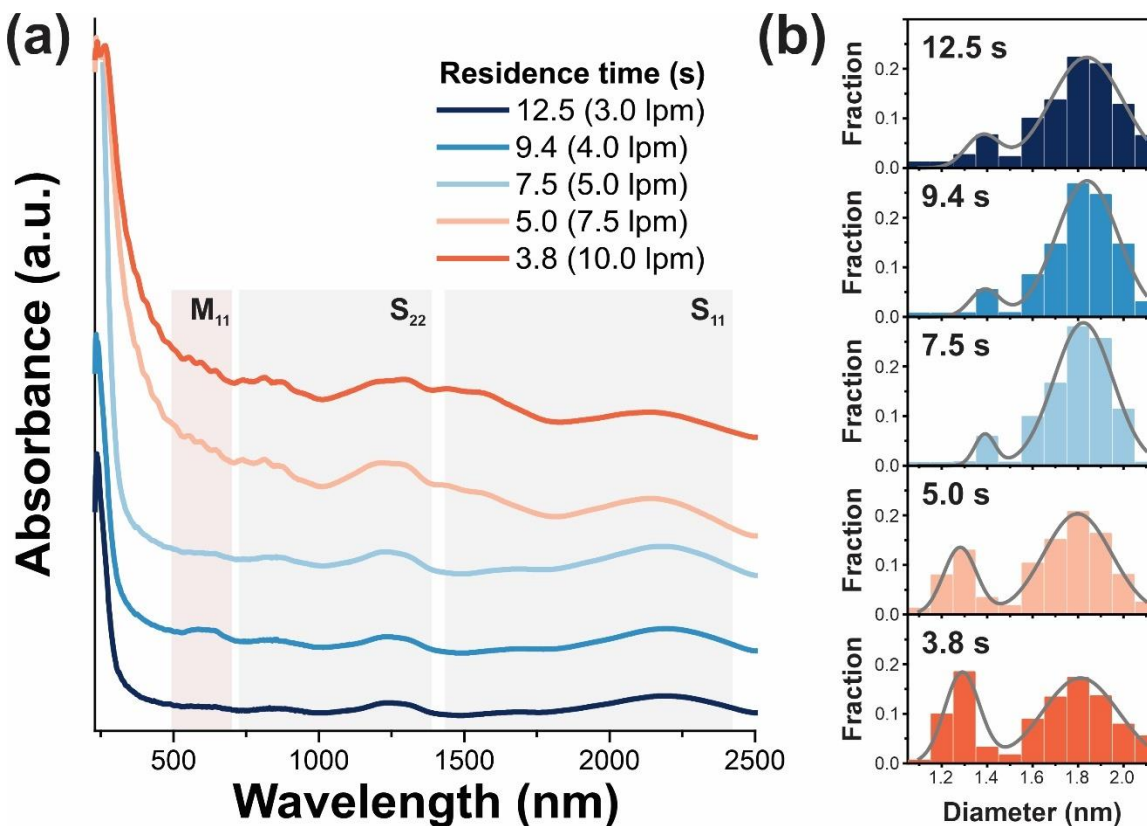


Figure 9. (a) UV-vis-NIR spectra of SWCNT films synthesized at different residence times (total flow rates); (b) corresponding nanotube diameter distribution histograms. Modified from **Publication I**.

A clear tendency of diameter distribution to bimodality is observed. As will be discussed in the following paragraphs, the reason for such an unusual catalyst activation pattern might be in the use of injector and CO₂. Nevertheless, both SWCNT diameter modes are kept rather unchanged when residence time varies but the intensity of the thin nanotube mode increases with flow rate. It can be explained by computational fluid dynamics (CFD) calculations (SI of **Publication I**) demonstrating a decrease in flow vorticity near the injector vicinity with flow rate presumably leading to a faster catalyst

feed rate to the hot zone. Pronounced turbulence at lower flow rates results in the changed catalyst activation pattern expressed in shifted diameter distributions at flow rates lower than 3 lpm (SI of **Publication I**). Thus, the residence time window of 12.5 – 3.8 s (achieved by 3 – 10 lpm flow rates) can be found in the current method. Nevertheless, maintained diameters (both modes) confirm the catalyst formation and nanotube nucleation stages could be considered the same at different residence times allowing us to examine the pure residence time effect on further results.

Next, the nanotube growth stage was investigated. In addition to length, the nanotube bundling degree characterizes this stage. Besides, nanotube yield is an important parameter, since it demonstrates the amount of nanotube material (based on film absorbance, equation (26)) and depends on nanotube number and size. In this case, diameter distribution changes are negligible, hence, yield dependency on nanotube number N and length L is sufficient for consideration:

$$\text{Yield} \sim L \cdot N. \quad (29)$$

Figure 10 compiles all the abovementioned SWCNT parameter dependencies on residence time.

SWCNT bundle length distribution was studied by analysis of SEM images and gathering statistics of bundle contour length (**Figure 10a**). Length distributions are well described by lognormal law, which is typical for aerosol processes [32,61], so geometric mean and standard deviation are used for further length discussions. The most exciting results are depicted in **Figure 10b** where bundle length dependency on residence time is shown. Nanotube lengthening with residence time is indeed observed which supports the

main idea of this study. The resulting dependency can be expressed by a power law (the validity of such an approach will be uncovered in the following paragraphs):

$$L(\tau) \sim \tau^\lambda, \quad (30)$$

where λ is a scaling law parameter describing the nanotube growth rate.

Nevertheless, it should be noted that such SEM imaging does not allow the separation of nanotubes and their bundles. Therefore, the nanotube bundle length increase might not be caused by nanotube lengthening but by higher budding degree (b) – parameter describing inter-nanotube collisions in aerosol flow, which can be estimated as a ratio of the number of nucleated nanotubes in the activation stage N to the number of resulting bundles and nanotubes N_b :

$$b = \frac{N}{N_b} = \frac{\overline{d_b}^{-2}}{\overline{d}^2}, \quad (31)$$

and as a ratio of an average bundle diameter $\overline{d_b}$ to an average nanotube diameter \overline{d} in a sample (where quadratic dependency comes from an approximation of the cylindrical geometry of nanotubes and bundles formed from them [31])

The kinetics of aerosol evolution is expressed by the equation [151]:

$$\frac{dN(t)}{dt} = -K(d_b(t)L(t))N(t)^2, \quad (32)$$

where K is a coagulation coefficient dependent on mobility particle size (d_m), which, for rod-like particles (like nanotubes) can be estimated as $d_m \sim L^{1/3}d_b^{2/3}$, and $N(t)$ describes a reduction in aerosol concentration by the coagulation process. Taking into account the power dependency of nanotube length on time (equation (30)) and bundling degree

definition (equation (31)), an estimation of bundling degree dependency on an initial number of nanotubes N and residence time τ (details are in **Appendix 1**) can be derived:

$$b(N, \tau) \sim N \cdot \tau^{\frac{3-\lambda}{2}}. \quad (33)$$

Thus, the bundling degree depends on both residence time and initial nanotube concentration. Bundling degree can be found by measuring bundle diameters using TEM images (similar to bundle length statistics). **Figure 10c** displays a typical TEM image and **Figure 10d** shows bundle diameter dependency on residence time. Since nanotube diameter distribution does not change, bundle diameter can be used for estimation of bundling degree.

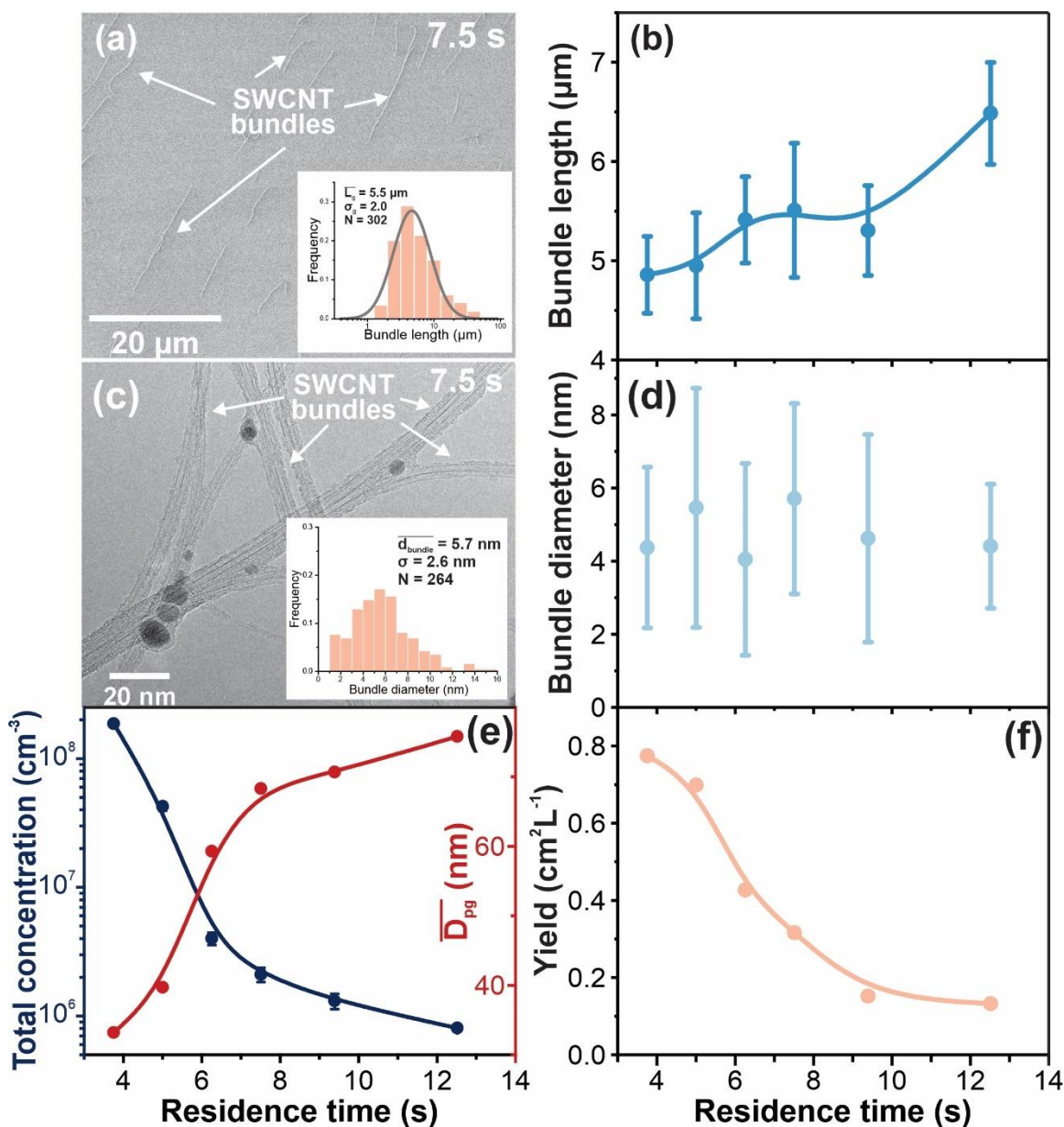


Figure 10. (a) Typical SEM image of SWCNT bundles deposited on the silicon substrate (residence time is 7.5 s) with length distribution histogram and corresponding statistics in the inset. (b) Bundle length dependency on residence time. (c) Typical TEM image of SWCNT bundles (residence time is 7.5 s) with diameter distribution histogram and corresponding statistics in the inset. (d) Bundle diameter dependency on residence time. (e) Total aerosol concentration (left axis) and geometric mean diameter of aerosol particles dependencies on residence time. (f) Yield dependency on residence time. Modified from **Publication I**.

Surprisingly, a clear trend in bundle diameter increase with residence time is not observed: it can be considered unchanged. This allows us to conclude that nanotube lengthening occurs indeed confirming the current approach to residence time variation. Yet, at the same time, an unchanged bundling degree might imply a decrease in aerosol concentration with residence time.

DMA measurements prove this assumption: total aerosol concentration dependency strongly declines with residence time (**Figure 10e**, dark-blue curve; DMA spectra can be found in **Publication I**). Meanwhile, the mean mobility diameter $\overline{D_{pg}}$ increases with residence time which correlates with length increase. Such a strong drop in nanotube concentration likely affects the yield dependency on residence time (**Figure 10f**), which drops by 7-8 times.

The strong decrease in nanotube concentration with residence time can be attributed to several factors: diffusion losses on the reactor walls since penetration decreases with residence time (i); thermophoresis losses at the outlet of the reactor where quartz tube cools down rapidly (ii); losses caused by vortices near the injector (iii); decreased in catalyst feed rate (caused by lower “main flow” rates). A thorough investigation of the abovementioned possibilities (SI of **Publication I**) results in diffusion losses and increased catalyst feed rate at higher flow rates (lower residence times) to be the dominant mechanisms behind the yield drop phenomenon. Increased catalyst activation degree, nonetheless, is not related to changes in activation pattern (which was investigated by optical absorbance spectroscopy).

Finally, the effect of residence time variation on the optoelectronic performance of synthesized SWCNT films, *e.g.*, R_{90} was investigated. Expectedly, yet, still inspiringly, nanotube lengthening positively affected SWCNT film conductivity yielding a 2.6-fold decrease in R_{90} (from 2.9 to 1.1 $\text{k}\Omega/\square$; **Figure 11a**). Nevertheless, such a considerable decrease in R_{90} is higher than expected according to equation (9). Diameter distribution and bundling degree, which could also affect film conductivity, are rather constant. An unexpected increase in I_G/I_D with residence time could be a reason for this trend (shown in **Publication I**). This phenomenon will be discussed in the next paragraphs.

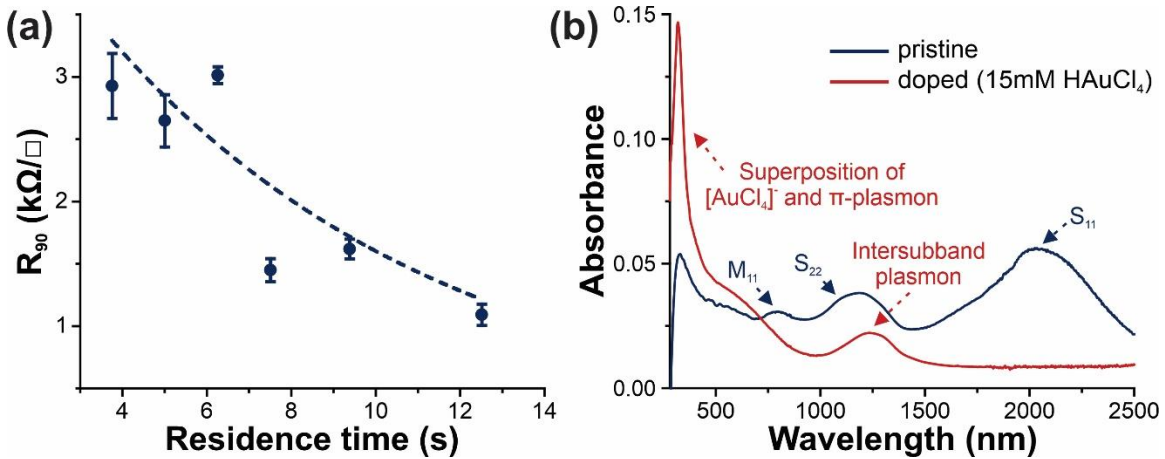


Figure 11. (a) R_{90} dependency on residence time. (b) UV-vis-NIR spectra of pristine (blue curve) and HAuCl_4 -doped (red curve) SWCNT films synthesized at the optimized conditions with highlighted absorption peaks. Modified from **Publication I**.

Nevertheless, $\text{k}\Omega/\square$ order of R_{90} for TCFs is much higher than industrial requirements of tens of Ω/\square . To approach R_{90} obtained in this study to such values, the developed here strategy to extend residence time was combined with previously found optimal for conductivity temperature (854 °C), decreased catalyst concentration (0.6 ppm), and slightly decreased CO_2 concentration (0.59 vol%) [50], to decrease R_{90} . Pristine film

with R_{90} of $245 \Omega/\square$ was obtained, which then was doped with 15 mM HAuCl_4 according to the technique published elsewhere [46]. **Figure 11a** illustrates the spectra of the SWCNT film before and after doping. A slight increase in absorbance after doping can be noticed which is associated with reduced gold nanoparticles deteriorating transparency of the film. Nevertheless, an effective decrease in Schottky barriers and saturation of nanotubes with holes resulted in such low R_{90} values as $51 \Omega/\square$.

Thus, the proposed method of residence time extension has solved several important tasks. For the first time, a fundamental possibility to separate catalyst activation and nanotube growth stages was demonstrated. This opens up broad prospects for the investigation of nanotube growth kinetics and mechanisms in the aerosol CVD process. Next, a new approach for controllable adjustment of nanotube length in the aerosol CVD process was developed. The third achievement is of practical interest: nanotube lengthening caused by residence time extension significantly decreases equivalent sheet resistance providing one more opportunity to tune the conductivity of SWCNT thin films. This methodology for the synthesis of nanotubes with controllable length was successfully applied in the development of SWCNT film-based freestanding membranes for nanoaerosol filtration (**Publication IV**) and bolometers (**Publication V**).

4.1.2. Boosting the synthesis with hydrogen

Although the described above approach to controllable residence time tuning was developed for CO-based aerosol CVD, it is quite universal and might be applicable to various carbon feedstocks. A specific significant problem of the use of carbon monoxide

as a carbon source is its high stability, which, although results in high purity of the sample, also leads to low synthesis yield as a reverse side of this coin.

As a problem solution, the introduction of growth promoters is often employed. Sulfur compounds, such as thiophene, are one of the most widely used promoters in aerosol CVD synthesis of CNTs [152]. Yet, it was shown that they decrease the adsorption energy of CO to a metallic surface, that is, are not beneficial in the CO atmosphere [153]. Another big group is weak oxidizers, such as CO₂ and H₂O which were successfully applied in CO-based synthesis [64,77,79]. Their promoting role was explained by etching excessive amorphous carbon this way cleaning the catalyst surface and equalizing balance in carbon release/incorporation in a growing nanotube [146]. At the same time, reducing additives to CO atmosphere were utilized much rarer [70,76,79,154]. Hydrogen was shown to enhance nanotube growth in the reactor with a catalyst supply system based on a hot wire generator. The positive effect was explained by preserving the generator from oxidation and additional carbon-feeding reaction (equation (17)) [79]. Yet, no detailed explanations were given. Furthermore, Anoshkin *et al.* studying the CO/C₂H₄ hybrid carbon source system found a positive hydrogen effect on the performance of SWCNT films as TCFs with H₂ addition, yet, detailed research on this phenomenon was not reported as well [70].

It is worth noting that hydrogen was utilized quite frequently in hydrocarbon-based FCCVD (including aerosol CVD). Moreover, some FCCVD processes are designed in such a way that hydrogen is used as a main carrier gas [74,155,156]. The numerical investigation reported various hydrogen influences on the FCCVD nanotube synthesis: suppression of non-catalytic pyrolysis of hydrocarbons preventing nanotube samples from amorphous

carbon impurities [56,72,73,156] (i); catalyst surface cleaning based on hydrogenation process (with methane formation, the reaction is shown in equation (18)) [157,158] (ii); and nanotube etching, including selective one (tailoring of nanotube diameter was demonstrated, which was explained by hydrogen etching of higher-reactivity thin nanotubes) [159,160] (iii). Recent works report all three effects in dependency on H₂ concentration ((i)-(iii): from the lowest to the highest ones) [157,161].

Nevertheless, neither a detailed explanation of the mechanisms of the H₂ effect in the CO atmosphere, nor its effect on optoelectronic performance (R_{90}) and process productivity (yield) have been reported so far. In this work, the hydrogen role in the improvement of the synthesis process – its productivity, *i.e.*, yield, is studied. At the same time, high attention is paid to the quality of the film, including, equivalent sheet resistance (R_{90}), defectiveness, and nanotube length.

Moreover, recently, our group has investigated the effect of different temperatures on CO-based SWCNT synthesis and different temperature regimes were found in terms of nanotube growth: low-temperature (low-T; < 900 °C) and high-temperature (high-T) one (> 900 °C) [32]. The appearance of two different regimes was explained by the phase transition of nano-sized iron from α - to γ -phase and, as a consequence, changes in nanotube growth rate-determining stages. The second part of this work was aimed to fill this gap, herewith, the hydrogen effect in both temperature regimes is investigated.

Before experiments on H₂ introduction in CO-based synthesis of nanotubes, the thermodynamics background of the possible reactions (equations (16) – (18)) was studied first. Details in calculations based on temperature dependency of heat capacity (Shomate

equation), Gibbs free energy ($\Delta_r G^0$) and Arrhenius equation are shown in **Appendix 2**. Final dependencies of Gibbs free energy of reactions (16) – (18) on temperature and equilibrium concentration of CO₂, H₂O, and CH₄ on introduced H₂ concentration (c_{H_2}) at 880 °C are shown in **Figure 12**. Carbon-producing reactions (16) and (18) demonstrate similar thermodynamic behavior with positive values of $\Delta_r G^0$ at temperatures higher ~ 700 °C indicating a prevalence of reverse reaction direction. Therefore, the synthesis of nanotubes is pushed by kinetic reasons. Equilibrium concentrations plotted versus c_{H_2} in **Figure 12b** points to the gradual shift to carbon synthesized by the reaction between CO and H₂ rather than by the CO disproportionation with c_{H_2} increase. Yet, fraction of methane formed via carbon hydrogenation increases as well (reaction (18)). Nevertheless, since no CO₂ and H₂O are artificially introduced into the reactor, quotients of the reactions (16) and (17) (**Appendix 2**) indicated the formation of carbon by both reactions coupled with corresponding CO₂ and H₂O. Thus, with the H₂ introduced at moderate concentrations, we might deal with additional reactions feeding the system with carbon in addition to the Boudouard reaction, which could enhance the synthesis productivity.

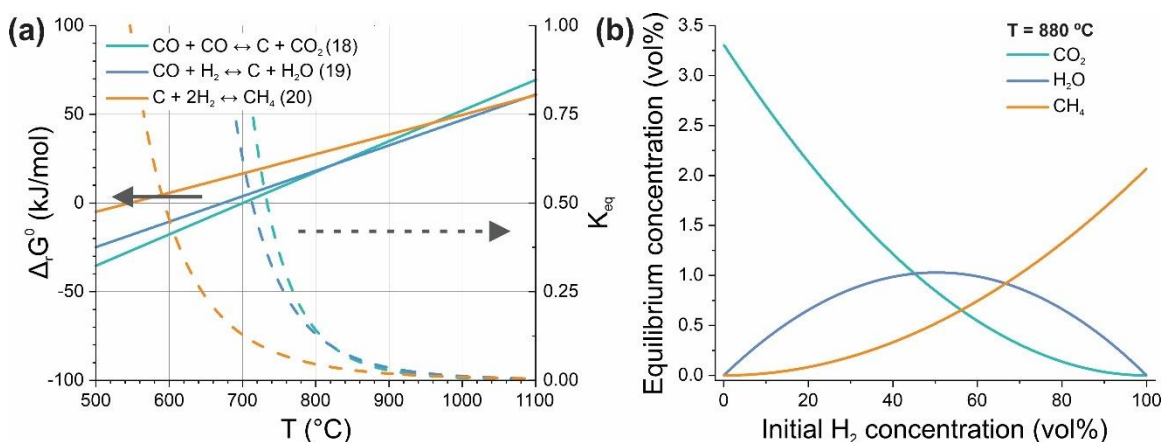


Figure 12. (a) Dependencies of Gibbs free energies of reactions (16) – (18) ($\Delta_r G^\circ$) (left y-axis) and corresponding equilibrium constants (K_{eq}) (dashed curves; right y-axis) on temperature; (b) Dependency of equilibrium concentrations of CO_2 , H_2O , and CH_4 on the initial H_2 concentration introduced to CO at 880 °C.

Experiments on the introduction of H_2 in CO-based synthesis started with the well-studied conditions (including those described in the previous paragraph) referring to the low-T regime: the 880 °C reactor hot zone temperature. At the same catalyst concentration of 0.9 ppm and residence time of 7.5 s (5 lpm total flow rate) without introduced CO_2 (to study pure H_2 effect), H_2 concentration was varied in the range of 0.5 – 40 vol%. It is worth noting that the choice of temperatures highly above 700 °C, where both CO disproportionation (reaction (16)) and hydrogenation (reaction (17)) become thermodynamically suppressed (**Figure 12a**), is due to the kinetics of the nanotube growth. In early works devoted to CO-based aerosol CVD synthesis [79,146], essential nanotube growth was found only at temperatures above 800 °C. Besides, recently, the highest length of the SWCNTs obtained at the same aerosol CVD reactor has been found in the 850 – 880 °C temperature range [32].

Figure 13a represents UV-vis-NIR spectra of SWCNT films obtained with H₂ added to the CO atmosphere. Spectra are pretty similar indicating similar diameter distributions. At the highest c_{H_2} (40 vol%), no noticeable characteristic peaks can be found, which, together with the loss of transferability of the synthesized samples, point to limits of hydrogen concentration used in the synthesis. Nevertheless, two features can be observed with H₂ addition: a slight redshift of the S₁₁ peak (meaning slight nanotube thickening) and a formation of a second subpeak of the S₁₁ peak (evident at $c_{H_2} \approx 5.0$ vol%), which intensity gradually prevails over the main one, indicating the bimodal diameter distribution of nanotubes. The second one may imply a new pathway in the catalyst activation stage caused by H₂ introduction, in particular, by another carbon-feeding reaction (17).

This assumption is supported by an enormous yield increase with c_{H_2} (**Figure 13b**). A 15-fold increase in synthesis productivity (from 0.034 to 0.55 cm²L⁻¹) is observed, which reveals the remarkable practical potential of adding H₂ to CO. According to equation (29), yield is determined mainly by nanotube concentration and length. Nevertheless, according to the principles of SWCNT network conductivity (Paragraph 2.1.2) and experimental observations (equation (9)), nanotube lengthening would lead to film conductivity increase (*e.g.*, R_{90} decrease), which, however, does not take place (**Figure 13c**). No considerable changes in R_{90} can be noted until high concentration (>10 vol%) are reached where R_{90} soars (where the synthesis conditions are already far from optimal), which lead to the conclusion that SWCNT lengthening barely happens and a huge increase in the yield originates from the increase in nanotube concentration, that is the increase in catalyst

activation degree. SWCNT film I_G/I_D reflecting defectiveness demonstrates bell-shaped dependency on c_{H_2} , which could be responsible of slight lowering of R_{90} at the medium c_{H_2} (Figure 13c-d).

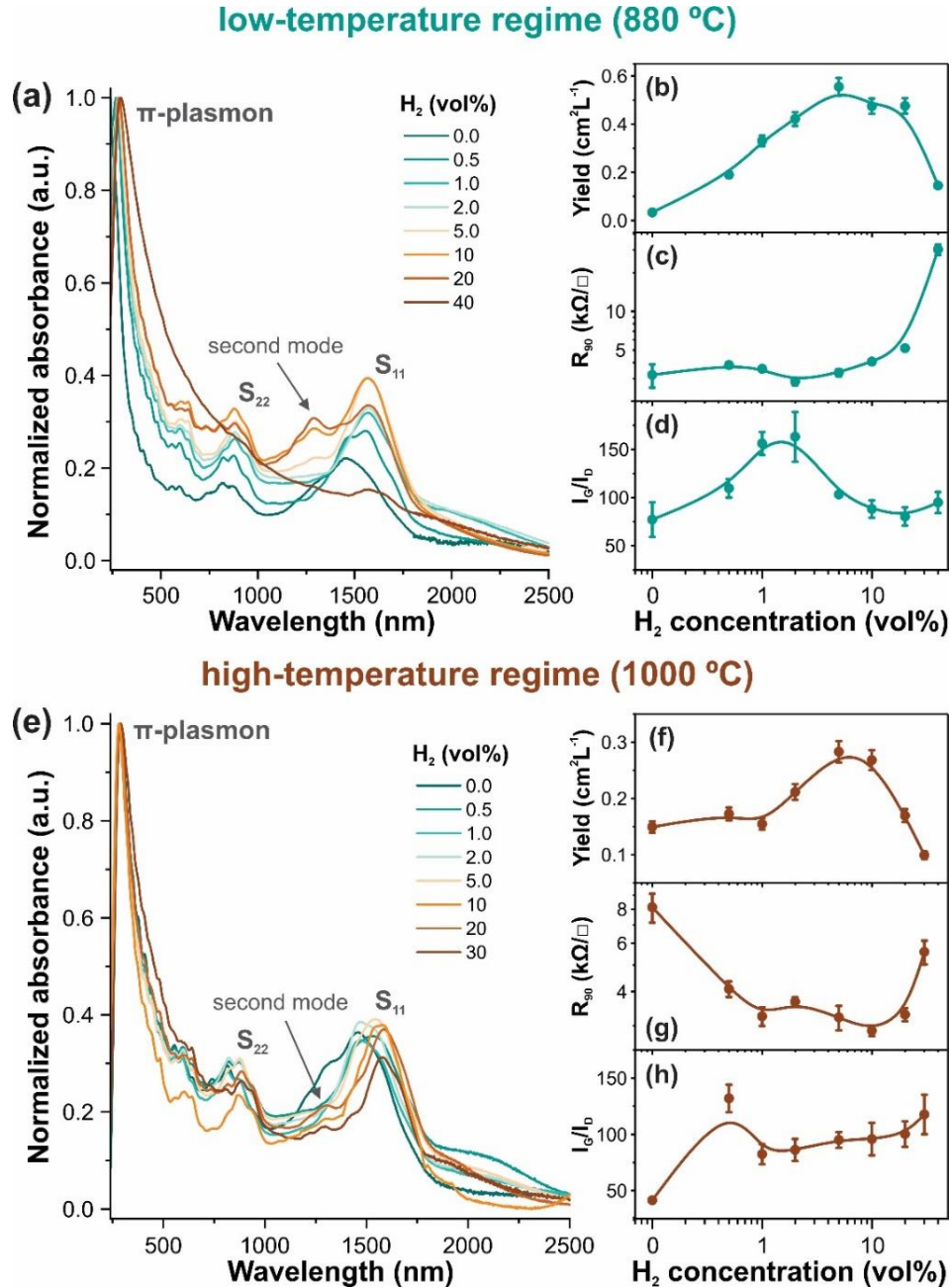


Figure 13. (a, e) Optical absorbance spectra of the SWCNT films synthesized with the addition of H_2 (concentration is shown in the legend); with indicated second mode in SWCNT diameter distribution (at

$c_{H_2} \approx 5.0 \text{ vol\%}$); Dependencies of the yield (**b, f**), R_{90} (**c, g**), and I_G/I_D (**d, h**) on c_{H_2} . (**a-d**) figures correspond to the low-T regime (880 °C); (**e-h**) figures - to the high-T one (1000 °C).

The experiment and the protocol of measurements for the investigation of the H_2 effect in the high-T regime (1000 °C) of SWCNT synthesis were repeated. Quite similar tendencies in optical spectroscopy and yield dependency can be found (**Figure 13e-f**). Yet, the second S_{11} subpeak is less pronounced and the yield increase is more moderate (by 2-3 times). However, generally higher synthesis productivity at higher temperatures (from 0.034 to 0.15 cm^2L^{-1}) should be noted, which is in agreement with previous results [32].

A R_{90} -vs- c_{H_2} trend (**Figure 13g**) appeared to be significantly different compared to that found in the low-T regime: a three-fold decrease in R_{90} is observed at the medium c_{H_2} (5 – 10 vol%). Now, unlike low-T regime, a length-driven process explaining the simultaneous increase in the yield and decrease in R_{90} is quite possible. To verify this hypothesis, direct length measurements by gathering bundle length statistics visualized by SEM (**Figure 14**) were conducted. Typical lognormal law-described length distributions (**Figure 14a1-d1**) tend to shift to longer bundles at $c_{H_2} = 5.0 \text{ vol\%}$. **Figure 14e** illustrates geometric mean bundle length dependency on c_{H_2} with a prominent maximum at 5.0 vol% (increase from 0.8 to 1.9 μm), which is in excellent correlation of conductivity trend (**Figure 13g**) and confirms length-determined results. Besides, I_G/I_D increases c_{H_2} , which could also affect decrease in R_{90} (**Figure 13h**).

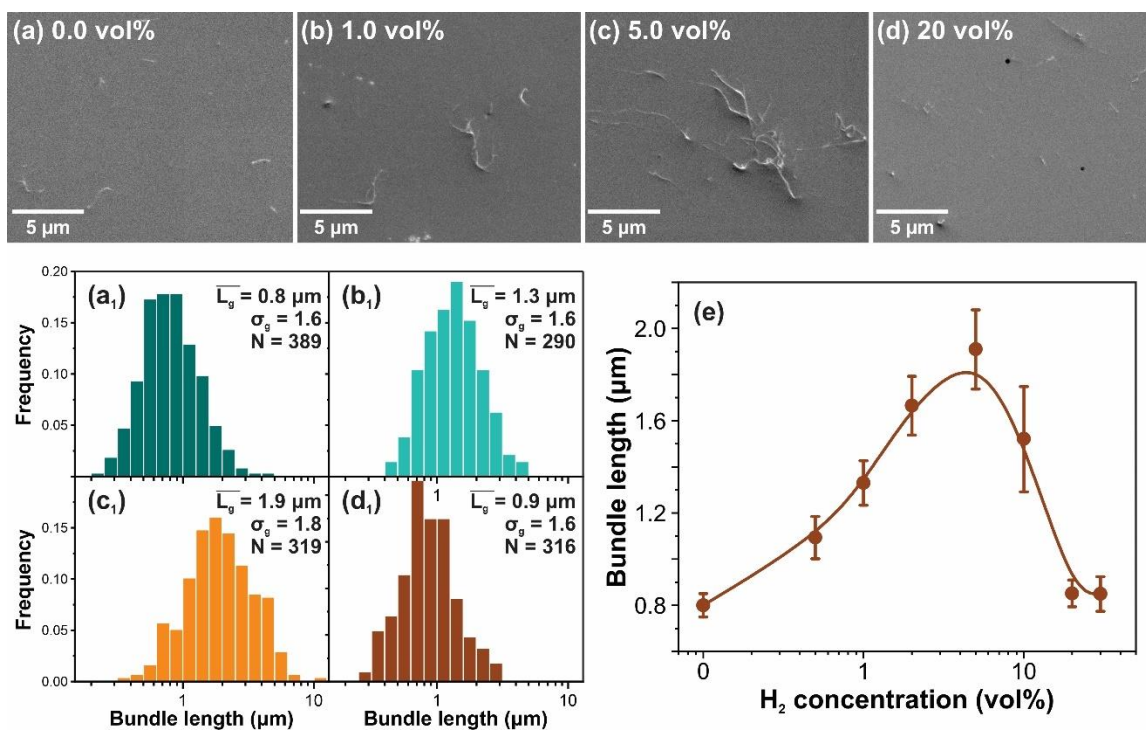


Figure 14. (a)-(d) Typical SEM images of SWCNT bundles synthesized in high-T regimes at different c_{H_2} (indicated in the figure) with (a₁) - (d₁) corresponding length distribution histograms with statistics results. (e) Dependency of nanotube bundle length on c_{H_2} in high-T regime.

The H₂ effect in CO-based synthesis of SWCNTs in different temperature regimes is summarized in **Table 2**.

Table 2. H₂ influence trends on different stages of SWCNT synthesis in low- and high-T regimes.

Regime	Activation stage (SWCNT diameter)	Growth and deactivation stages		
		Yield (synthesis productivity)	R_{90} (film conductivity)	I_G/I_D (nanotube defectiveness/quality)
Low-T	Diameter increase; formation of the intense second mode of thinner SWCNTs	~ 15-fold ↑ (~ 5 vol%)	Not improved	2-fold ↑ (~ 2 vol%; bell-shaped dependency)
High-T	Diameter increase; formation of the slight second mode of thinner SWCNTs	~2-4-fold ↑ (~ 5 – 10 vol%)	3-fold ↑ (~ 10 vol%)	2-fold ↑ (~ 20-30 vol%; steady increase)

The common effect of a slight diameter increase (expressed in the slight S_{11} peak redshift) may be explained by the dilution effect. Indeed, relatively high c_{H_2} are reached (up to 40 vol%) which could lead to a shortage of carbon source. An identical experiment on dilution but by N_2 instead of H_2 gave the same results (**Appendix 3**).

Meanwhile, deviations in the H_2 effect in the different temperature regimes may be briefly summarized as follows: in the low-T regime, H_2 strongly affects the activation stage resulting in increased nanotube concentration and, in turn, yield, while growth stage is rather maintained; in high-T regime, H_2 affects both stages, but activation degree is already high because of higher temperature and H_2 effect is quite moderate (slight S_{11} subpeak), while growth stage is affected considerably resulting in 2.4-fold increase in length leading to both yield and conductivity increase. Nevertheless, both effects are likely to come from an additional carbon-feeding reaction (17), which is reflected in an extra pathway in catalyst activation (S_{11} subpeak formation).

Such differences are explained by different growth rate-limiting stages. For the low-T regime, two possible options were given [32]: ~ 180 kJ/mol activation energy indicated either CO dissociation on α -Fe NPs or bulk diffusion in the catalyst cementite phase (Fe_3C). According to the present results, the latter is unlikely since an additional carbon-feeding reaction between CO and H_2 (17) would enhance growth in this case. Thus, thanks to the present results, a dominant mechanism in SWCNT growth rate-determining reaction may be proposed: carbon diffusion in the catalyst cementite phase.

Nanotube growth enhancement in the high-T regime can be realized in two scenarios: H_2 extends the catalyst lifetime or accelerates growth. The probability of the

former can be tested in a residence time variation experiment (described in previous Section 4.1.1). Synchronous declines in R_{90} (similar to observed in the low-T regime, shown in **Figure 11**) indicate residence time does not exceed catalyst lifetime (**Appendix 3**) pointing to a higher probability of increased growth rate than catalyst lifetime. This signifies that the growth-limiting stage was overcome. In the high-T regime, a similar duality to the low-T was discussed: the rate-limiting stage could be either CO dissociation or carbon diffusion in γ -Fe catalytic NPs. Now, vice versa, extra carbon released via reaction (17) could barely enhance growth if carbon diffusion is a bottleneck – it would rather lead to catalyst deactivation by encapsulation in an excessive carbon shell. Thus, again thanks to the results of the H_2 effect, the conclusion can be drawn that in the high-T regime, CO dissociation limits nanotube growth.

Thus, H_2 affects CO-based SWCNT synthesis in a complex manner and its influence strongly depends on the temperature regime used. In the low-T regime (< 900 °C), it greatly improves synthesis productivity by increasing catalyst activation degree via another carbon-producing reaction between CO and H_2 . Nevertheless, this reaction leads to a different effect in the high-T regime (> 900 °C), which is explained by different nanotube growth rate-limiting stages: H_2 improves both nanotube film yield and conductivity by accelerated nanotube growth resulting in longer SWCNTs. These mechanisms are schematically represented in **Figure 15**.

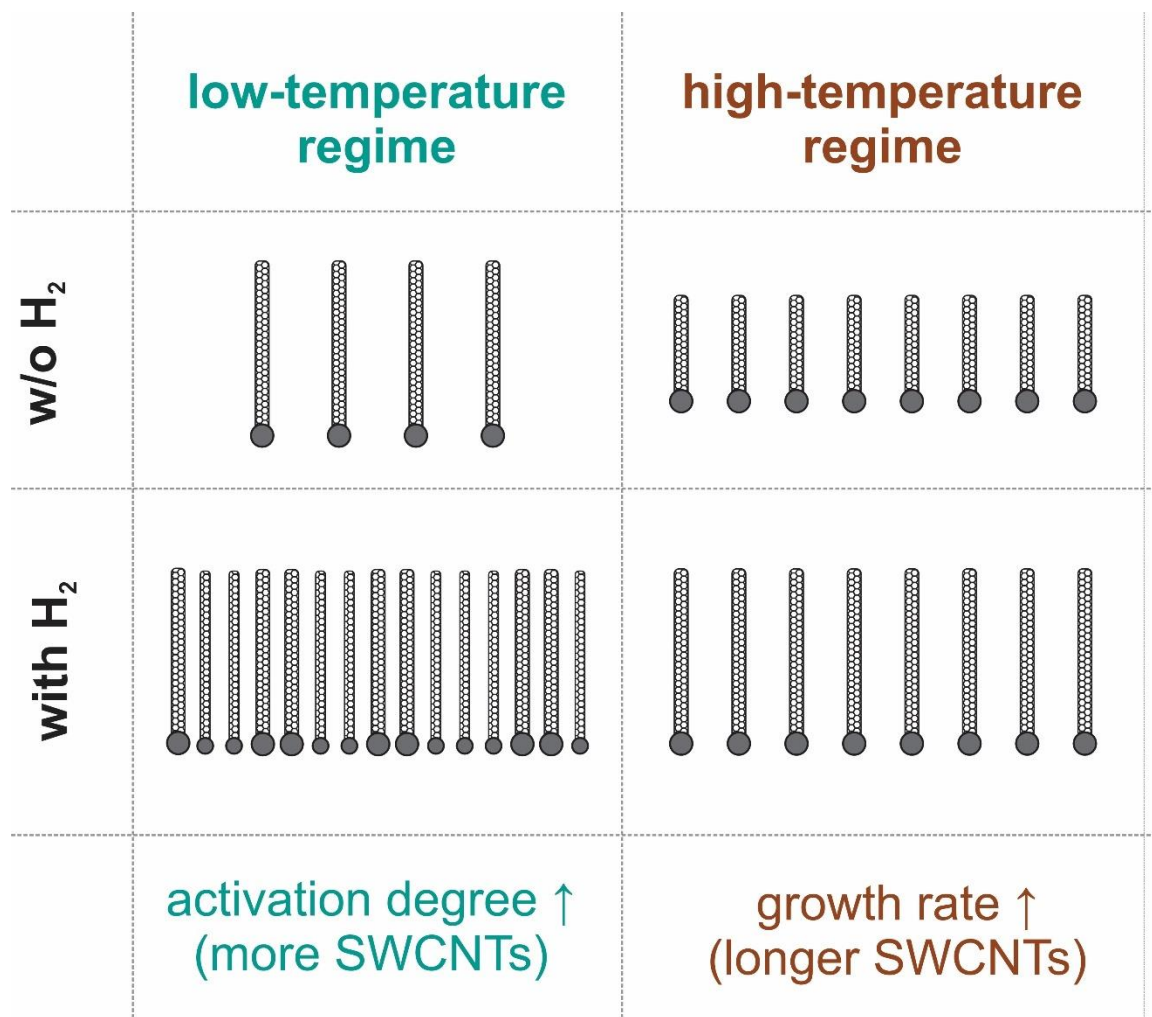


Figure 15. Schematic illustration of the H₂ effect in different temperature regimes.

Thus, for the first time, hydrogen was demonstrated as an effective growth promoter in CO-based aerosol CVD synthesis of SWCNT films. A significant yield increase (by ~ 15 times) appeared to be the highest compared to that achieved by the addition of other growth promoters (~3-fold yield increase achieved by C₂H₄ [70], and ~ 2.1-fold improvement obtained by CO₂ in the works [77,162] and ~ 12.8 in [32]). Such a strong boost in process productivity can greatly improve SWCNT film production by increasing yield/R₉₀ ratio, which can be easily fitted to the other approaches to conductivity

optimization (including the residence time extension proposed above). At the same time, these results reveal uncovered mechanisms in SWCNT growth, crucial for the general development of nanotube CVD synthesis.

4.2. Fast evaluation of nanotube growth kinetics

As was mentioned above, one of the most challenging and fundamental problems of the FCCVD process caused by catalyst mobility is reactor scaling. To estimate practical benefits from scaling, that is, possibilities to improve process productivity or material properties by reactor scaling, nanotube growth termination should be assessed, *e.g.*, catalyst lifetime should be determined. Typically, this problem is solved by direct kinetics assessment, which includes a collection of nanotubes at different residence times and measuring their length.

Both procedures may be quite complicated. The problems of residence time control were discussed above (Section 664.1.1), while length measurement approaches are usually based on time-consuming measurements of bundle contour length visualized by SEM or AFM (already applied in this work). There are also less popular methods based on dynamic light scattering [163,164], rheology tests [165], THz spectroscopy [166], and some others, which, however, have their limitations and require additional specific equipment.

The approach to controllable residence time tuning proposed in this work (Section 664.1.1) solves the first task. Yet, length evolution with residence time could be extracted from that method too. Indeed, for numerical tasks, precise determination of length is not needed but qualitative estimations on nanotube growth rate are. In that task, the goal was to lengthen nanotubes for optimizing film conductivity. However, an opposite task can be

set: can a remarkable correlation between nanotube residence time trends of length and conductivity (**Figure 10b** and **Figure 11a**) be used for the estimation of nanotube growth kinetics?

The objective of this part of the work was to develop a new method for fast evaluation of nanotube growth kinetics in aerosol CVD. For this, the correlation of R_{90} -vs- τ and L -vs- τ trends are investigated at different synthesis conditions, which might affect growth kinetics. Besides, since, in addition to length, nanotube conductivity is determined by nanotube diameter distribution, defectiveness, and bundling degree, the evolution of these structural parameters with residence time was studied as well. CO_2 concentration is selected as a parameter affecting synthesis conditions since its growth promotion activity depends on its concentration. Moreover, despite the CO_2 role in CO-based aerosol CVD synthesis was studied quite thoroughly, its effect on catalyst deactivation, hence, nanotube kinetics during all the growth stages, has not been studied so far. Therefore, as an application of the proposed approach, the CO_2 effect on catalyst deactivation is studied as well.

Residence time (τ) and CO_2 concentration (c_{CO_2}) were varied and the dependency of the synthesized film properties in this two-parameter space was investigated. As the most studied and the closest-to-optimal conditions in terms of yield/ R_{90} ratio, the low-T regime (880 °C) and moderate catalyst concentration (0.9 ppm) are examined. In total, there were 42 points collected (seven points of τ (3.8 – 12.5 s) and six points of c_{CO_2} (0.00 – 1.49 vol%)). **Figure 16** complies two-parameter dependencies of R_{90} , yield, I_G/I_D ratio, and bundle length. Herewith, horizontal trends are of consideration, that is, the evolution

of these parameters with time at different c_{CO_2} . Diameter distributions are not shown in **Figure 16**, yet, UV-vis-NIR spectra of SWCNT films obtained in different regions of τ and c_{CO_2} are depicted in **Appendix 4**. Similar to what observed for residence time variation above (Section 4.1.1), no changes in the spectra with residence time variation are found (while c_{CO_2} affects significantly) which supports the universality of the method on residence time variation.

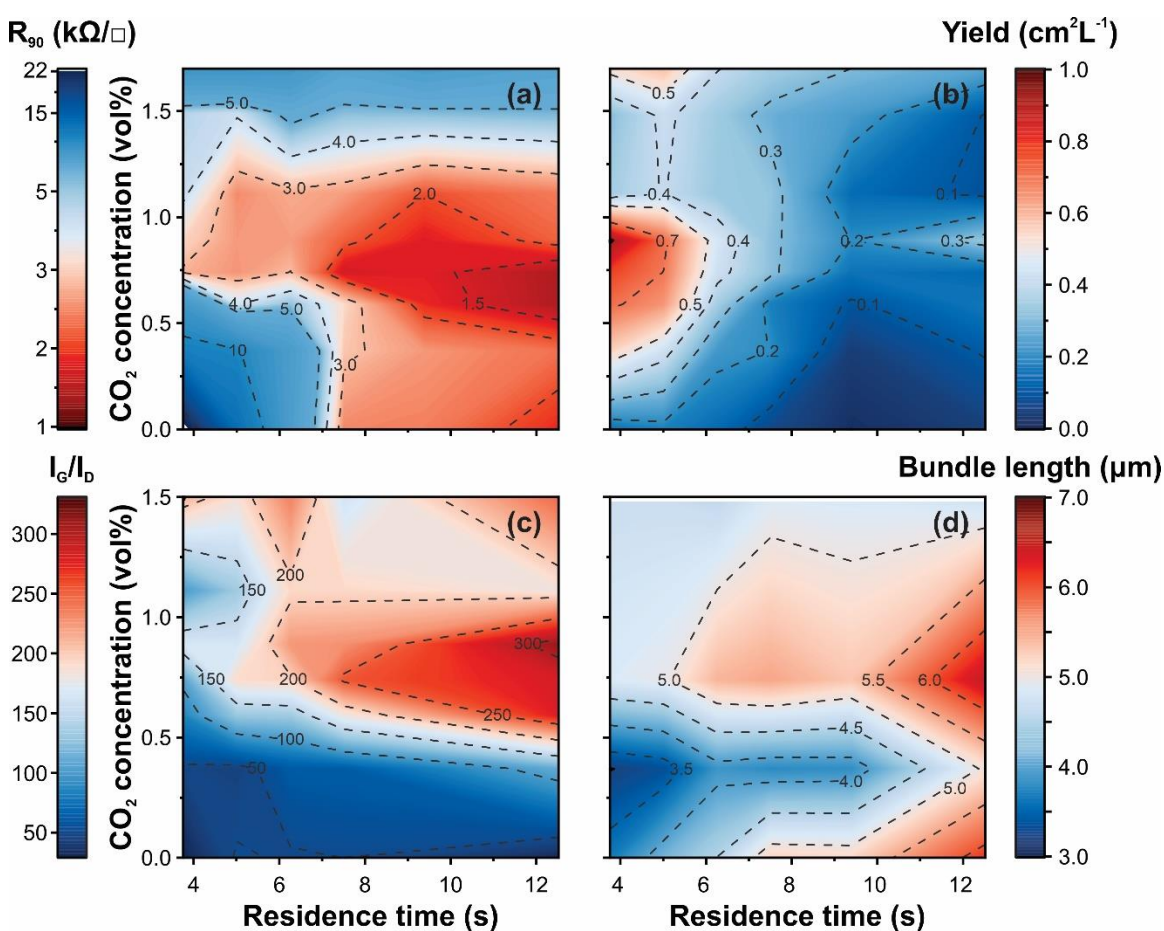


Figure 16. Contour plots representing two-parameter (τ and c_{CO_2}) dependency of (a) R_{90} , (b) yield, (c) I_G/I_D ratio, and (d) bundle length of SWCNT films.

Except for the yield, all the other parameters have a hot spot at the longest τ and medium c_{CO_2} . Nevertheless, in contrast to I_G/I_D , R_{90} and length change with τ is the highest at low c_{CO_2} (<0.5 vol%), where I_G/I_D is rather constant. At the same time, all the parameters improve with τ at moderate c_{CO_2} (0.5 – 1.2 vol%) and do not considerably change at the highest ones (>1.2 vol%). Yield tends to decline with τ in the whole c_{CO_2} considered, which is explained by universal (independent on c_{CO_2}) reasons attributed to the specifics of a flow reactor (diffusion losses and decreased catalyst activation, details are in Section 4.1.1).

Bundle length tendencies were obtained by analysis of SEM images visualizing SWCNT bundles (similar to what was executed in Sections 4.1.1 and 4.1.2). Typical SEM images of nanotube bundles obtained in different regions of τ and c_{CO_2} with corresponding length distribution histograms are demonstrated in **Appendix 4**. The highest increase in the length is observed for SWCNT synthesized without CO₂ added, and no growth at all – at the highest one of 1.49 vol%. Nevertheless, to associate these bundle length trends with nanotube growth kinetics, bundle and nanotube length interrelation should be proved. This was performed similarly to that described in Section 4.1.1 by investigation of SWCNT bundle degree dependencies. Typical TEM images and bundle diameter dependency on residence time at different c_{CO_2} are compiled in **Appendix 4**. Surprisingly, no noticeable changes at both τ and c_{CO_2} variations were revealed. This finding answers several important problems at once: relatively constant bundling degree indicates nanotube bundle length increase is caused by nanotube lengthening and not by inter-nanotube collisions in aerosol flow (i); bundling degree contribution to R_{90} -vs- τ can be neglected (ii); bundling

can be excluded from the possible causes for nanotube growth termination (which was assumed in some works devoted to the aerosol CVD [147]) (iii).

Thus, indeed, nanotube length and R_{90} are correlated. **Table 3** represents the overall trends of SWCNT parameter evolution with time at different c_{CO2} ranges. For ease of evaluation of parameters' interrelations, "equivalent sheet conductivity" σ_{90} as an inverse parameter to R_{90} is used:

$$\sigma_{90} [\square/\Omega] \equiv \frac{1}{R_{90}}. \quad (34)$$

Table 3. Representation of the overall trends of SWCNT structural parameters with residence time increase at different c_{CO2} ranges.

c_{CO2} range	σ_{90}	Yield	length	I_G/I_D	bundling
low (< 0.5 vol%)	↑↑↑	↓↓	↑↑	○	○
medium (0.5 – 1.2 vol%)	↑↑	↓↓	↑	↑	○
high (>1.2 vol%)	○	↓	○	○	○

The trends illustrated in **Table 3** can be represented quantitatively. For this, scaling law form can be used (similar to equations (30) and (33)):

$$L \sim \tau^\lambda, \quad (35)$$

$$b \sim N \cdot \tau^{\frac{3-\lambda}{2}} \sim \tau^\beta, \quad (36)$$

$$\sigma_{90} \sim \tau^r \quad (R_{90} \sim \tau^{-r}), \quad (37)$$

$$\text{Yield} \sim L \cdot N \sim \tau^{-\gamma}, \quad (38)$$

$$\frac{I_G}{I_D} \sim \tau^\kappa, \quad (39)$$

where equation (35) essentially duplicates equation (30) (for ease of perception), and powers λ , β , r , γ , and κ characterize the rate of parameter change with residence time τ

and depend on synthesis conditions, in this case, c_{CO_2} . For the determination of values of the powers, linear fitting of the dependencies (35) – (39) plotted in log-log scales is applied. **Figure 17** contains such dependencies of σ_{90} and length and the resulting powers for σ_{90} , length, I_G/I_D , and bundling degree (as the parameters affecting σ_{90}) scaling laws obtained for different c_{CO_2} . The total results of residence time dependencies of all the parameters (including yield) plotted in both linear and log scales as well as power values obtained from fitting results are compiled in **Appendix 4**.

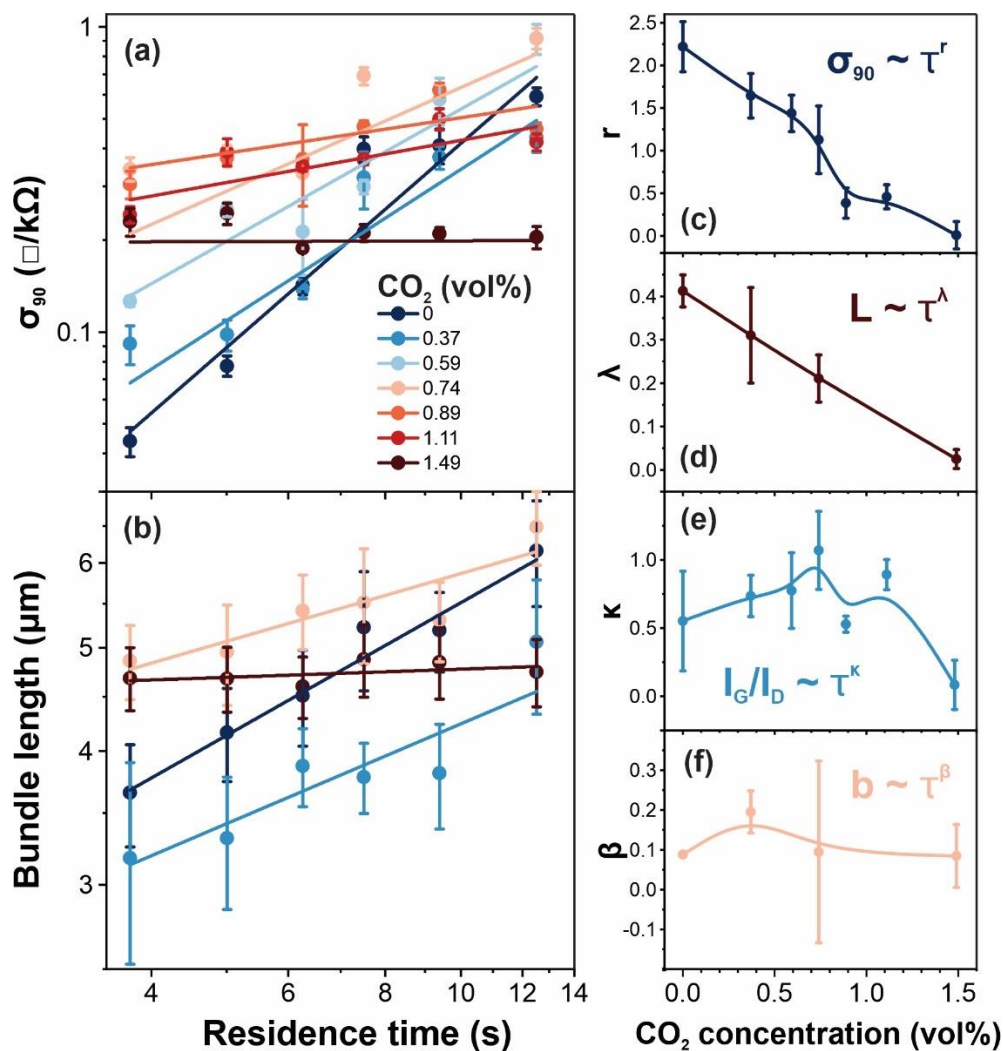


Figure 17. (a) σ_{90} and (b) bundle length (L) plotted versus τ in log-log scales; dependencies of the scaling powers (c) r (σ_{90} -vs- τ), (d) λ (L -vs- τ), (e) κ (I_G/I_D -vs- τ), and (f) β (b -vs- τ).

Essentially, **Figure 17** repeats the trends depicted in contour plot form (**Figure 16**), however, in such representation, changes in the parameters with time, including, nanotube growth kinetics, can be evaluated quantitatively. In particular, a clear correlation between σ_{90} and bundle length trends can be observed, while the other parameters determining film conductivity – defectiveness and bundling degree, demonstrate completely a different pattern.

Thus, from the method on controllable residence time variation (Section 4.1.1), a new method of fast evaluation of nanotube growth kinetics follows. By comparative analysis of R_{90} -vs- τ trends obtained at different synthesis conditions, which can be collected much faster than length measurements, it is possible to estimate growth features, including its termination which allows assessing prerequisites for subsequent reactor scaling. The validity of this method is confirmed by the unchanged SWCNT diameter and bundling degree with residence time, which arises from the reactor design. Defectiveness seems to affect to a lesser extent.

In particular, the applicability of this approach can be demonstrated for an explanation of the CO₂ effect on nanotube growth kinetics and catalyst deactivation. Since this problem refers rather to mechanistic aspects of aerosol CVD synthesis than assembling SWCNT networks, it will be discussed here briefly. **Figure 17b** indicates the *overall* nanotube growth slows down with c_{CO_2} . Yet, bundle length at the shortest τ is the highest for the highest c_{CO_2} . It means that with c_{CO_2} increase, initial growth rate increase but catalyst lifetime shortens leading to fast growth termination (and, hence, impracticability of reactor scaling), which is, however, typical for CVD nanotube growth [167].

Changes in growth rate and time might be caused by changes in diameter distribution with CO₂ addition (reflected in optical spectra in **Appendix 4**). Due to its etching activity, CO₂ leads to postponed catalyst activation causing nanotube thickening (in this case reflected in the formation of a second mode of thicker nanotubes due to the features of the injection strategy). A quadratic increase in catalyst site surface area with a linear increase in carbon demand for growing nanotubes likely results in an imbalance in

carbon release and consumption, which could lead to catalyst deactivation by encapsulation in excessive carbon. At the same time, the increase in the initial rate can be explained by overcoming the growth-limiting stage – carbon diffusion in the cementite phase of the catalyst found above (Section 4.1.2). CO₂ postponing carbon precipitation on catalyst shifts Fe-C phase diagram which could suppress cementite formation in α -phase Fe NPs (which was demonstrated by Wirth *et al.* [168] and discussed by Anisimov *et al.* in terms of CO-based aerosol CVD [146]).

Moreover, this complex CO₂ influence results in I_G/I_D -vs- τ trends (**Figure 16c** and **Figure 17e**). Taking into account quite high defectiveness ($I_G/I_D \sim 50$) at low c_{CO_2} , it might originate from non-optimal growth conditions and amorphous carbon (not etched without CO₂). With c_{CO_2} increase, since defects are mainly located in nanotube ends [169] at optimized conditions, an increase in nanotube length leads to I_G/I_D increase with τ and high κ values at the medium c_{CO_2} , while constant length at the highest c_{CO_2} results in maintained I_G/I_D .

Thus, by the method of fast kinetics assessment, CO₂ influence on both nanotube growth rate and catalyst deactivation was studied as well. In particular, for the first time, a CO₂-caused increase in the nanotube growth rate and decrease in catalyst lifetime in the CO-based aerosol CVD was found and explained.

Summing up, in this chapter, several approaches to optimization of SWCNT films synthesized in CO-based aerosol CVD process were proposed. Residence time extension was demonstrated to significantly decrease SWCNT film R_{90} by nanotube lengthening, while, at the same time, allowing to separation of catalyst activation and nanotube growth

stages, which was developed to the proposition of a new fast method to evaluate SWCNT kinetics and catalyst deactivation. By this method, CO₂ influence on the kinetics feature of the CO-based aerosol CVD process was explained. The use of H₂ was shown to significantly improve the productivity of the synthesis which opens up practical prospects for scalable production of SWCNT films utilized as TCFs. Meanwhile, different temperature regimes were found and H₂ influence in each one was thoroughly investigated and explained.

Chapter 5. Fabrication of SWCNT/polymer nanocomposites

5.1. Multifunctional elastic SWCNT/TPU nanocomposites

While SWCNT thin films as quasi-2D macroscale networks are applied mainly as TCFs, conductive SWCNT/polymer nanocomposites containing 3D nanotube networks are more functional because of the polymer matrix. In particular, elastomer-based conductive nanocomposites are excellent materials for soft lightweight stretchable and flexible electronics. Nevertheless, as discussed in Section 2.3.1, the crucial problem in nanocomposites is the homogeneity of nanotube dispersion, which affects all the final properties of the material. Spatial distribution of SWCNTs in SWCNT/TPU nanocomposites with different nanotube concentrations, which were manufactured by coagulation precipitation technique (CP) implying immediate nanocomposite formation, were estimated by SEM (**Figure 18**).

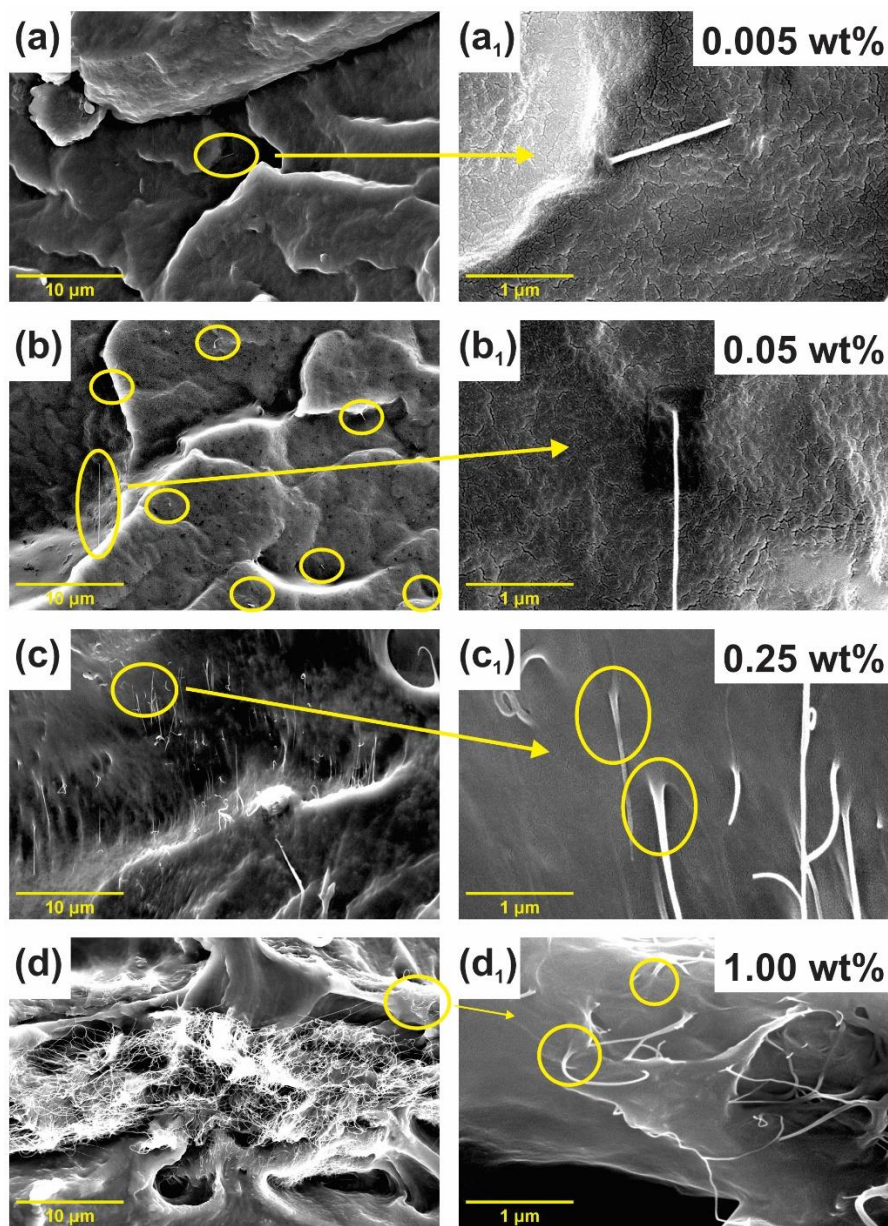


Figure 18. SEM images of fracture surface of SWCNT/TPU nanocomposites with different nanotube concentrations: (a) 0.005 wt%, (b) 0.05 wt%, (c) 0.25 wt%, (d) 1.00 wt%; yellow circles highlight SWCNTs/bundles enlarged in corresponding magnified images (a₁)-(d₁); yellow circles in the magnified images highlight nanotubes pulled out of the polymer indicating high TPU wetting. Modified from **Publication II**.

At the lowest concentration of 0.005 wt%, only individual SWCNTs/bundles randomly located in the TPU matrix may be found. At the higher concentrations, uniform

SWCNT distribution can be observed until the highest concentrations (1.00 wt%) where 10-20 μm scale agglomerates are formed (**Figure 18d**). A high dispersion degree is believed to be achieved by effective dispersion techniques (homogenization and ultrasonication) and quick nanocomposite formation by CP, although, at high nanotube loadings, dispersion is complicated by high suspension viscosity. Besides, magnified SEM images (**Figure 18c₁-d₁**; additional SEM images are shown in **Figure A9, Appendix 5**) illustrate the gradual thickening of bundles approaching the TPU matrix (the region where nanotubes are pulled out of the polymer, highlighted in **Figures 18** and **A9**). This might indicate high TPU wetting of nanotubes, which could be attributed to the high affinity of TPU to nanotubes and agrees with the reported data [170,171]. Thus, SEM analysis reveals quite good prerequisites for nanocomposite properties achieved by high dispersion degree.

Nanocomposite conductivity was tested by impedance spectroscopy technique. Frequency dependencies of conductivity (Bode charts) of the nanocomposites with different nanotube loadings are shown in **Figure 19a**.

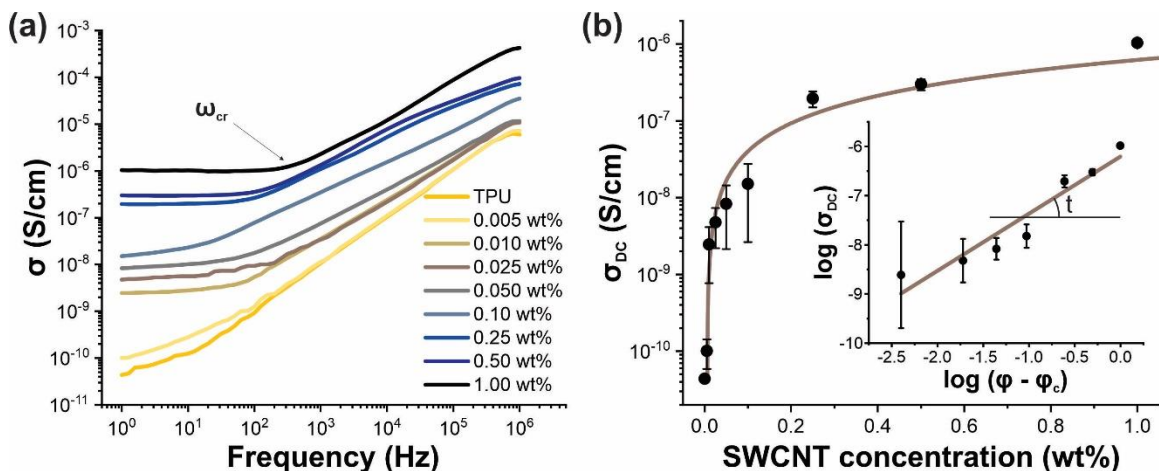


Figure 19. (a) Conductivity dependencies on frequency for SWCNT/nanotube nanocomposites with different concentrations (shown in legend) with highlighted critical frequency. (b) DC conductivity plotted versus

SWCNT concentration (percolation curve) with the same data plotted in log-log scales (inset) for determination of percolation threshold. Modified from **Publication II**.

Impedance spectra demonstrate an evident general increase in the conductivity of nanocomposite with nanotube concentration. Meanwhile, two conductivity regimes can be identified in the frequency dependencies of conductivity: frequency-independent in the low-frequency region, and frequency-dependent in the high-frequency one, which correlates with the other reported impedance results for nanocomposites [172,173]. Frequency-independent region indicates ohmic impedance response meaning the nanotube-based conductive network is formed within TPU. Nevertheless, the 0.005 wt%-concentrated nanocomposite does not demonstrate such a regime and essentially behaves identically to the pure TPU sample. A steady increase in conductivity with frequency reflects a dielectric response to perturbing electromagnetic fields:

$$\sigma = \varepsilon_0 \varepsilon'' \omega, \quad (40)$$

where $\varepsilon_0 \cong 8.85 \text{ F/m}$ is vacuum permittivity, ε'' is imaginary dielectric permittivity and ω is the frequency of the applied field. This behavior is supported by the slope ~ 1.0 of the impedance curves.

The transition between two conductivity regions for higher-concentrated nanocomposites occurs at a critical (characteristic) frequency ω_{cr} (indicated in **Figure 19a**). Below the transition, an impedance response is determined by the nanotube network. Thus, the percolation threshold can be assumed in the 0.005 – 0.010 wt% concentration range. Meanwhile, charge carriers travel distances proportional to perturbing wavelength. Therefore, with frequency increase, these distances will decrease, reaching a critical value

equal to an average inter-nanotube distance. Thus, at higher distances, impedance is governed by capacitive contribution and determined by insulating polymer wrapping nanotubes. This explains the shift in ω_{cr} towards higher frequencies with SWCNT concentration increase.

Taken at the lowest frequency (1 Hz) applied, DC conductivity plotted versus SWCNT concentration represents a typical percolation curve (**Figure 19b**) described by equation (13). Since impedance spectra pointed to the percolation threshold to be within the 0.005 – 0.010 wt% range, iterative selection of the percolation threshold φ_c in this range resulted in the best fitting at 0.006 wt% (inset in **Figure 19b**). Thus, an ultralow percolation threshold of 0.006 wt% (equivalent to 0.0037 vol%) was found which is orders of magnitude lower than the ones found for TPU-based nanocomposites prepared by CP [99] and is comparable to the lowest percolation thresholds reported (typically, for epoxy-based nanocomposites [88,91]). Moreover, according to equation (14) derived from percolation theory, for an aspect ratio approximately equal to 3000 of nanotubes used, φ_c should be ~ 0.035 wt% (assuming SWCNT density as 1.9 g/cm^3). Considerably lower values found in conductivity measurements could be explained by the balance between high dispersion degree and, at the same time, moderate agglomeration between nanotubes. Such a phenomenon could be explained by the formation of small-scale chain-like agglomerates, which would allow the formation of percolative conductive pathways at the lower nanotube concentration compared to the case of uniformly distributed particles [16]. Indeed, a moderate degree of aggregation was shown to lead to lower values of percolation threshold by both experimental [174] and simulation [175] studies. In some works, such a

phenomenon is referred to as a kinetic percolation threshold due to filler movement and re-aggregation [93].

Besides, the slope of the fitting line t (power value in equation (14)) could also provide some useful information on SWCNT network construction. Fitting results yield $t = 1.16 \pm 0.16$, which is lower than the 2.0 predicted for 3D SWCNT network conductivity governed by contact resistance. Decreased t values may be an indication of a certain degree of aggregation between nanotubes. However, analysis of the parameter t is established as quite ambiguous and depends on many factors [88]. In addition, quite low conductivity values should be noted, which is likely attributed to the dominance of tunneling resistance contribution caused by the high wetting of nanotubes by polyurethane.

Nevertheless, the ultralow percolation threshold indicates a “golden middle” in the selection of the aspect ratio of nanotubes and dispersion techniques. On the one hand, the use of quite moderate-length nanotubes (with an aspect ratio of ~ 3000) allows a high dispersion degree. On the other hand, nanotubes of this length construct percolative pathways at lower concentrations because of both, higher exclusive volume (in terms of percolation theory) and not very vigorous dispersion techniques, which could allow a flocculation (moderate agglomeration) of nanotubes.

For estimation of the applicability of nanocomposites in soft electronics, in addition to electrical properties, mechanical properties should be evaluated too. Since this work touches on the conductivity topic, the results are given in short (detailed description of the results of tensile tests are presented in **Publication II**). Briefly, typical for nanocomposites, an increase in elasticity (Young’s modulus) and a decrease in the strain at break with

SWCNT concentration were observed. These two trends lead to a maximum in tensile strength at 0.1 – 0.2 wt% concentration. Nevertheless, strain at break is generally maintained before 0.25 wt% (before significant agglomeration happened at the highest concentration as was found in SEM analysis (**Figure 18d**)) indicating that low-concentrated nanocomposites are of practical interest. Moreover, an increase in Young's modulus related to the nanotube amount added (from ~ 15 MPa to 30 MPa for 0.25 wt% concentration) appeared to be comparable or even superior to the results for CNT/polyurethane composites [99,125,126,176].

Simultaneous measurements of the mechanical sensitivity (piezoresistive response) of nanocomposites yielded highly promising results as well. **Figure 20a** depicts stress-strain and corresponding $\Delta R/R_0$ -strain curves in moderate strain range (250%), while **Figure 20b** depicts the piezoresistive response in the whole strain range.

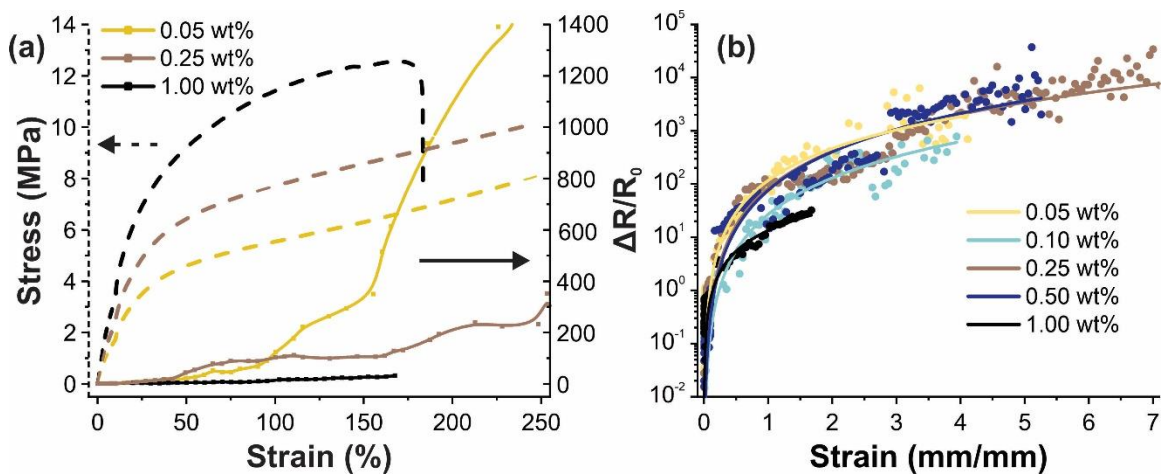


Figure 20. (a) Piezoresistive ($\Delta R/R_0$) response to strain (right y-axis) plotted with stress-strain curves (left y-axis) for SWCNT/TPU nanocomposites at 0.05, 0.25, and 1.00 wt% and (b) the same dependency plotted in the whole strain range. Modified from **Publication II**.

Piezoresistive tests indicate a decrease in mechanical sensitivity with a nanotube concentration increase, which is in good agreement with established mechanisms of composite strain sensing assuming the highest response at near-percolation threshold concentrations based on losses of contact junctions and an exponential increase in tunneling resistance (discussed in details in Section 2.3.1). Gauge factor (GF) values were calculated according to equation (15) in the elastic range (since this deformation region allows multiple uses of materials and is of practical interest; both are given in **Figure 20** and **Table 4**). Within the whole strain range, maximum GFs may be found (**Figure 20b**, **Table 4**). The results point to the highest sensitivity for medium-concentrated nanocomposites. On the one hand, it is associated with fast achievement of immeasurable resistances of $G\Omega$ s for low-concentrated nanocomposites (which do not change at the following strain). On the other hand, the brittleness of high-concentrated nanocomposites does not allow them to stretch sufficiently to reach breaks on the nanotube network.

Nevertheless, GF in the elastic region should be considered a figure of merit. The very high GF value of 82 achieved at such a low nanotube concentration of 0.05 wt% opens up extremely beneficial sides of nanocomposites proposed in this work: high performance at low concentrations. This result is reached because of the ultralow percolation threshold. As a next step, for investigation of sensor repeatability and aging stability, cycling tests could be performed, which would demonstrate the applicability of such sensors in real devices. Nevertheless, the goal of this work was to investigate fundamental possibilities for various applications, such as piezoresistivity (strain sensing) and EMI-shielding.

Table 4. Elastic range and GF values determined for both elastic and the whole (maximum GF) strain ranges.

SWCNT concentration (wt%)	Elastic range (%)	GF in the elastic range	Maximum GF
TPU	26	-	-
0.05	18	82 ± 2	480 ± 20
0.10	21	35 ± 2	150 ± 10
0.25	24	22 ± 9	1090 ± 30
0.50	21	15 ± 8	780 ± 30
1.00	22	8.0 ± 0.4	15.5 ± 1.8

This paradigm was achieved for EMI shielding efficiency in the THz range too. **Figure 21a** represents transmittance spectra of SWCNT/TPU nanocomposites in the THz range and **Figure 21b** shows the resulting dependency of shielding efficiency normalized to the sample thickness dependency on SWCNT concentration at different probe frequencies. A steady drop in transmittance observed for all the nanocomposites corresponds to a typical for nanotube networks electrodynamic response explained within the framework of the Drude conductivity model (applicable for metals).

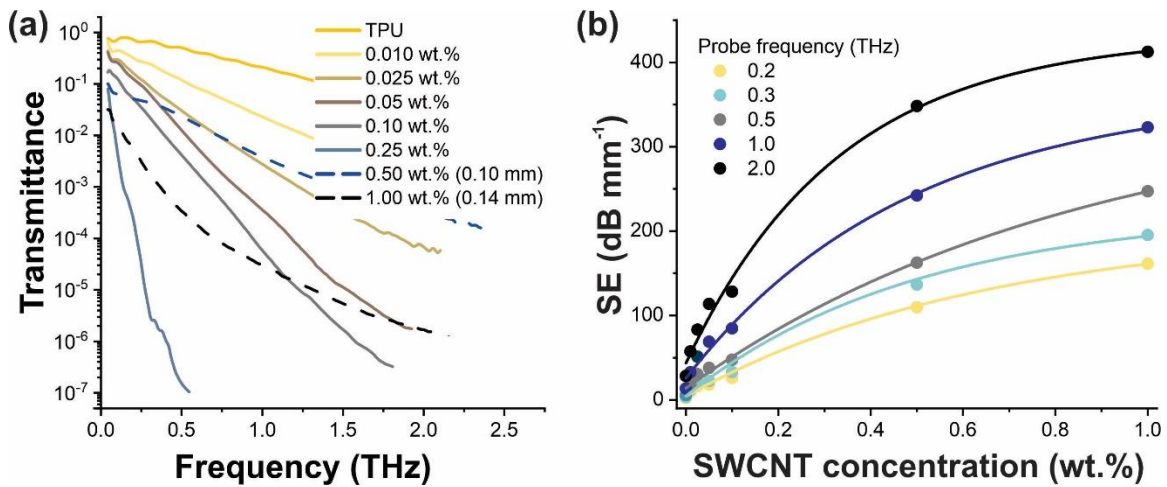


Figure 21. (a) Transmittance spectra of SWCNT/TPU nanocomposites with 0.5-mm thickness (unless otherwise indicated) in THz range at different SWCNT concentrations; (b) Normalized SE dependency on SWCNT concentration at different probe frequencies. Modified from **Publication II**.

SWCNT/TPU nanocomposites exhibit extremely high shielding efficiency normalized to the sample thickness (calculated according to equation (28)), obviously growing with nanotube concentration. In particular, SE of 20 dB/mm at 1 THz frequency is achieved for a very low concentration of 0.01 wt%, which supports the paradigm of high performance at low concentrations and originates from a low percolation threshold.

The percolation threshold as well as strain sensing and EMI shielding efficiency performance of SWCNT/TPU nanocomposites can be compared with the other reported results in these areas. **Table 5** represents the lowest percolation threshold values found for the CNT/TPU elastic nanocomposites with different types of CNTs produced by different fabrication techniques. Comparison with the recent works reveals at least one order of magnitude drop in the percolation threshold values achieved in this study, which verifies the proposed approach.

Table 5. Percolation threshold values achieved in the papers related to CNT/TPU nanocomposites (sorted by the publication year).

Filler type	Aspect ratio	Processing	Percolation threshold (wt%)	Ref
MWCNT	~100	Solution mixing	0.28	[177]
MWCNT	~160	Melt mixing	0.13	[178]
MWCNT	~160	Solution mixing	0.35	[179]
carbon nanostructure (CNS)	70 μm length; 20 μm thickness	Melt mixing	0.06	[180]
MWCNT	~160	Melt mixing	3.02	[125]
MWCNT	~160	Fused filament fabrication + 3D printing	2 - 3	[181]
MWCNT	$\sim 10^3$	CP (NIPS)	1.5	[99]
MWCNT	$\sim 10^4$	CP (NIPS)	0.7	[99]
SWCNT	$10^5 - 10^6$	CP (NIPS)	0.4	[99]
SWCNT	$\sim 10^3$	CP (NIPS)	0.006	this work

Thus, a new strategy for the fabrication of elastic SWCNT/thermoplastic nanocomposites has resulted in the unprecedentedly low percolation threshold and state-of-the-art values of both GF and SE in the THz range in terms of performance achieved at low concentrations (**Figure 22**). These remarkable results are attributed to the appropriate selection of SWCNT aspect ratio and nanocomposite manufacturing route (SWCNT dispersion and nanocomposite formation) yielding a close-to-homogeneous spatial distribution of nanotubes, which allows the formation of percolating pathways at ultralow concentrations, and provide great prospects for nanocomposite industry development.

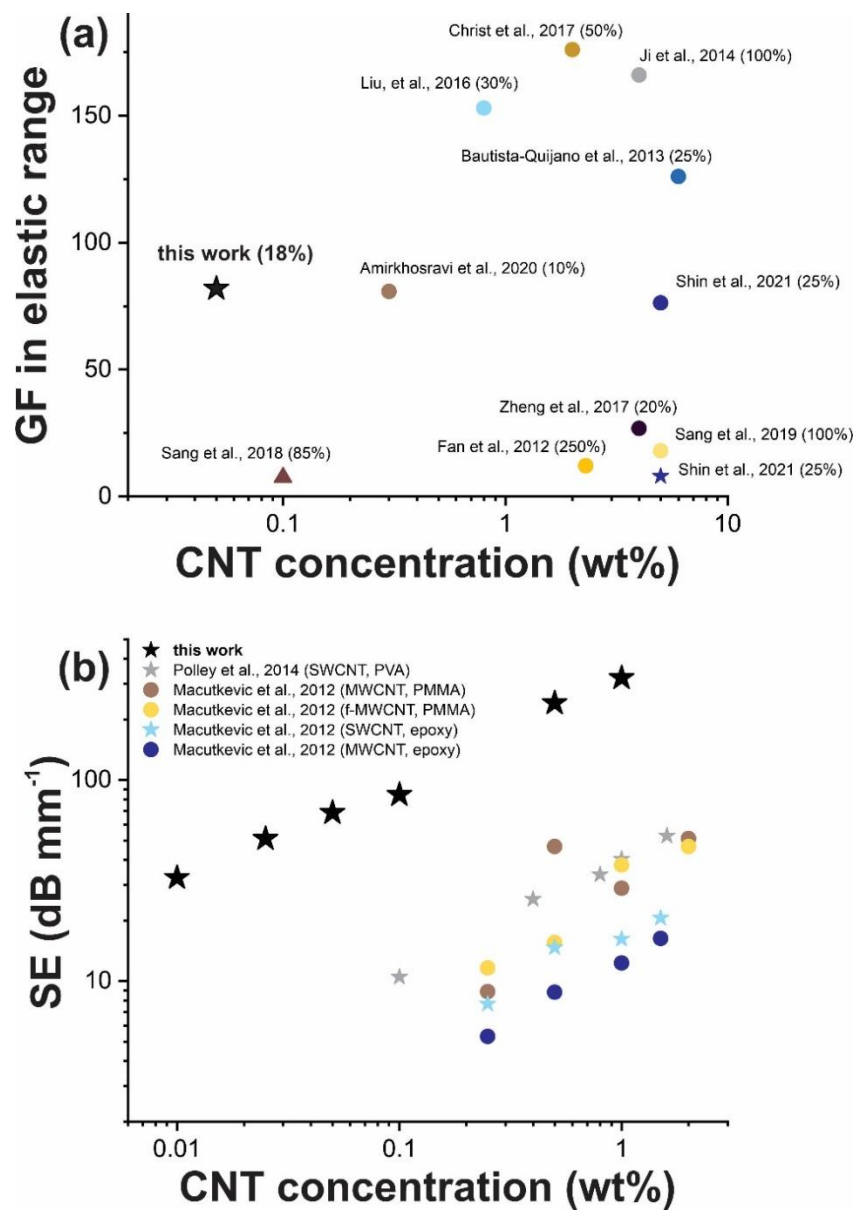


Figure 22. (a) The advances in the GF values plotted versus CNT concentration (strain is indicated in the brackets); ★ correspond to SWCNTs, ● to MWCNTs, ▲ to carbon nanostructures based on MWCNTs. (b) The advances in the normalized SE values at 1 THz (CNT type and polymer are indicated in the brackets). Modified from **Publication II**.

5.2. Nanotube bulk density optimization for SWCNT/thermoset nanocomposites

As was discussed above, nanotube dispersion is the primary problem in CNT/polymer nanocomposite manufacturing. Commercial masterbatches (MBs) are one of the most convenient solutions to this problem for industry. Highly concentrated pastes with pre-dispersed nanotubes can be easily incorporated into the manufacturing process and do not require specific equipment necessary for CNT powder processing. Densely packed in polymer, CNTs cannot be aerosolized, which significantly lowers health risks. Nevertheless, MBs possess certain drawbacks: specificity to certain polymers, specific storage conditions, and high price compared to raw nanotube powders.

Briquettes, the fabrication procedure of which is described in Section 2.3.2, are an alternative polymer-unspecific solution. Nevertheless, compression of nanotubes could affect their subsequent dispersion in the polymer (for instance, leading to an increased agglomeration/entanglement degree) or introduce defects in SWCNT structure. BET analysis and Raman spectroscopy results indicated no noticeable changes caused by both compression and rapid expansion (RESS) of nanotube powders (**Table 1**). The nanotube agglomeration state in the scale of tens of microns also seems unchanged according to the SEM observations (**Figure 23c-e**). However, the bulk density of the powder varies in orders of magnitude (**Table 1**, powders are captured and illustrated in **Figure 23a-b**).

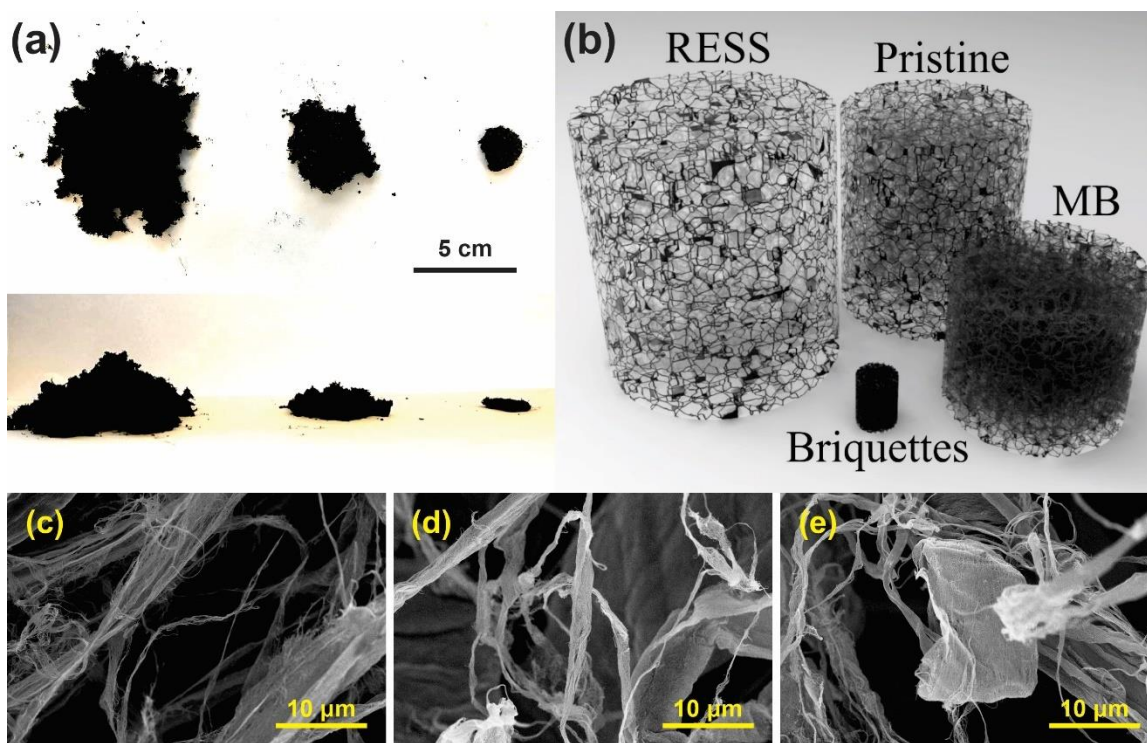


Figure 23. (a) Photos of SWCNT powder types (from left to right: RESS, pristine, briquettes) from the top view (top) and side view (bottom). (b) Schematic representation of differences in bulk densities of nanotubes of different types. SEM images of (c) RESS, (d) pristine, and (e) briquette types of SWCNTs. Taken from **Publication III**.

Thus, except for bulk densities (where briquettes possess evident advantages for practical use), all the other initial parameters of SWCNTs are the same. SEM analysis of SWCNT/epoxy nanocomposites fabricated from these three types of SWCNT powders and MBs (four types total) also did not yield noticeable differences between nanotube morphology (images in **Publication III**). At the lowest concentrations, in all four types of nanocomposites, SWCNTs tend to form small agglomerates of bundles/nanotubes widely and uniformly distributed in the epoxy matrix. Reaching higher concentrations, distances between these agglomerates decrease, while their size, on the contrary, increases. It occurs until the highest concentrations (~ 1.00 wt%), at which all the observed area of the

nanocomposite fracture surface contains an interconnected SWCNT network. Thus, since nanotube morphology governs the resulting properties of nanocomposites, those prepared from nanotube briquettes have prerequisites to perform similarly despite huge variations in the bulk density of raw nanotube material.

Both DC and AC conductivity tests were carried out for nanocomposites. Percolation curves obtained are demonstrated in **Figure 24a** (DC and AC measurements gave identical results (SI in **Publication III**)).

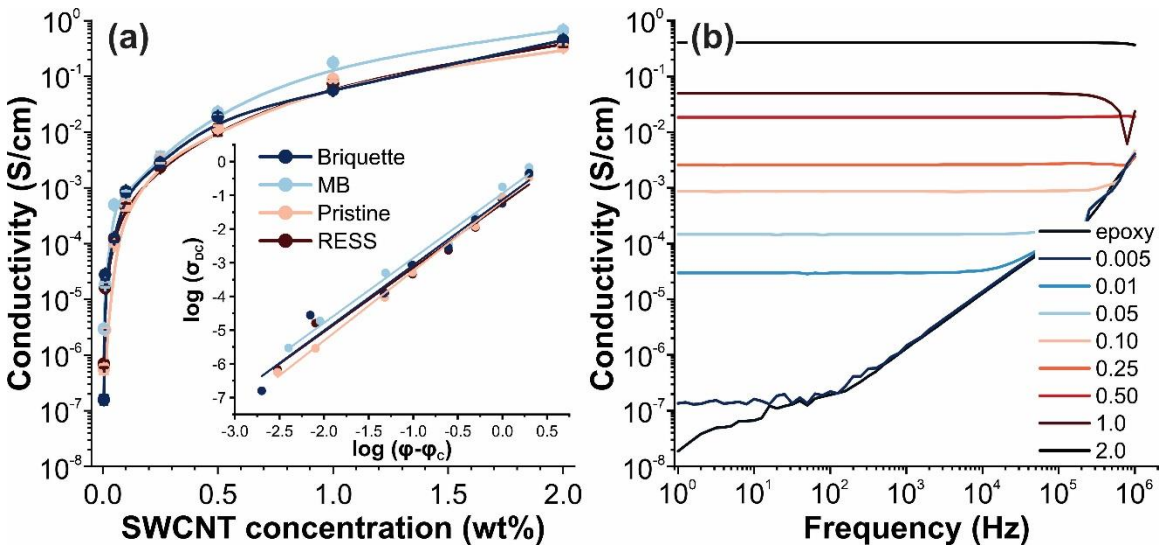


Figure 24. (a) Percolation curves (nanocomposite conductivity dependency on nanotube concentration) obtained for different types of nanocomposites (indicated in legend) and the same data plotted in log-log scales (inset). (b) Impedance spectra of pristine SWCNT/epoxy nanocomposites with different nanotube concentrations. Modified from **Publication III**

Compared to SWCNT/TPU nanocomposites, SWCNT/epoxy ones demonstrate much higher conductivity (reaching 10⁻¹ S/cm for 1.0 wt%). It could be explained by the absence of polymer wettability observed for TPU, which is also supported by SEM (**Publication III**). **Table 6** contains the results of percolation threshold determination and exponential parameter t (from equation (13)).

Table 6. Percolation thresholds and scaling parameter t found for different types of SWCNT/epoxy nanocomposites.

Series	φ_c (wt%)	t
Briquettes	0.003	1.94 ± 0.14
MB	0.001	1.92 ± 0.09
Pristine	0.002	2.07 ± 0.04
RESS	0.002	1.90 ± 0.10

All the nanocomposites have ultralow percolation thresholds, meanwhile, the deviations between different types are insignificant. Such low values should be attributed to manufacturing technique and moderate SWCNT aspect ratio (as was discussed for SWCNT/TPU nanocomposites). Nevertheless, in contrast to the TPU-based ones, the scaling parameter t of SWCNT/epoxy nanocomposite appeared to be noticeably higher (approximately 2.0) which is in excellent correlation with percolation theory [88].

To investigate features of nanocomposite conductivity behavior, impedance spectroscopy (as it was done for TPU nanocomposites, **Figure 24b**) was utilized. Curiously, impedance response turned out to be different compared to polyurethane-based samples. In this case, a pronounced frequency-independent region is observed for all the SWCNT concentrations, including the lowest 0.005 wt% (obviously, except pure polymer), meaning percolation thresholds to be lower than 0.005 wt%, this way verifying the results obtained from DC conductivity analysis. Moreover, above 0.25 wt%, within the 1 Hz – 1 MHz frequency range studied, no frequency-dependent regions can be revealed at all. This implies that the average inter-tube distance corresponding to the characteristic (critical) frequency is not achieved indicating a higher SWCNT dispersion degree than it was achieved for TPU nanocomposites. This assumption is supported by lower percolation

thresholds too. Nonetheless, at the same time, as the nanotubes used were the same as for the TPU nanocomposites (commercial SWCNTs with ~ 3000 aspect ratio), they are considerably lower than the theoretically predicted value, which also might indicate a moderate formation of small-scale chain-like aggregates resulting in a formation of percolative network at very low concentrations.

Thus, SWCNT/epoxy nanocomposites demonstrate remarkable electrical conductivity properties with both ultralow percolation thresholds (0.001 – 0.003 wt%) and, unlike TPU/SWCNT nanocomposites, high conductivity ($\sim 10^{-1}$ S/cm for 1.0 wt%). Meanwhile, densely packed SWCNT briquettes used as an initial material resulted in similarly high conductivity as the other samples, including ones based on commercial MBs.

In addition to electrical conductivity tests, the nanocomposites were tested on thermal conductivity and stability. These parameters appeared to be similar too (details are in **Publication III**), which supports the identity of the nanocomposites fabricated from SWCNT powders with different bulk densities (consolidation degrees). This is caused by similar nanotube morphology in polymer, which is likely to come from similar properties of raw powders (defectiveness, surface area, morphology). The compression procedure, which increases bulk density by more than 20 times, probably affects macroscale nanotube organization, while the microscale one (determining the properties) is left unchanged.

Thus, an approach to use briquette-packed SWCNT powders proposed in this work provides a highly promising solution for the nanocomposite industry since they are significantly simpler for processing compared to pristine powders, but noticeably cheaper and not as polymer-specific as MBs. These advantages are illustrated in **Figure 25**.

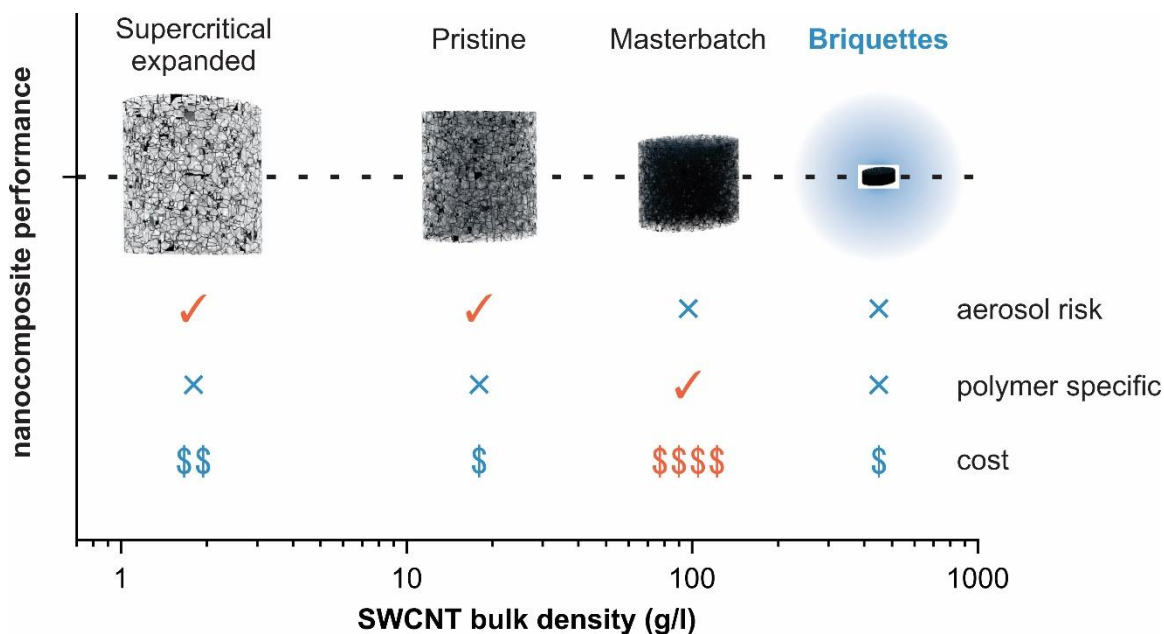


Figure 25. Schematic illustration of briquette-packed SWCNT powders providing identical nanocomposite performance than the other types of raw SWCNT material but, because of much higher bulk density, being advantageous over the rest ones. Modified from **Publication III**

Chapter 6. Conclusions

The current thesis addresses the problems of controllable assembling of SWCNT networks in macromaterials for their subsequent employment in electronic and optical applications. Meanwhile, two branches of the study were formulated. The first one concerns the controlled synthesis of quasi-2D nanotube networks – thin SWCNT films, which main application is transparent conductive films. The second direction is devoted to the problems of SWCNT organization in a 3D network in host polymer – nanocomposite formation, which conductivity properties were realized in such applications as mechanical sensing (piezoresistivity) and shielding from electromagnetic fields. New strategies in chemical engineering of the CO-based aerosol CVD reactor were fulfilled to optimize the synthesis of SWCNT thin films (macroscale “2D” network): improve the figure of merits of the product (film conductivity, or, R_{90}) and the process (synthesis productivity, or, yield), while alternative methods for the fabrication of SWCNT/polymer nanocomposites were studied and developed for the achievement of decreased percolation threshold for electronic applications:

- the performance of SWCNT films as TCFs was enhanced by residence time tuning leading to the controllable adjustment of SWCNT length: R_{90} of $51 \Omega/\square$ was achieved for doped SWCNT films; moreover, this method allowed the separation of the catalyst activation and nanotube growth stages, which brings opportunities for the study of SWCNT growth kinetics in aerosol CVD process (**Publication I, Publication IV, Publication V**);

- a new fast approach to SWCNT growth kinetics evaluation based on analysis of R_{90} versus residence time trends was proposed: the direct correlation between R_{90} (conductivity) evolution with residence time and nanotube growth was shown; opening up the prospects for solving one of the key problems of aerosol CVD reactors – reactor scaling.
- synthesis productivity (yield) was significantly improved by the introduction of H_2 in the CO-based process: a 15-fold increase in the yield was found (the highest compared to that achieved by using other promoters), which leads to noticeably improved R_{90} /yield balance – the crucial parameter for industrial production of TCF.
- a new method based on the combination of coagulation precipitation technique and moderate aspect ratio of SWCNTs was proposed for the assembling 3D SWCNT networks within polymer at very low concentrations – nanocomposites with ultralow percolation thresholds: 0.006 wt% for elastic SWCNT/TPU nanocomposites was achieved as a result leading to the state-of-the-art performance of low-concentrated nanocomposites in soft electronic applications: strain sensing (gauge factor of 82 for 0.05 wt% SWCNT concentration) and EMI shielding in THz range (20 dB/mm for 0.01 wt%) (**Publication II**);
- fabrication of SWCNT/polymer nanocomposites was significantly simplified by the use of compressed (briquette-shaped) SWCNT powders (by 25 times): the same functional properties of nanocomposites as those of nanocomposites fabricated

from highly aerosolized powders and expensive and polymer-specific masterbatches were found (**Publication III**).

Bibliography

- [1] Radushkevich LV, Lukyanovich VM, O strukture ugleroda, obrazujucesja pri termiceskom razlozenii okisi ugleroda na zeleznom kontakte, *Zurn Fisic Chim* 26 (1952) 88–95.
- [2] A. Oberlin, M. Endo, T. Koyama, Filamentous growth of carbon through benzene decomposition, *J Cryst Grpwth.* 32 (1976) 335-349. [https://doi.org/10.1016/0022-0248\(76\)90115-9](https://doi.org/10.1016/0022-0248(76)90115-9).
- [3] S. Iijima, Helical microtubules of graphite carbon, *Nature.* 354 (1991) 56-58. <http://dx.doi.org/10.1038/354056a0>.
- [4] H. Chen, A. Roy, J.B. Baek, L. Zhu, J. Qu, L. Dai, Controlled growth and modification of vertically-aligned carbon nanotubes for multifunctional applications, *Materials Science and Engineering R: Reports.* 70 (2010) 63–91. <https://doi.org/10.1016/j.mser.2010.06.003>.
- [5] E. Theocharous, C.J. Chunnillall, R. Mole, D. Gibbs, N. Fox, N. Shang, G. Howlett, B. Jensen, R. Taylor, J.R. Reveles, O.B. Harris, N. Ahmed, The partial space qualification of a vertically aligned carbon nanotube coating on aluminium substrates for EO applications, *Opt Express.* 22 (2014) 7290. <https://doi.org/10.1364/oe.22.007290>.
- [6] E.T. Thostenson, W.Z. Li, D.Z. Wang, Z.F. Ren, T.W. Chou, Carbon nanotube/carbon fiber hybrid multiscale composites, *J Appl Phys.* 91 (2002) 6034–6037. <https://doi.org/10.1063/1.1466880>.
- [7] N. Behabtu, C.C. Young, D.E. Tsentalovich, O. Kleinerman, X. Wang, A.W.K. Ma, E. Amram Bengio, R.F. Ter Waarbeek, J.J. De Jong, R.E. Hoogerwerf, S.B. Fairchild, J.B. Ferguson, B. Maruyama, J. Kono, Y. Talmon, Y. Cohen, M.J. Otto, M. Pasquali, Strong, Light, Multifunctional Fibers of Carbon Nanotubes with Ultrahigh Conductivity, *Science.* 339 (2013) 182-186. <https://doi.org/10.1126/science.1228061>.
- [8] W. Yang, P. Thordarson, J.J. Gooding, S.P. Ringer, F. Braet, Carbon nanotubes for biological and biomedical applications, *Nanotechnology.* 18 (2007) 412001. <https://doi.org/10.1088/0957-4484/18/41/412001>.
- [9] E.A. Laird, F. Kuemmeth, G.A. Steele, K. Grove-Rasmussen, J. Nygård, K. Flensberg, L.P. Kouwenhoven, Quantum transport in carbon nanotubes, *Rev Mod Phys.* 87 (2015) 703-764. <https://doi.org/10.1103/RevModPhys.87.703>.
- [10] A. K. Geim, K.S. Novoselov, The rise of graphene. *Nature Mater.* 6 (2007) 183-191. <https://doi.org/10.1038/nmat1849>.
- [11] M.S. Dresselhaus, G. Dresselhaus, R. Saito, Physics of carbon nanotubes. 33 (1995) 883-891. [https://doi.org/10.1016/0008-6223\(95\)00017-8](https://doi.org/10.1016/0008-6223(95)00017-8).
- [12] J.W. Mintmire, C.T. White, Electronic and structural properties of carbon nanotubes, *Carbon Nanotubes.* (1996) 37–46. <https://doi.org/10.1016/b978-0-08-042682-2.50010-22>.
- [13] J. Wilder, L. Venema, A. Rinzler, R.E. Smalley, C. Dekker. Electronic structure of atomically resolved carbon nanotubes. *Nature* 391 (1998) 59–62. <https://doi.org/10.1038/34139>.

- [14] R. Saito, M. Fujita, G. Dresselhaus, M.S. Dresselhaus, Electronic structure of chiral graphene tubules, *Appl Phys Lett.* 60 (1992) 2204–2206. <https://doi.org/10.1063/1.107080>.
- [15] H. Kataura, Y. Kumazawa, Y. Maniwa, I. Umezū, S. Suzuki, Y. Ohtsuka, Y. Achiba, Optical Properties of Single-Wall Carbon Nanotubes. *Synth Metals* 103 (1999) 2555-2558. [https://doi.org/10.1016/S0379-6779\(98\)00278-1](https://doi.org/10.1016/S0379-6779(98)00278-1).
- [16] Alamusi, N. Hu, H. Fukunaga, S. Atobe, Y. Liu, J. Li, Piezoresistive strain sensors made from carbon nanotubes based polymer nanocomposites, *Sensors.* 11 (2011) 10691–10723. <https://doi.org/10.3390/s111110691>.
- [17] J.G. Simmons, Generalized Formula for the Electric Tunnel Effect between Similar Electrodes Separated by a Thin Insulating Film, *J Appl Phys.* 34 (1963) 1793–1803. <https://doi.org/10.1063/1.1702682>.
- [18] W. Obitayo, T. Liu, A review: Carbon nanotube-based piezoresistive strain sensors, *J Sens.* 2012 (2012). <https://doi.org/10.1155/2012/652438>.
- [19] F. Du, J.E. Fischer, K.I. Winey, Effect of nanotube alignment on percolation conductivity in carbon nanotube/polymer composites, *Phys Rev B Condens Matter Mater Phys.* 72 (2005) 121404. <https://doi.org/10.1103/PhysRevB.72.121404>.
- [20] F. Yang, M. Wang, D. Zhang, J. Yang, M. Zheng, Y. Li, Chirality Pure Carbon Nanotubes: Growth, Sorting, and Characterization, *Chem Rev.* 120 (2020) 2693–2758. <https://doi.org/10.1021/acs.chemrev.9b00835>.
- [21] S.M. Bachilo, M.S. Strano, C. Kittrell, R.H. Hauge, R.E. Smalley, R. Bruce Weisman, Structure-Assigned Optical Spectra of Single-Walled Carbon Nanotubes, *Science.* 298 (2002) 2361-2366. <https://doi.org/10.1126/science.1078727>.
- [22] F. Ding, A.R. Harutyunyan, B.I. Yakobson, Dislocation theory of chirality-controlled nanotube growth, *Proc Natl Acad Sci USA.* 106 (2009) 2506–2509. <https://doi.org/10.1073/pnas.0811946106>.
- [23] L. Yu, C. Shearer, J. Shapter, Recent Development of Carbon Nanotube Transparent Conductive Films, *Chem Rev.* 116 (2016) 13413–13453. <https://doi.org/10.1021/acs.chemrev.6b00179>.
- [24] H. Geng, K. Kang Kim, K. Lee, G. Yong Kim, H. Kyu Choi, D. Sik Lee, K.A. Hyeok, Y. Hee Lee, Y. Chang, Y. Sil Lee, B. Kim, Y. Jun Lee, Dependence of material quality on performance of flexible transparent conducting films with single-walled carbon nanotubes, *Nano.* 2 (2007) 157-167. <https://doi.org/10.1142/S1793292007000532>.
- [25] M.S. Fuhrer, J. Nygård, L. Shih, M. Forero, Young-Gui Yoon, M.S.C. Mazzoni, Hyung Joon Choi, Jisoon Ihm, Steven G. Louie, A. Zettl, and Paul L. McEuen. Crossed Nanotube Junctions, *Science.* 288 (2000) 494-497. <https://doi.org/10.1126/science.288.5465.494>.
- [26] M.A. Topinka, M.W. Rowell, D. Goldhaber-Gordon, M.D. McGehee, D.S. Hecht, G. Gruner, Charge transport in interpenetrating networks of semiconducting and metallic carbon nanotubes, *Nano Lett.* 9 (2009) 1866–1871. <https://doi.org/10.1021/nl803849e>.

- [27] K. Yanagi, H. Udoguchi, S. Sagitani, Y. Oshima, T. Takenobu, H. Kataura, T. Ishida, K. Matsuda, Y. Maniwa, Transport mechanisms in metallic and semiconducting single-wall carbon nanotube networks, *ACS Nano*. 4 (2010) 4027–4032. <https://doi.org/10.1021/nn101177n>.
- [28] R.K. Jackson, A. Munro, K. Nebesny, N. Armstrong, S. Graham, Evaluation of transparent carbon nanotube networks of homogeneous electronic type, *ACS Nano*. 4 (2010) 1377–1384. <https://doi.org/10.1021/nn9010076>.
- [29] K.K. Kim, J.J. Bae, H.K. Park, S.M. Kim, H.-Z. Geng, K.A. Park, H.-J. Shin, S.-M. Yoon, A. Benayad, J.-Y. Choi, Y.H. Lee, Fermi level engineering of single-walled carbon nanotubes by AuCl₃ doping., *J Am Chem Soc*. 130 (2008) 12757–12761. <https://doi.org/10.1021/ja8038689>.
- [30] A. Znidarsic, A. Kaskela, P. Laiho, M. Gaberscek, Y. Ohno, A.G. Nasibulin, E.I. Kauppinen, A. Hassanien, Spatially resolved transport properties of pristine and doped single-walled carbon nanotube networks, *Journal of Physical Chemistry C*. 117 (2013) 13324–13330. <https://doi.org/10.1021/jp403983y>.
- [31] D. Hecht, L. Hu, G. Grüner, Conductivity scaling with bundle length and diameter in single walled carbon nanotube networks, *Appl Phys Lett*. 89 (2006) 1–4. <https://doi.org/10.1063/1.2356999>.
- [32] E.M. Khabushev, D.V. Krasnikov, J.V. Kolodiaznaia, A.V. Bubis, A.G. Nasibulin, Structure-dependent performance of single-walled carbon nanotube films in transparent and conductive applications, *Carbon*. 161 (2020) 712–717. <https://doi.org/10.1016/j.carbon.2020.01.068>.
- [33] A.G. Nasibulin, A. Ollikainen, A.S. Anisimov, D.P. Brown, P.V. Pikhitsa, S. Holopainen, J.S. Penttilä, P. Heliöstö, J. Ruokolainen, M. Choi, E.I. Kauppinen, Integration of single-walled carbon nanotubes into polymer films by thermo-compression, *Chemical Engineering Journal*. 136 (2008) 409–413. <https://doi.org/10.1016/j.cej.2007.04.033>.
- [34] G.A. Ermolaev, A.P. Tsapenko, V.S. Volkov, A.S. Anisimov, Y.G. Gladush, A.G. Nasibulin, Express determination of thickness and dielectric function of single-walled carbon nanotube films, *Appl Phys Lett*. 116 (2020). <https://doi.org/10.1063/5.0012933>.
- [35] L. Zhao, S. Yu, J. Li, M. Wu, L. Li, X. Wang, Highly reliable flexible transparent conductors prepared with Cu/Ni grid by vacuum-free solution process, *Opt Mater (Amst)*. 120 (2021) 111427. <https://doi.org/10.1016/j.optmat.2021.111427>.
- [36] W. He, C. Ye, Flexible Transparent Conductive Films on the Basis of Ag Nanowires: Design and Applications: A Review, *J Mater Sci Technol*. 31 (2015) 581–588. <https://doi.org/10.1016/j.jmst.2014.11.020>.
- [37] P.C. Wang, L.H. Liu, D. Alemu Mengistie, K.H. Li, B.J. Wen, T.S. Liu, C.W. Chu, Transparent electrodes based on conducting polymers for display applications, *Displays*. 34 (2013) 301–314. <https://doi.org/10.1016/j.displa.2013.05.003>.
- [38] D.J. Lipomi, J.A. Lee, M. Vosgueritchian, B.C.K. Tee, J.A. Bolander, Z. Bao, Electronic properties of transparent conductive films of PEDOT:PSS on

- stretchable substrates, *Chemistry of Materials*. 24 (2012) 373–382.
<https://doi.org/10.1021/cm203216m>.
- [39] C. Bulumulla, R. Gunawardhana, P.L. Gamage, J.T. Miller, R.N. Kularatne, M.C. Biewer, M.C. Stefan, Pyrrole-Containing Semiconducting Materials: Synthesis and Applications in Organic Photovoltaics and Organic Field-Effect Transistors, *ACS Appl Mater Interfaces*. 12 (2020) 32209–32232.
<https://doi.org/10.1021/acsami.0c07161>.
- [40] W. Greenbank, L. Hirsch, G. Wantz, S. Chambon, Interfacial thermal degradation in inverted organic solar cells, *Appl Phys Lett*. 107 (2015) 263301.
<https://doi.org/10.1063/1.4938554>.
- [41] M. Trchová, I. Šeděnková, Z. Morávková, J. Stejskal, Conducting polymer and ionic liquid: Improved thermal stability of the material - A spectroscopic study, *Polym Degrad Stab*. 109 (2014) 27–32.
<https://doi.org/10.1016/j.polymdegradstab.2014.06.012>.
- [42] Q. Zheng, Z. Li, J. Yang, J.K. Kim, Graphene oxide-based transparent conductive films, *Prog Mater Sci*. 64 (2014) 200–247.
<https://doi.org/10.1016/j.pmatsci.2014.03.004>.
- [43] X. Li, Y. Zhu, W. Cai, M. Borysiak, B. Han, D. Chen, R.D. Piner, L. Colomba, R.S. Ruoff, Transfer of large-area graphene films for high-performance transparent conductive electrodes, *Nano Lett*. 9 (2009) 4359–4363.
<https://doi.org/10.1021/nl902623y>.
- [44] D.A. Ilatovskii, E.P. Gilshtein, O.E. Glukhova, A.G. Nasibulin, Transparent Conducting Films Based on Carbon Nanotubes: Rational Design toward the Theoretical Limit, *Advanced Science*. 9 (2022) 2201673.
<https://doi.org/10.1002/advs.202201673>.
- [45] D.W. Shin, J.H. Lee, Y.H. Kim, S.M. Yu, S.Y. Park, J.B. Yoo, A role of HNO₃ on transparent conducting film with single-walled carbon nanotubes, *Nanotechnology*. 20 (2009) 475703. <https://doi.org/10.1088/0957-4484/20/47/475703>.
- [46] A.P. Tsapenko, A.E. Goldt, E. Shulga, Z.I. Popov, K.I. Maslakov, A.S. Anisimov, P.B. Sorokin, A.G. Nasibulin, Highly conductive and transparent films of HAuCl₄-doped single-walled carbon nanotubes for flexible applications, *Carbon*. 130 (2018) 448–457. <https://doi.org/10.1016/j.carbon.2018.01.016>.
- [47] O.T. Zaremba, A.E. Goldt, E.M. Khabushev, A.S. Anisimov, A.G. Nasibulin, Highly efficient doping of carbon nanotube films with chloroauric acid by dip-coating, *Mater Sci Eng B Solid State Mater Adv Technol*. 278 (2022) 115648.
<https://doi.org/10.1016/j.mseb.2022.115648>.
- [48] A.E. Goldt, O.T. Zaremba, M.O. Bulavskiy, F.S. Fedorov, K.V. Larionov, A.P. Tsapenko, Z.I. Popov, P. Sorokin, A.S. Anisimov, H. Inani, J. Kotakoski, K. Mustonen, A.G. Nasibulin, Highly efficient bilateral doping of single-walled carbon nanotubes, *J Mater Chem C Mater*. 9 (2021) 4514–4521.
<https://doi.org/10.1039/d0tc05996j>.
- [49] D.S. Kopylova, D.A. Satco, E.M. Khabushev, A.V. Bubis, D.V. Krasnikov, T. Kallio, A.G. Nasibulin, Electrochemical enhancement of optoelectronic

- performance of transparent and conducting single-walled carbon nanotube films, *Carbo*. 167 (2020) 244–248. <https://doi.org/10.1016/j.carbon.2020.05.103>.
- [50] E.M. Khabushev, D.V. Krasnikov, O.T. Zaremba, A.P. Tsapenko, A.E. Goldt, A.G. Nasibulin, Machine Learning for Tailoring Optoelectronic Properties of Single-Walled Carbon Nanotube Films, *Journal of Physical Chemistry Letters*. 10 (2019) 6962–6966. <https://doi.org/10.1021/acs.jpcclett.9b02777>.
- [51] N. Fukaya, D.Y. Kim, S. Kishimoto, S. Noda, Y. Ohno, One-step sub-10 μm patterning of carbon-nanotube thin films for transparent conductor applications, *ACS Nano*. 8 (2014) 3285–3293. <https://doi.org/10.1021/nn4041975>.
- [52] D. Mitin, Y. Berdnikov, A. Vorobyev, A. Mozharov, S. Raudik, O. Koval, V. Neplokh, E. Moiseev, D. Ilatovskii, A.G. Nasibulin, I. Mukhin, Optimization of Optoelectronic Properties of Patterned Single-Walled Carbon Nanotube Films, *ACS Appl Mater Interfaces*. 12 (2020) 55141–55147. <https://doi.org/10.1021/acsami.0c14783>.
- [53] V. Jourdain, C. Bichara, Current understanding of the growth of carbon nanotubes in catalytic chemical vapour deposition, *Carbon*. 58 (2013) 2–39. <https://doi.org/10.1016/j.carbon.2013.02.046>.
- [54] Q. Wen, R. Zhang, W. Qian, Y. Wang, P. Tan, J. Nie, F. Wei, Growing 20 cm long DWNTs/TWNTs at a rapid growth rate of 80–90 $\mu\text{m/s}$, *Chemistry of Materials*. 22 (2010) 1294–1296. <https://doi.org/10.1021/cm903866z>.
- [55] H.M. Cheng, F. Li, G. Su, H.Y. Pan, L.L. He, X. Sun, M.S. Dresselhaus, Large-scale and low-cost synthesis of single-walled carbon nanotubes by the catalytic pyrolysis of hydrocarbons, *Appl Phys Lett*. 72 (1998) 3282–3284. <https://doi.org/10.1063/1.121624>.
- [56] F. Smail, A. Boies, A. Windle, Direct spinning of CNT fibres: Past, present and future scale up, *Carbon*. 152 (2019) 218–232. <https://doi.org/10.1016/j.carbon.2019.05.024>.
- [57] A.G. Nasibulin, A. Moisala, D.P. Brown, H. Jiang, E.I. Kauppinen, A novel aerosol method for single walled carbon nanotube synthesis, *Chem Phys Lett*. 402 (2005) 227–232. <https://doi.org/10.1016/j.cplett.2004.12.040>.
- [58] J.S. Bulmer, A.W.N. Sloan, M. Glerum, J. Carpena-Núñez, R. Waelder, J. Humes, A.M. Boies, M. Pasquali, R. Rao, B. Maruyama, Forecasting carbon nanotube diameter in floating catalyst chemical vapor deposition, *Carbon*. 201 (2023) 719–733. <https://doi.org/10.1016/j.carbon.2022.08.001>.
- [59] L. Weller, F.R. Smail, J.A. Elliott, A.H. Windle, A.M. Boies, S. Hochgreb, Mapping the parameter space for direct-spun carbon nanotube aerogels, *Carbon*. 146 (2019) 789–812. <https://doi.org/10.1016/j.carbon.2019.01.091>.
- [60] W. Tan, J.C. Stallard, F.R. Smail, A.M. Boies, N.A. Fleck, The mechanical and electrical properties of direct-spun carbon nanotube mat-epoxy composites, *Carbon*. 150 (2019) 489–504. <https://doi.org/10.1016/j.carbon.2019.04.118>.
- [61] A. Kaskela, A.G. Nasibulin, M.Y. Timmermans, B. Aitchison, A. Papadimitratos, Y. Tian, Z. Zhu, H. Jiang, D.P. Brown, A. Zakhidov, E.I. Kauppinen, Aerosol-synthesized SWCNT networks with tunable conductivity and transparency by a

- dry transfer technique, *Nano Lett.* 10 (2010) 4349–4355.
<https://doi.org/10.1021/nl101680s>.
- [62] A.G. Nasibulin, A. Kaskela, K. Mustonen, A.S. Anisimov, V. Ruiz, S. Kivistö, S. Rackauskas, M.Y. Timmermans, M. Pudas, B. Aitchison, M. Kauppinen, D.P. Brown, O.G. Okhotnikov, E.I. Kauppinen, Multifunctional free-standing single-walled carbon nanotube films, *ACS Nano*. 5 (2011) 3214–3221.
<https://doi.org/10.1021/nn200338r>.
- [63] A. Moisala, A.G. Nasibulin, D.P. Brown, H. Jiang, L. Khriachtchev, E.I. Kauppinen, Single-walled carbon nanotube synthesis using ferrocene and iron pentacarbonyl in a laminar flow reactor, *Chem Eng Sci.* 61 (2006) 4393–4402.
<https://doi.org/10.1016/j.ces.2006.02.020>.
- [64] A.G. Nasibulin, D.P. Brown, P. Queipo, D. Gonzalez, H. Jiang, E.I. Kauppinen, An essential role of CO₂ and H₂O during single-walled CNT synthesis from carbon monoxide, *Chem Phys Lett.* 417 (2006) 179–184.
<https://doi.org/10.1016/j.cplett.2005.10.022>.
- [65] D.V. Krasnikov, B.Y. Zabelich, V.Y. Iakovlev, A.P. Tsapenko, S.A. Romanov, A.A. Alekseeva, A.K. Grebenko, A.G. Nasibulin, A spark discharge generator for scalable aerosol CVD synthesis of single-walled carbon nanotubes with tailored characteristics, *Chemical Engineering Journal.* 372 (2019) 462–470.
<https://doi.org/10.1016/j.cej.2019.04.173>.
- [66] V.Y. Iakovlev, D.V. Krasnikov, E.M. Khabushev, A.A. Alekseeva, A.K. Grebenko, A.P. Tsapenko, B.Y. Zabelich, J.V. Kolodiaznaia, A.G. Nasibulin, Fine-tuning of spark-discharge aerosol CVD reactor for single-walled carbon nanotube growth: The role of ex situ nucleation, *Chemical Engineering Journal.* 383 (2020) 123073. <https://doi.org/10.1016/j.cej.2019.123073>.
- [67] Y. Tian, M.Y. Timmermans, M. Partanen, A.G. Nasibulin, H. Jiang, Z. Zhu, E.I. Kauppinen, Growth of single-walled carbon nanotubes with controlled diameters and lengths by an aerosol method, *Carbon.* 49 (2011) 4636–4643.
<https://doi.org/10.1016/j.carbon.2011.06.036>.
- [68] Y. Tian, A.G. Nasibulin, B. Aitchison, T. Nikitin, J.V. Pfaler, H. Jiang, Z. Zhu, L. Khriachtchev, D.P. Brown, E.I. Kauppinen, Controlled synthesis of single-walled carbon nanotubes in an aerosol reactor, *Journal of Physical Chemistry C.* 115 (2011) 7309–7318. <https://doi.org/10.1021/jp112291f>.
- [69] E.M. Khabushev, J.V. Kolodiaznaia, D.V. Krasnikov, A.G. Nasibulin, Activation of catalyst particles for single-walled carbon nanotube synthesis, *Chemical Engineering Journal.* 413 (2021) 127475.
<https://doi.org/10.1016/j.cej.2020.127475>.
- [70] I.V. Anoshkin, A.G. Nasibulin, Y. Tian, B. Liu, H. Jiang, E.I. Kauppinen, Hybrid carbon source for single-walled carbon nanotube synthesis by aerosol CVD method, *Carbon.* 78 (2014) 130–136. <https://doi.org/10.1016/j.carbon.2014.06.057>.
- [71] A.R. Bogdanova, D.V. Krasnikov, E.M. Khabushev, J.A. Ramirez B., Y.E. Matyushkin, A.G. Nasibulin, Role of Hydrogen in Ethylene-Based Synthesis of Single-Walled Carbon Nanotubes, *Nanomaterials.* 13 (2023) 1504.
<https://doi.org/10.3390/nano13091504>.

- [72] E.X. Ding, H. Jiang, Q. Zhang, Y. Tian, P. Laiho, A. Hussain, Y. Liao, N. Wei, E.I. Kauppinen, Highly conductive and transparent single-walled carbon nanotube thin films from ethanol by floating catalyst chemical vapor deposition, *Nanoscale*. 9 (2017) 17601–17609. <https://doi.org/10.1039/c7nr05554d>.
- [73] E.X. Ding, A. Hussain, S. Ahmad, Q. Zhang, Y. Liao, H. Jiang, E.I. Kauppinen, High-performance transparent conducting films of long single-walled carbon nanotubes synthesized from toluene alone, *Nano Res.* 13 (2020) 112–120. <https://doi.org/10.1007/s12274-019-2581-7>.
- [74] E.M. Khabushev, D.V. Krasnikov, A.E. Goldt, E.O. Fedorovskaya, A.P. Tsapenko, Q. Zhang, E.I. Kauppinen, T. Kallio, A.G. Nasibulin, Joint effect of ethylene and toluene on carbon nanotube growth, *Carbon*. 189 (2022) 474–483. <https://doi.org/10.1016/j.carbon.2021.12.052>.
- [75] G. Glockler, Carbon-Oxygen Bond Energies and Bond Distances, *The Journal of Physical Chemistry*. 62 (1958) 1049–1054. <https://doi.org/10.1021/j150567a006>.
- [76] K. Mustonen, P. Laiho, A. Kaskela, Z. Zhu, O. Reynaud, N. Houbenov, Y. Tian, T. Susi, H. Jiang, A.G. Nasibulin, E.I. Kauppinen, Gas phase synthesis of non-bundled, small diameter single-walled carbon nanotubes with near-armchair chiralities, *Appl Phys Lett*. 107 (2015) 013106. <https://doi.org/10.1063/1.4926415>.
- [77] Y. Liao, A. Hussain, P. Laiho, Q. Zhang, Y. Tian, N. Wei, E.X. Ding, S.A. Khan, N.N. Nguyen, S. Ahmad, E.I. Kauppinen, Tuning Geometry of SWCNTs by CO₂ in Floating Catalyst CVD for High-Performance Transparent Conductive Films, *Adv Mater Interfaces*. 5 (2018) 1801209. <https://doi.org/10.1002/admi.201801209>.
- [78] Y. Tian, M.Y. Timmermans, S. Kivistö, A.G. Nasibulin, Z. Zhu, H. Jiang, O.G. Okhotnikov, E.I. Kauppinen, Tailoring the diameter of single-walled carbon nanotubes for optical applications, *Nano Res.* 4 (2011) 807–815. <https://doi.org/10.1007/s12274-011-0137-6>.
- [79] A.G. Nasibulin, P. Queipo, S.D. Shandakov, D.P. Brown, H. Jiang, P.V. Pikhitsa, O. V. Tolochko, E.I. Kauppinen, Studies on mechanism of single-walled carbon nanotube formation, *J Nanosci Nanotechnol*. 6 (2006) 1233–1246. <https://doi.org/10.1166/jnn.2006.340>.
- [80] M.B. Bryning, D.E. Milkie, M.F. Islam, L.A. Hough, J.M. Kikkawa, A.G. Yodh, Carbon nanotube aerogels, *Advanced Materials*. 19 (2007) 661–664. <https://doi.org/10.1002/adma.200601748>.
- [81] X. Gui, J. Wei, K. Wang, A. Cao, H. Zhu, Y. Jia, Q. Shu, D. Wu, Carbon nanotube sponges, *Advanced Materials*. 22 (2010) 617–621. <https://doi.org/10.1002/adma.200902986>.
- [82] H. Sun, Z. Xu, C. Gao, Multifunctional, ultra-flyweight, synergistically assembled carbon aerogels, *Advanced Materials*. 25 (2013) 2554–2560. <https://doi.org/10.1002/adma.201204576>.
- [83] F. Schütt, S. Signetti, H. Krüger, S. Röder, D. Smazna, S. Kaps, S.N. Gorb, Y.K. Mishra, N.M. Pugno, R. Adelung, Hierarchical self-entangled carbon nanotube tube networks, *Nat Commun*. 8 (2017) 1215. <https://doi.org/10.1038/s41467-017-01324-7>.

- [84] SWCNT markets with the greatest potential, (n.d.) 10–12. DataM Intelligence, Global Carbon Nanotubes Market. <https://www.datamintelligence.com/research-report/carbon-nanotubesmarket>, 2023.
- [85] B. Arash, Q. Wang, V.K. Varadan, Mechanical properties of carbon nanotube/polymer composites, *Sci Rep.* 4 (2014) 1–8. <https://doi.org/10.1038/srep06479>.
- [86] M.T. Byrne, Y.K. Guin'Ko, Recent advances in research on carbon nanotube - polymer composites, *Advanced Materials.* 22 (2010) 1672–1688. <https://doi.org/10.1002/adma.200901545>.
- [87] P.M. Ajayan, O. Stephan, C. Colliex, D. Trauth, Aligned Carbon Nanotube Arrays Formed by Cutting a Polymer Resin-Nanotube Composite, *Science.* 265 (2006) 11–12. <https://doi.org/10.1126/science.265.5176.1212>.
- [88] W. Bauhofer, J.Z. Kovacs, A review and analysis of electrical percolation in carbon nanotube polymer composites, *Compos Sci Technol.* 69 (2009) 1486–1498. <https://doi.org/10.1016/j.compscitech.2008.06.018>.
- [89] I. Balberg, C.H. Anderson, S. Alexander, N. Wagner, Excluded volume and its relation to the onset of percolation, *Phys Rev B.* 30 (1984) 3933. <https://doi.org/10.1103/PhysRevB.30.3933>.
- [90] A. Celzard, E. McRae, C. Deleuze, M. Dufort, Critical concentration in percolating systems containing a high-aspect-ratio filler, *Phys Rev B Condens Matter Mater Phys.* 53 (1996) 6209–6214. <https://doi.org/10.1103/PhysRevB.53.6209>.
- [91] J.K.W. Sandler, J.E. Kirk, I.A. Kinloch, M.S.P. Shaffer, A.H. Windle, Ultra-low electrical percolation threshold in carbon-nanotube-epoxy composites, *Polymer.* 44 (2003) 5893–5899. [https://doi.org/10.1016/S0032-3861\(03\)00539-1](https://doi.org/10.1016/S0032-3861(03)00539-1).
- [92] A. Moaisala, Q. Li, I.A. Kinloch, A.H. Windle, Thermal and electrical conductivity of single- and multi-walled carbon nanotube-epoxy composites, *Compos Sci Technol.* 66 (2006) 1285–1288. <https://doi.org/10.1016/j.compscitech.2005.10.016>.
- [93] J.Z. Kovacs, B.S. Velagala, K. Schulte, W. Bauhofer, Two percolation thresholds in carbon nanotube epoxy composites, 67 (2007) 922–928. <https://doi.org/10.1016/j.compscitech.2006.02.037>.
- [94] N.M. Nurazzi, M.R.M. Asyraf, A. Khalina, N. Abdullah, F.A. Sabaruddin, S.H. Kamarudin, S. Ahmad, A.M. Mahat, C.L. Lee, H.A. Aisyah, M.N.F. Norraahim, R.A. Ilyas, M.M. Harussani, M.R. Ishak, S.M. Sapuan, Fabrication, functionalization, and application of carbon nanotube-reinforced polymer composite: An overview, *Polymers.* 13 (2021) 1–44. <https://doi.org/10.3390/polym13071047>.
- [95] S. Gong, W. Cheng, One-Dimensional Nanomaterials for Soft Electronics, *Adv Electron Mater.* 3 (2017) 1600314. <https://doi.org/10.1002/aelm.201600314>.
- [96] S.H. Chae, Y.H. Lee, Carbon nanotubes and graphene towards soft electronics, *Nano Converg.* 1 (2014) 15. <https://doi.org/10.1186/s40580-014-0015-5>.
- [97] Y. Kato, M. Horibe, S. Ata, T. Yamada, K. Hata, Stretchable electromagnetic-interference shielding materials made of a long single-walled carbon-nanotube-

- elastomer composite, *RSC Adv.* 7 (2017) 10841–10847.
<https://doi.org/10.1039/c6ra25350d>.
- [98] B. Yao, W. Hong, T. Chen, Z. Han, X. Xu, R. Hu, J. Hao, C. Li, H. Li, S.E. Perini, M.T. Lanagan, S. Zhang, Q. Wang, H. Wang, Highly Stretchable Polymer Composite with Strain-Enhanced Electromagnetic Interference Shielding Effectiveness, *Advanced Materials*. 32 (2020) 1–7.
<https://doi.org/10.1002/adma.201907499>.
- [99] B. Shin, S. Mondal, M. Lee, S. Kim, Y. Il Huh, C. Nah, Flexible thermoplastic polyurethane-carbon nanotube composites for electromagnetic interference shielding and thermal management, *Chemical Engineering Journal*. 418 (2021) 129282. <https://doi.org/10.1016/j.cej.2021.129282>.
- [100] W.L. Chan, J. Deibel, D.M. Mittleman, Imaging with terahertz radiation, *Reports on Progress in Physics*. 70 (2007) 1325–1379. <https://doi.org/10.1088/0034-4885/70/8/R02>.
- [101] H.A. Hafez, X. Chai, A. Ibrahim, S. Mondal, D. Férachou, X. Ropagnol, T. Ozaki, Intense terahertz radiation and their applications, *Journal of Optics*. 18 (2016).
<https://doi.org/10.1088/2040-8978/18/9/093004>.
- [102] J.H. Son, S.J. Oh, H. Cheon, Potential clinical applications of terahertz radiation, *J Appl Phys*. 125 (2019) 190901. <https://doi.org/10.1063/1.5080205>.
- [103] J. Macutkevicius, D. Seliuta, G. Valusis, R. Adomavicius, P. Kuzhir, A. Paddubskaya, M. Shuba, S. Maksimenko, L. Coderoni, F. Micciulla, I. Sacco, S. Bellucci, Terahertz time domain spectroscopy of epoxy resin composite with various carbon inclusions, *Chem Phys*. 404 (2012) 129–135.
<https://doi.org/10.1016/j.chemphys.2012.02.002>.
- [104] J. Macutkevicius, D. Seliuta, G. Valusis, R. Adomavicius, A. Krotkus, P. Kuzhir, A. Paddubskaya, S. Maksimenko, V. Kuznetsov, I. Mazov, I. Simonova, Multi-walled carbon nanotubes/PMMA composites for THz applications, *Diam Relat Mater*. 25 (2012) 13–18. <https://doi.org/10.1016/j.diamond.2012.02.002>.
- [105] D. Polley, A. Barman, R.K. Mitra, EMI shielding and conductivity of carbon nanotube- polymer composites at terahertz frequency, 39 (2014) 1541–1544.
<https://doi.org/10.1364/OL.39.001541>.
- [106] H.A. Butt, S. V Lomov, I.S. Akhatov, S.G. Abaimov, Self-diagnostic carbon nanocomposites manufactured from industrial epoxy masterbatches, *Compos Struct*. 259 (2020) 113244. <https://doi.org/10.1016/j.compstruct.2020.113244>.
- [107] V. Schroeder, S. Savagatrup, M. He, S. Lin, T.M. Swager, Carbon nanotube chemical sensors, *Chem Rev*. 119 (2019) 599–663.
<https://doi.org/10.1021/acs.chemrev.8b00340>.
- [108] W. Huang, K. Dai, Y. Zhai, H. Liu, P. Zhan, J. Gao, G. Zheng, C. Liu, C. Shen, Flexible and Lightweight Pressure Sensor Based on Carbon Nanotube/Thermoplastic Polyurethane-Aligned Conductive Foam with Superior Compressibility and Stability, *ACS Appl Mater Interfaces*. 9 (2017) 42266–42277.
<https://doi.org/10.1021/acsami.7b16975>.
- [109] M. Ji, H. Deng, D. Yan, X. Li, L. Duan, Q. Fu, Selective localization of multi-walled carbon nanotubes in thermoplastic elastomer blends: An effective method

- for tunable resistivity-strain sensing behavior, *Compos Sci Technol.* 92 (2014) 16–26. <https://doi.org/10.1016/j.compscitech.2013.11.018>.
- [110] H. Liu, J. Gao, W. Huang, K. Dai, G. Zheng, C. Liu, C. Shen, X. Yan, J. Guo, Z. Guo, Electrically conductive strain sensing polyurethane nanocomposites with synergistic carbon nanotubes and graphene bifillers, *Nanoscale.* 8 (2016) 12977–12989. <https://doi.org/10.1039/c6nr02216b>.
- [111] J.F. Christ, N. Aliheidari, A. Ameli, P. Pötschke, 3D printed highly elastic strain sensors of multiwalled carbon nanotube/thermoplastic polyurethane nanocomposites, *Mater Des.* 131 (2017) 394–401. <https://doi.org/10.1016/j.matdes.2017.06.011>.
- [112] J.R. Bautista-Quijano, F. Avilés, J.V. Cauich-Rodriguez, Sensing of large strain using multiwall carbon nanotube/segmented polyurethane composites, *J Appl Polym Sci.* 130 (2013) 375–382. <https://doi.org/10.1002/app.39177>.
- [113] T. Yamada, Y. Hayamizu, Y. Yamamoto, Y. Yomogida, A. Izadi-Najafabadi, D.N. Futaba, K. Hata, A stretchable carbon nanotube strain sensor for human-motion detection, *Nat Nanotechnol.* 6 (2011) 296–301. <https://doi.org/10.1038/nnano.2011.36>.
- [114] K. Suzuki, K. Yataka, Y. Okumiya, S. Sakakibara, K. Sako, H. Mimura, Y. Inoue, Rapid-Response, Widely Stretchable Sensor of Aligned MWCNT/Elastomer Composites for Human Motion Detection, *ACS Sens.* 1 (2016) 817–825. <https://doi.org/10.1021/acssensors.6b00145>.
- [115] I. Kang, M.J. Schulz, J.H. Kim, V. Shanov, D. Shi, A carbon nanotube strain sensor for structural health monitoring, *Smart Mater Struct.* 15 (2006) 737–748. <https://doi.org/10.1088/0964-1726/15/3/009>.
- [116] H. Zhang, E. Bilotti, T. Peijs, The use of carbon nanotubes for damage sensing and structural health monitoring in laminated composites: a review, *Nanocomposites.* 1 (2015) 167–184. <https://doi.org/10.1080/20550324.2015.1113639>.
- [117] G. Mittal, V. Dhand, K.Y. Rhee, S.J. Park, W.R. Lee, A review on carbon nanotubes and graphene as fillers in reinforced polymer nanocomposites, *Journal of Industrial and Engineering Chemistry.* 21 (2015) 11–25. <https://doi.org/10.1016/j.jiec.2014.03.022>.
- [118] Z. Spitalsky, D. Tasis, K. Papagelis, C. Galiotis, Progress in Polymer Science Carbon nanotube – polymer composites: Chemistry , processing , mechanical and electrical properties, *Prog Polym Sci.* 35 (2010) 357–401. <https://doi.org/10.1016/j.progpolymsci.2009.09.003>.
- [119] M.A. Kazakova, V.L. Kuznetsov, N.V. Semikolenova, S.I. Moseenkov, D.V. Krasnikov, M.A. Matsko, A.V. Ishchenko, V.A. Zakharov, A.I. Romanenko, O.B. Anikeeva, E.N. Tkachev, V.I. Suslyaev, V.A. Zhuravlev, K.V. Dorozkin, Comparative study of multiwalled carbon nanotube/polyethylene composites produced via different techniques, *Phys Status Solidi B Basic Res.* 251 (2014) 2437–2443. <https://doi.org/10.1002/pssb.201451194>.
- [120] P. Pötschke, B. Krause, S.T. Buschhorn, U. Köpke, M.T. Müller, T. Villmow, K. Schulte, Improvement of carbon nanotube dispersion in thermoplastic composites

- using a three roll mill at elevated temperatures, *Compos Sci Technol.* 74 (2013) 78–84. <https://doi.org/10.1016/j.compscitech.2012.10.010>.
- [121] F. Du, J.E. Fischer, K.I. Winey, Coagulation Method for Preparing Single-Walled Carbon Nanotube / Poly (methyl methacrylate) Composites and Their Modulus, Electrical Conductivity, and Thermal Stability, *J Polym Sci Part B Polym Phys.* 11 (2003) 3333–3338. <https://doi.org/10.1002/polb.10701>.
- [122] Y. Zheng, Y. Li, K. Dai, M. Liu, K. Zhou, G. Zheng, C. Liu, C. Shen, Conductive thermoplastic polyurethane composites with tunable piezoresistivity by modulating the filler dimensionality for flexible strain sensors, *Compos Part A Appl Sci Manuf.* 101 (2017) 41–49. <https://doi.org/10.1016/j.compositesa.2017.06.003>.
- [123] B. Mensah, H.G. Kim, J.H. Lee, S. Arepalli, C. Nah, Carbon nanotube-reinforced elastomeric nanocomposites: A review, *Int J Smart Nano Mater.* 6 (2015) 211–238. <https://doi.org/10.1080/19475411.2015.1121632>.
- [124] R. Sattar, A. Kausar, M. Siddiq, Advances in thermoplastic polyurethane composites reinforced with carbon nanotubes and carbon nanofibers: A review, *Journal of Plastic Film and Sheeting.* 31 (2015) 186–224. <https://doi.org/10.1177/8756087914535126>.
- [125] Z. Sang, K. Ke, I. Manas-Zloczower, Effect of carbon nanotube morphology on properties in thermoplastic elastomer composites for strain sensors, *Compos Part A Appl Sci Manuf.* 121 (2019) 207–212. <https://doi.org/10.1016/j.compositesa.2019.03.007>.
- [126] M. Dong, C. Wang, H. Liu, C. Liu, C. Shen, J. Zhang, C. Jia, T. Ding, Z. Guo, Enhanced Solid Particle Erosion Properties of Thermoplastic Polyurethane-Carbon Nanotube Nanocomposites, *Macromol Mater Eng.* 304 (2019) 1–11. <https://doi.org/10.1002/mame.201900010>.
- [127] J.H. Du, J. Bai, H.M. Cheng, The present status and key problems of carbon nanotube based polymer composites, *Express Polym Lett.* 1 (2007) 253–273. <https://doi.org/10.3144/expresspolymlett.2007.39>.
- [128] OCSiAl, Single-walled carbon nanotubes: structure, properties, applications, and health & safety. <https://tuball.com/ru/articles/single-walled-carbon-nanotubes.2023>.
- [129] T.B. Nguyen Thi, S. Ata, T. Morimoto, T. Yamada, T. Okazaki, K. Hata, Tailoring the electrically conductive network of injection-molded polymer-carbon nanotube composite at low filler content, *Mater Today Proc.* 40 (2020) 5–8. <https://doi.org/10.1016/j.matpr.2020.02.137>.
- [130] B.J.A. Gutierrez, S. Dul, A. Pegoretti, J. Alvarez-Quintana, L. Fambri, Investigation of the Effects of Multi-Wall and Single-Wall Carbon Nanotubes Concentration on the Properties of ABS Nanocomposites, *C.* 7 (2021) 33. <https://doi.org/10.3390/c7020033>.
- [131] P. Pötschke, A.R. Bhattacharyya, A. Janke, S. Pegel, A. Leonhardt, C. Täschner, M. Ritschel, S. Roth, B. Hornbostel, J. Cech, Melt mixing as method to disperse carbon nanotubes into thermoplastic polymers, *Fullerenes Nanotubes and Carbon Nanostructures.* 13 (2005) 211–224. <https://doi.org/10.1081/FST-200039267>.

- [132] K. Prashantha, J. Soulestin, M.F. Lacrampe, P. Krawczak, G. Dupin, M. Claes, Masterbatch-based multi-walled carbon nanotube filled polypropylene nanocomposites: Assessment of rheological and mechanical properties, *Compos Sci Technol.* 69 (2009) 1756–1763. <https://doi.org/10.1016/j.compscitech.2008.10.005>.
- [133] OCSiAl, Technical data sheet. https://tuball.com/media/documents/files/2021/06/07/TDS_TUBALL_01RW03_ENG_V5.PDF. 2023.
- [134] P.M. Kalachikova, A.E. Goldt, E.M. Khabushev, T.V. Eremin, K.B. Ustinovich, A. Grebenko, O.O. Parenago, T.S. Zatsepin, O.I. Pokrovskiy, E.D. Obratsova, A.G. Nasibulin, Direct injection of SWCNTs into liquid after supercritical nitrogen treatment, *Carbon.* 152 (2019) 66–69. <https://doi.org/10.1016/j.carbon.2019.06.003>.
- [135] K.B. Ustinovich, V.V. Ivanov, Y.M. Tokunov, A.A. Loshkarev, N.I. Saprionova, A.M. Vorobei, O.O. Parenago, M.G. Kiselev, Study of dispersions of carbon nanotubes modified by the method of rapid expansion of supercritical suspensions, *Molecules.* 25 (2020) 4061. <https://doi.org/10.3390/molecules25184061>.
- [136] X. Liu, T. Pichler, T. Pichler, M. Knupfer, M.S. Golden, J. Fink, H. Kataura, Y. Achiba, Detailed analysis of the mean diameter and diameter distribution of single-wall carbon nanotubes from their optical response, *Phys Rev B Condens Matter Mater Phys.* 66 (2002) 454111–454118. <https://doi.org/10.1103/PhysRevB.66.045411>.
- [137] K. Lingam, R. Podila, C. Loebick, P. Chen, P.C. Ke, B. Powell, L. Pfefferle, A.M. Rao, Effect of bundling on the π plasmon energy in sub-nanometer single wall carbon nanotubes, *Carbon.* 49 (2011) 3803–3807. <https://doi.org/10.1016/j.carbon.2011.04.072>.
- [138] M. He, S. Zhang, J. Zhang, Horizontal Single-Walled Carbon Nanotube Arrays: Controlled Synthesis, Characterizations, and Applications, *Chem Rev.* 120 (2020) 12592–12684. <https://doi.org/10.1021/acs.chemrev.0c00395>.
- [139] S.A. Romanov, A.E. Aliev, B.V. Fine, A.S. Anisimov, A.G. Nasibulin, Highly efficient thermophones based on freestanding single-walled carbon nanotube films, *Nanoscale Horiz.* 4 (2019) 1158–1163. <https://doi.org/10.1039/c9nh00164f>.
- [140] J.J.A. Creighton, D.G. Eadont, Ultraviolet-Visible Absorption Spectra of the Colloidal Metallic Elements, *Journal of the Chemical Society, Faraday Transactions.* 87 (1991) 3881–3891. <https://doi.org/10.1039/FT9918703881>.
- [141] L. Guo, Q. Huang, X.Y. Li, S. Yang, Iron nanoparticles: Synthesis and applications in surface enhanced Raman scattering and electrocatalysis, *Physical Chemistry Chemical Physics.* 3 (2001) 1661–1665. <https://doi.org/10.1039/b009951l>.
- [142] L. Calliari, S. Fanchenko, M. Filippi, Plasmon features in electron energy loss spectra from carbon materials, *Carbon.* 45 (2007) 1410–1418. <https://doi.org/10.1016/j.carbon.2007.03.034>.

- [143] A. Jorio, M.A. Pimenta, A.G. Souza Filho, R. Saito, G. Dresselhaus, M.S. Dresselhaus, Characterizing carbon nanotube samples with resonance Raman scattering, *New J Phys.* 5 (2003) 139. <https://doi.org/10.1088/1367-2630/5/1/139>.
- [144] M.S. Dresselhaus, G. Dresselhaus, R. Saito, A. Jorio, Raman spectroscopy of carbon nanotubes, 409 (2005) 47–99. <https://doi.org/10.1016/j.physrep.2004.10.006>.
- [145] S.D.M. Brown, A. Jorio, P. Corio, M.S. Dresselhaus, G. Dresselhaus, R. Saito, K. Kneipp, Origin of the Breit-Wigner-Fano lineshape of the tangential G-band feature of metallic carbon nanotubes, *Phys Rev B Condens Matter Mater Phys.* 63 (2001) 1–8. <https://doi.org/10.1103/PhysRevB.63.155414>.
- [146] A.S. Anisimov, A.G. Nasibulin, H. Jiang, P. Launois, J. Cambedouzou, S.D. Shandakov, E.I. Kauppinen, Mechanistic investigations of single-walled carbon nanotube synthesis by ferrocene vapor decomposition in carbon monoxide, *Carbon.* 48 (2010) 380–388. <https://doi.org/10.1016/j.carbon.2009.09.040>.
- [147] A. Kaskela, P. Laiho, N. Fukaya, K. Mustonen, T. Susi, H. Jiang, N. Houbenov, Y. Ohno, E.I. Kauppinen, Highly individual SWCNTs for high performance thin film electronics, *Carbon.* 103 (2016) 228–234. <https://doi.org/10.1016/j.carbon.2016.02.099>.
- [148] A. Moisala, A.G. Nasibulin, I. Kauppinen, The role of metal nanoparticles in the catalytic production of single-walled carbon nanotubes-a review, *Journal of Physics: Condensed Matter.* 15 (2003) S3011. <https://doi.org/10.1088/0953-8984/15/42/003>.
- [149] A.G. Nasibulin, P.V. Pikhitsa, H. Jiang, E.I. Kauppinen, Correlation between catalyst particle and single-walled carbon nanotube diameters, *Carbon.* 43 (2005) 2251–2257. <https://doi.org/10.1016/j.carbon.2005.03.048>.
- [150] M.C. Diaz, H. Jiang, E. Kauppinen, R. Sharma, P.B. Balbuena, Can Single-Walled Carbon Nanotube Diameter Be Defined by Catalyst Particle Diameter?, *Journal of Physical Chemistry C.* 123 (2019) 30305–30317. <https://doi.org/10.1021/acs.jpcc.9b07724>.
- [151] P. Kulkarni, P.A. (Paul A. Baron, Klaus. Willeke, *Aerosol measurement: principles, techniques, and applications*, Wiley, 2011.
- [152] D.R. Chen, M. Chitranshi, M. Schulz, V. Shanov, A Review of Three Major Factors Controlling Carbon Nanotubes Synthesis from the Floating Catalyst Chemical Vapor Deposition, *Nano Life.* 09 (2019) 1930002. <https://doi.org/10.1142/s1793984419300024>.
- [153] A.R. Bogdanova, D.V. Krasnikov, A.G. Nasibulin, The role of sulfur in the CVD carbon nanotube synthesis, *Carbon.* 210 (2023) 118051. <https://doi.org/10.1016/j.carbon.2023.118051>.
- [154] K. Mustonen, P. Laiho, A. Kaskela, T. Susi, A.G. Nasibulin, E.I. Kauppinen, Uncovering the ultimate performance of single-walled carbon nanotube films as transparent conductors, *Appl Phys Lett.* 107 (2015) 143113. <https://doi.org/10.1063/1.4932942>.
- [155] O. Reynaud, A.G. Nasibulin, A.S. Anisimov, I.V. Anoshkin, H. Jiang, E.I. Kauppinen, Aerosol feeding of catalyst precursor for CNT synthesis and highly

- conductive and transparent film fabrication, *Chemical Engineering Journal*. 255 (2014) 134–140. <https://doi.org/10.1016/j.cej.2014.06.082>.
- [156] J.S. Bulmer, A. Kaniyoor, T. Gspann, J. Mizen, J. Ryley, P. Kiley, G. Ratering, W. Sparreboom, G. Bauhuis, T. Stehr, D. Oudejans, M. Sparkes, B. O'Neill, J.A. Elliott, Forecasting continuous carbon nanotube production in the floating catalyst environment, *Chemical Engineering Journal*. 390 (2020) 124497. <https://doi.org/10.1016/j.cej.2020.124497>.
- [157] Y. Ma, A.B. Dichiara, D. He, L. Zimmer, J. Bai, Control of product nature and morphology by adjusting the hydrogen content in a continuous chemical vapor deposition process for carbon nanotube synthesis, *Carbon*. 107 (2016) 171–179. <https://doi.org/10.1016/j.carbon.2016.05.060>.
- [158] J. Lei, K.V. Bets, E.S. Penev, B.I. Yakobson, Floating Fe Catalyst Formation and Effects of Hydrogen Environment in the Growth of Carbon Nanotubes, *J Phys Chem Lett*. 14 (2023) 4266–4272. <https://doi.org/10.1021/acs.jpcclett.3c00716>.
- [159] Q. Liu, W. Ren, Z.G. Chen, D.W. Wang, B. Liu, B. Yu, F. Li, H. Cong, H.M. Cheng, Diameter-selective growth of single-walled carbon nanotubes with high quality by floating catalyst method, *ACS Nano*. 2 (2008) 1722–1728. <https://doi.org/10.1021/nn8003394>.
- [160] P.X. Hou, W.S. Li, S.Y. Zhao, G.X. Li, C. Shi, C. Liu, H.M. Cheng, Preparation of metallic single-wall carbon nanotubes by selective etching, *ACS Nano*. 8 (2014) 7156–7162. <https://doi.org/10.1021/nn502120k>.
- [161] A.R. Bogdanova, D.V. Krasnikov, E.M. Khabushev, J.A. Ramirez B., Y.E. Matyushkin, A.G. Nasibulin, Role of Hydrogen in Ethylene-Based Synthesis of Single-Walled Carbon Nanotubes, *Nanomaterials*. 13 (2023) 1504. <https://doi.org/10.3390/nano13091504>.
- [162] A.M. Shetty, G.M.H. Wilkins, J. Nanda, M.J. Solomon, Multiangle depolarized dynamic light scattering of short functionalized single-walled carbon nanotubes, *Journal of Physical Chemistry C*. 113 (2009) 7129–7133. <https://doi.org/10.1021/jp900731q>.
- [163] S. Badaire, P. Poulin, M. Maugey, C. Zakri, In situ measurements of nanotube dimensions in suspensions by depolarized dynamic light scattering, *Langmuir*. 20 (2004) 10367–10370. <https://doi.org/10.1021/la049096r>.
- [164] D.E. Tsentalovich, A.W.K. Ma, J.A. Lee, N. Behabtu, E.A. Bengio, A. Choi, J. Hao, Y. Luo, R.J. Headrick, M.J. Green, Y. Talmon, M. Pasquali, Relationship of Extensional Viscosity and Liquid Crystalline Transition to Length Distribution in Carbon Nanotube Solutions, *Macromolecules*. 49 (2016) 681–689. <https://doi.org/10.1021/acs.macromol.5b02054>.
- [165] P. Karlsen, M.V. Shuba, C. Beckerleg, D.I. Yuko, P.P. Kuzhir, S.A. Maksimenko, V. Ksenevich, H. Viet, A.G. Nasibulin, R. Tenne, E. Hendry, Influence of nanotube length and density on the plasmonic terahertz response of single-walled carbon nanotubes, *J Phys D Appl Phys*. 51 (2018) 014003. <https://doi.org/10.1088/1361-6463/aa96ef>.

- [166] G. Chen, R.C. Davis, H. Kimura, S. Sakurai, M. Yumura, D.N. Futaba, K. Hata, The relationship between the growth rate and the lifetime in carbon nanotube synthesis, *Nanoscale*. 7 (2015) 8873–8878. <https://doi.org/10.1039/c5nr01125f>.
- [167] C.T. Wirth, B.C. Bayer, A.D. Gamalski, S. Esconjauregui, R.S. Weatherup, C. Ducati, C. Baetz, J. Robertson, S. Hofmann, The phase of iron catalyst nanoparticles during carbon nanotube growth, *Chemistry of Materials*. 24 (2012) 4633–4640. <https://doi.org/10.1021/cm301402g>.
- [168] J.S. Bulmer, T.S. Gspann, J.S. Barnard, J.A. Elliott, Chirality-independent characteristic crystal length in carbon nanotube textiles measured by Raman spectroscopy, *Carbon*. 115 (2017) 672–680. <https://doi.org/10.1016/j.carbon.2017.01.044>.
- [169] L.D. Tijning, C.H. Park, W.L. Choi, M.T.G. Ruelo, A. Amarjargal, H.R. Pant, I.T. Im, C.S. Kim, Characterization and mechanical performance comparison of multiwalled carbon nanotube/polyurethane composites fabricated by electrospinning and solution casting, *Compos B Eng*. 44 (2013) 613–619. <https://doi.org/10.1016/j.compositesb.2012.02.015>.
- [170] W. Chen, X. Tao, Y. Liu, Carbon nanotube-reinforced polyurethane composite fibers, *Compos Sci Technol*. 66 (2006) 3029–3034. <https://doi.org/10.1016/j.compscitech.2006.01.024>.
- [171] B.E. Kilbride, J.N. Coleman, J. Fraysse, P. Fournet, Experimental observation of scaling laws for alternating current and direct current conductivity in polymer-carbon nanotube composite thin films, *J Appl Phys*. 92 (2002) 4024-4030. <https://doi.org/10.1063/1.1506397>.
- [172] S. Geng, P. Wang, T. Ding, Impedance characteristics and electrical modelling of multi-walled carbon nanotube/silicone rubber composites, *Compos Sci Technol*. 72 (2011) 36–40. <https://doi.org/10.1016/j.compscitech.2011.08.021>.
- [173] J.O. Aguilar, J.R. Bautista-Quijano, F. Avilés, Influence of carbon nanotube clustering on the electrical conductivity of polymer composite films, *Express Polym Lett*. 4 (2010) 292–299. <https://doi.org/10.3144/expresspolymlett.2010.37>.
- [174] N. Hu, Z. Masuda, C. Yan, G. Yamamoto, H. Fukunaga, T. Hashida, The electrical properties of polymer nanocomposites with carbon nanotube fillers, *Nanotechnology*. 19 (2008) 215701. <https://doi.org/10.1088/0957-4484/19/21/215701>.
- [175] H. Xia, M. Song, Preparation and characterization of polyurethane-carbon nanotube composites, *Soft Matter*. 1 (2005) 386–394. <https://doi.org/10.1039/b509038e>.
- [176] H. Koerner, W. Liu, M. Alexander, P. Mirau, H. Dowty, R.A. Vaia, Deformation-morphology correlations in electrically conductive carbon nanotube - Thermoplastic polyurethane nanocomposites, *Polymer*. 46 (2005) 4405–4420. <https://doi.org/10.1016/j.polymer.2005.02.025>.
- [177] R. Zhang, A. Dowden, H. Deng, M. Baxendale, T. Peijs, Conductive network formation in the melt of carbon nanotube/thermoplastic polyurethane composite, *Compos Sci Technol*. 69 (2009) 1499–1504. <https://doi.org/10.1016/j.compscitech.2008.11.039>.

- [178] R. Zhang, H. Deng, R. Valenca, J. Jin, Q. Fu, E. Bilotti, T. Peijs, Strain sensing behaviour of elastomeric composite films containing carbon nanotubes under cyclic loading, *Compos Sci Technol.* 74 (2013) 1–5. <https://doi.org/10.1016/j.compscitech.2012.09.016>.
- [179] Z. Sang, K. Ke, I. Manas-Zloczower, Interface Design Strategy for the Fabrication of Highly Stretchable Strain Sensors, *ACS Appl Mater Interfaces.* 10 (2018) 36483–36492. <https://doi.org/10.1021/acsami.8b14573>.
- [180] C.J. Hohimer, G. Petrossian, A. Ameli, C. Mo, P. Pötschke, 3D printed conductive thermoplastic polyurethane/carbon nanotube composites for capacitive and piezoresistive sensing in soft pneumatic actuators, *Addit Manuf.* 34 (2020) 101281. <https://doi.org/10.1016/j.addma.2020.101281>.
- [181] NIST Chemistry WebBook Database. <https://webbook.nist.gov>, 2023.
- [182] A.T.D. Butland, R.J. Maddison, The specific heat of graphite: an evaluation of measurements, *J Nucl Mater.* 49 (1973/74) 45-56. [https://doi.org/10.1016/0022-3115\(73\)90060-3](https://doi.org/10.1016/0022-3115(73)90060-3).

Appendices

Appendix 1. Bundling degree dependency on the number of nanotubes and residence time

Bundle diameter, d_b , is connected to the bundling degree according to equation

(31):

$$d_b = db^{\frac{1}{2}} = d \left(\frac{N}{N_b} \right)^{\frac{1}{2}}. \quad (\text{A1})$$

Thus, the coagulation K coefficient is dependent on time t and aerosol concentration $N(t)$

[151]:

$$\begin{aligned} K &= \frac{4kTC_c}{3\mu} \sim C_c \sim Kn \sim \frac{\lambda_{mean\ free}}{d_m} \sim d_m^{-1} \sim L^{-\frac{1}{3}} d_b^{-\frac{2}{3}} \sim L^{-\frac{1}{3}} N(t)^{-\frac{1}{3}} \sim L^{-\frac{1}{3}} N(t)^{-\frac{1}{3}} \sim \\ &\sim t^{-\frac{\lambda}{3}} N(t)^{-\frac{1}{3}} = \alpha t^{-\frac{\lambda}{3}} N(t)^{-\frac{1}{3}}, \end{aligned} \quad (\text{A2})$$

where C_c is the Cunningham slip correction factor, μ is gas viscosity, $\lambda_{mean\ free}$ is mean free path, and α is a proportionality coefficient. Thus, the following differential equation is derived:

$$\frac{dN(t)}{dt} = -\alpha t^{-\frac{\lambda}{3}} N(t)^{-\frac{1}{3}} N(t)^2 = -\alpha t^{-\frac{\lambda}{3}} N(t)^{\frac{5}{3}}. \quad (\text{A3})$$

An integral of this differential equation leads to the dependency of the bundling degree on the number of formed SWCNTs and residence time (considering the following initial conditions $N(0) = N$; $N(\tau) = N_b$):

$$N(t) = \frac{N(0)}{\left(1 + \frac{2\alpha}{3-\lambda} \cdot N(0)^{\frac{2}{3}} \cdot t^{\frac{3-\lambda}{3}}\right)^{\frac{3}{2}}},$$

$$b = \frac{N}{N_b} = N \left/ \frac{N}{\left(1 + \frac{2\alpha}{3-\lambda} \cdot N^{\frac{2}{3}} \cdot \tau^{\frac{3-\lambda}{3}}\right)^{\frac{3}{2}}}\right. = \left(1 + \frac{2\alpha}{3-\lambda} \cdot N^{\frac{2}{3}} \cdot \tau^{\frac{3-\lambda}{3}}\right)^{\frac{3}{2}} \sim N \cdot \tau^{\frac{3-\lambda}{2}}. \quad (\text{A4})$$

Appendix 2. Thermodynamic calculations for CO/H₂ atmosphere.

To estimate equilibrium concentrations of the products of reactions (16) – (17), the correlation between change in Gibbs free energy $\Delta_r G^0$ and equilibrium constant K_{eq} was used:

$$K_{eq} = \exp\left(-\frac{\Delta_r G^0}{RT}\right). \quad (\text{A5})$$

Meanwhile, $\Delta_r G^0$ can be expressed as a difference between the free energies of the product $\Delta_f G_{product}$ and reactant $\Delta_f G_{reactant}$ formation:

$$\Delta_r G^0 = \Delta_f G_{product}(T) - \Delta_f G_{reactant}(T), \quad (\text{A6})$$

where free energy of the reagent formation can be derived using the enthalpy $\Delta_f H$ and entropy $\Delta_f S$ formation:

$$\Delta_f G(T) = \Delta_f H(T) - T\Delta_f S(T), \quad (\text{A7})$$

which temperature dependency, in turn, can be derived using heat capacity C_p :

$$\Delta_f H(T) = \Delta_f H(298 \text{ K}) + \int_{298}^T C_p(T) dT, \quad (\text{A8})$$

$$\Delta_f S(T) = \Delta_f S(298 \text{ K}) + \int_{298}^T \frac{C_p(T)}{T} dT, \quad (\text{A9})$$

where $\Delta_f H(298 \text{ K})$ and $\Delta_f S(298 \text{ K})$ are standard enthalpy and entropy, respectively. With the use of polynomial heat capacity dependency on reduced temperature $\tau = \frac{T}{1000} \text{ (K)}$

(Shomate equation):

$$C_p = A + B\tau + C\tau^2 + D\tau^3 + \frac{E}{\tau^2}, \quad (\text{A10})$$

and the equations (S4) and (S5), temperature-dependent $\Delta_f H(\tau)$ and $\Delta_f S(\tau)$ can be derived:

$$\Delta_f H(\tau) = A\tau + \frac{B\tau^2}{2} + \frac{C\tau^3}{3} + \frac{D\tau^4}{4} - \frac{E}{\tau} + F, \quad (\text{A11})$$

$$\Delta_f S(\tau) = A \ln \tau + B\tau + \frac{C\tau^2}{2} + \frac{D\tau^3}{3} - \frac{E}{2\tau^2} + G, \quad (\text{A12})$$

where the coefficients used can be found in the NIST database (**Table A1**, [182]). The resulting $\Delta_f G(T)$ -vs- T curves for reactions (16) – (18) are plotted in **Figure 12a**.

Table A1. Coefficients from the Shomate equation for the reagents from reactions (16) – (18) (taken from the NIST database [182]; empirical coefficients for C (graphite) were taken from [183]).

Reagent	A	B	C	D	E	F	G
CO (<1300 K)	25.56759	6.09613	4.054656	-2.6713	0.131021	-118.009	227.3665
CO (>1300 K)	35.1507	1.300095	-0.20592	0.01355	-3.28278	-127.838	231.712
CO ₂ (<1200 K)	24.99735	55.18696	-33.6914	7.948387	-0.13664	-403.608	228.2431

CO ₂ (>1200 K)	58.16639	2.720074	-0.49229	0.038844	-6.44729	-425.919	263.6125
C (graphite)	0.538657	9.11E-06	-90.2725	-43449.3	1.59E07	- 1.44E+09	5.74
H ₂ (<1000 K)	33.06618	-11.3634	11.43282	-2.77287	-0.15856	-9.9808	172.708
H ₂ (>1000 K)	18.56308	12.25736	-2.85979	0.268238	1.97799	-1.14744	156.2881
H ₂ O	30.092	6.832514	6.793435	-2.53448	0.082139	-250.881	223.3967
CH ₄ (<1300 K)	-0.70303	108.4773	-42.5216	5.862788	0.678565	-76.8438	158.7163
CH ₄ (>1300 K)	85.81217	11.26467	-2.11415	0.13819	-26.4222	-153.533	224.4143

The quotients of reactions (16) – (18) (Q_1 , Q_2 , Q_3) are calculated according to the equations:

$$Q_1 = \frac{\{CO_2\}}{\{CO\}^2}, \quad (A13)$$

$$Q_2 = \frac{\{H_2O\}}{\{CO\}\{H_2\}}, \quad (A14)$$

$$Q_3 = \frac{\{CH_4\}}{\{H_2\}^2}, \quad (A15)$$

where actual concentrations of the reagents are denoted as reagents in curly brackets. At the equilibrium, the quotients turn to equilibrium constants (K_1 , K_2 , K_3). Calculated equilibrium constants allow determining equilibrium concentrations of the products of reactions (16) - (18) (denoted as reagents in square brackets): CO₂, H₂O, and CH₄ depending on the H₂ concentration:

$$K_1 = \frac{[CO_2]}{[CO]^2}, \quad (A16)$$

$$K_2 = \frac{[H_2O]}{[CO][H_2]}, \quad (A17)$$

$$K_3 = \frac{[CH_4]}{[H_2]^2}. \quad (A18)$$

Taking into account that the reactor is kept under atmospheric pressure and describing equilibrium concentration in vol%, the total concentration of CO and H₂ equals 1 (100 vol%). Thus, considering the initial concentration of the introduced hydrogen as a parameter a ($[H_2] \equiv a$), CO concentration is determined by a ($[CO] \equiv 1 - a$), the products (their equilibrium concentrations) taken as sought variables (extents of reaction) ($[CO_2] \equiv x$, $[H_2O] \equiv y$, $[CH_4] \equiv z$), and taking into account the consumption of the reagents (CO and H₂), we can obtain the system of equations:

$$\left\{ \begin{array}{l} K_1 = \frac{x}{(1 - a - 2x - y)^2} \\ K_2 = \frac{y}{(1 - a - 2x - y)(a - y - 2z)} \\ K_3 = \frac{z}{(a - y - 2z)^2} \end{array} \right. \quad (A19)$$

where equilibrium constants are known for the given temperature. The system of equations (A19) can be solved numerically for parameter a in the range of (0,1). **Figure A1** represents the results of equation (A19) solution for both temperatures: 880 °C and 1000 °C.

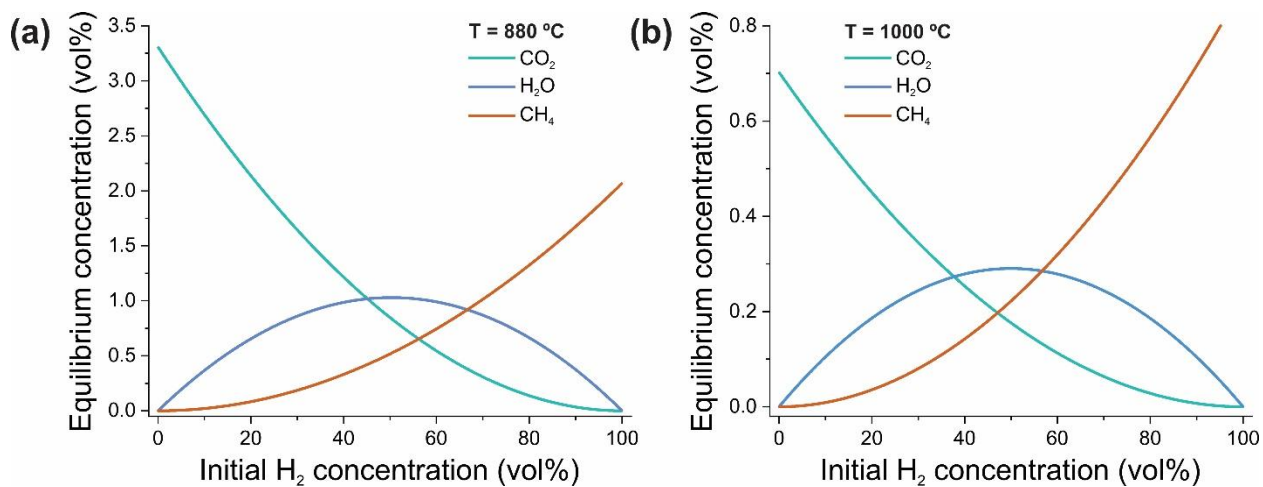


Figure S1. Calculated equilibrium concentrations of CO₂, H₂O, and CH₄ depending on the initial H₂ concentration introduced at (a) 880 °C and (b) 1000 °C.

Appendix 3. Effects of nitrogen and residence time in H₂-assisted aerosol

CVD nanotube synthesis.

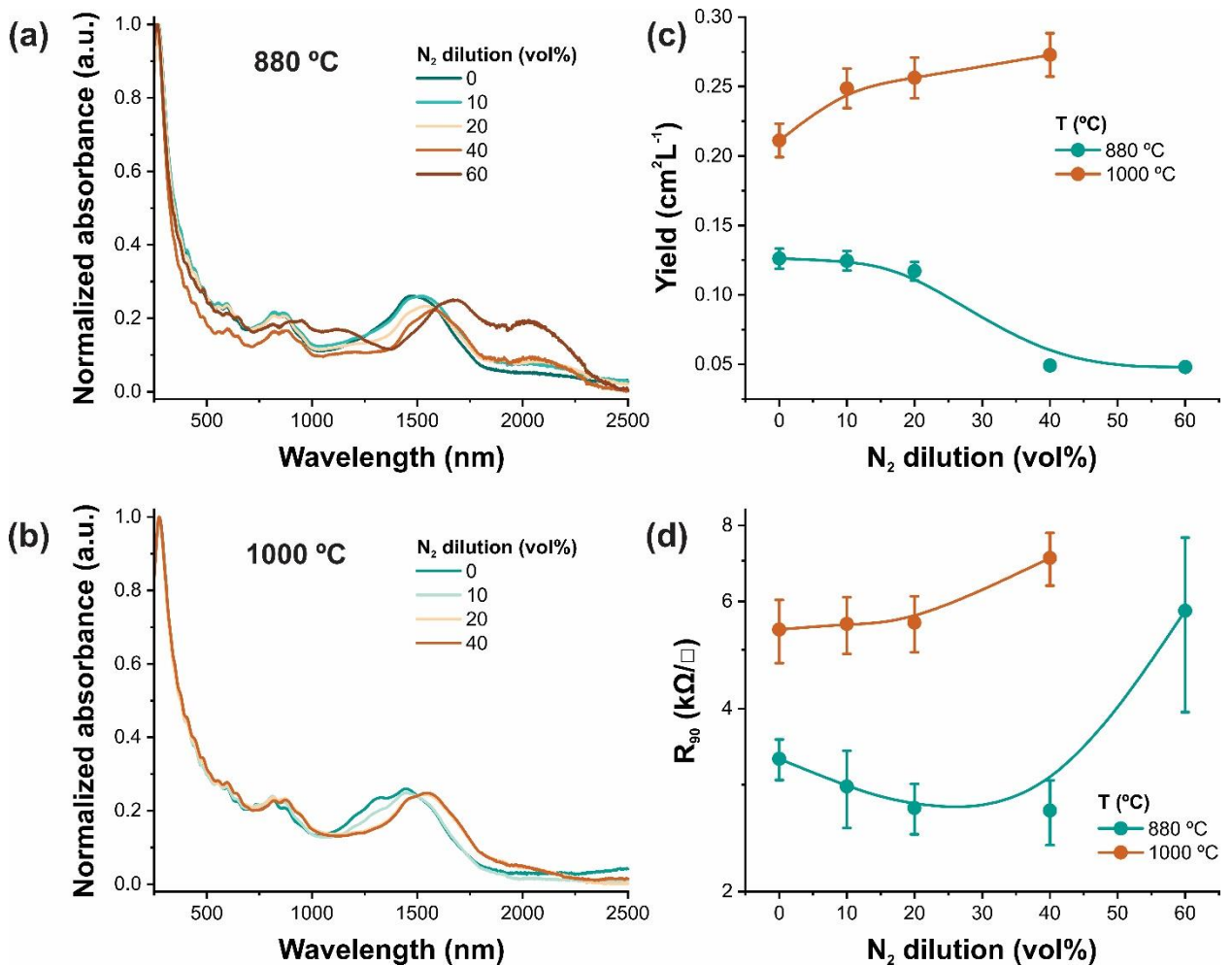


Figure A2. UV-vis-NIR spectra of the SWCNT films synthesized with N₂ dilution (concentration is shown in the legend) at (a) 880 °C and (b) 1000 °C; Dependencies of the yield (c) and R₉₀ (d) on N₂ concentration at 880 °C and 1000 °C.

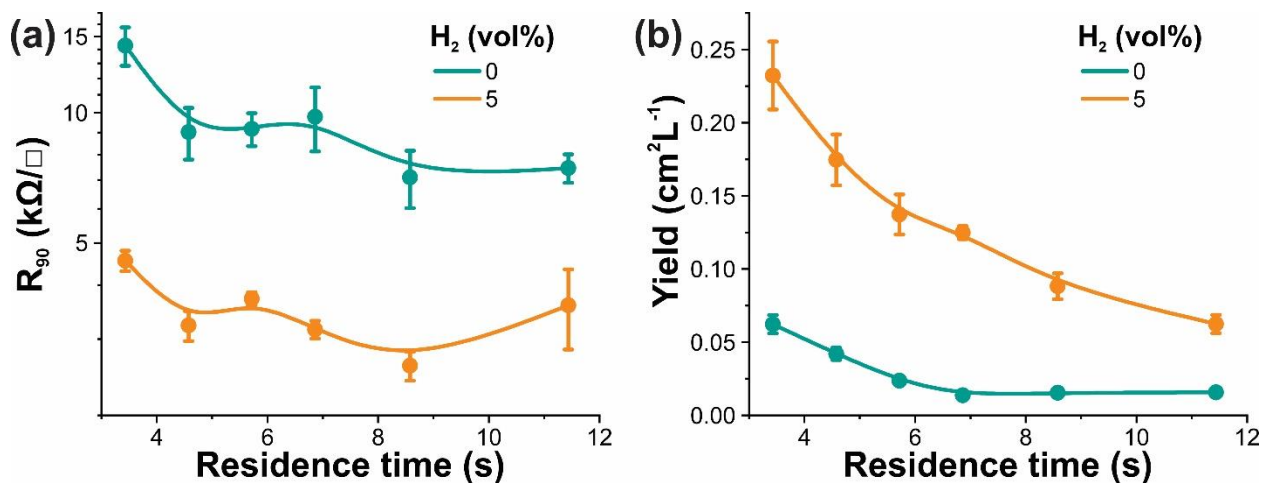


Figure A3. (a) R_{90} and (b) yield dependencies on residence time without and with H_2 introduction (at 5 vol%) at 1000 °C.

Appendix 4. Supporting figures for nanotube kinetics evaluation study

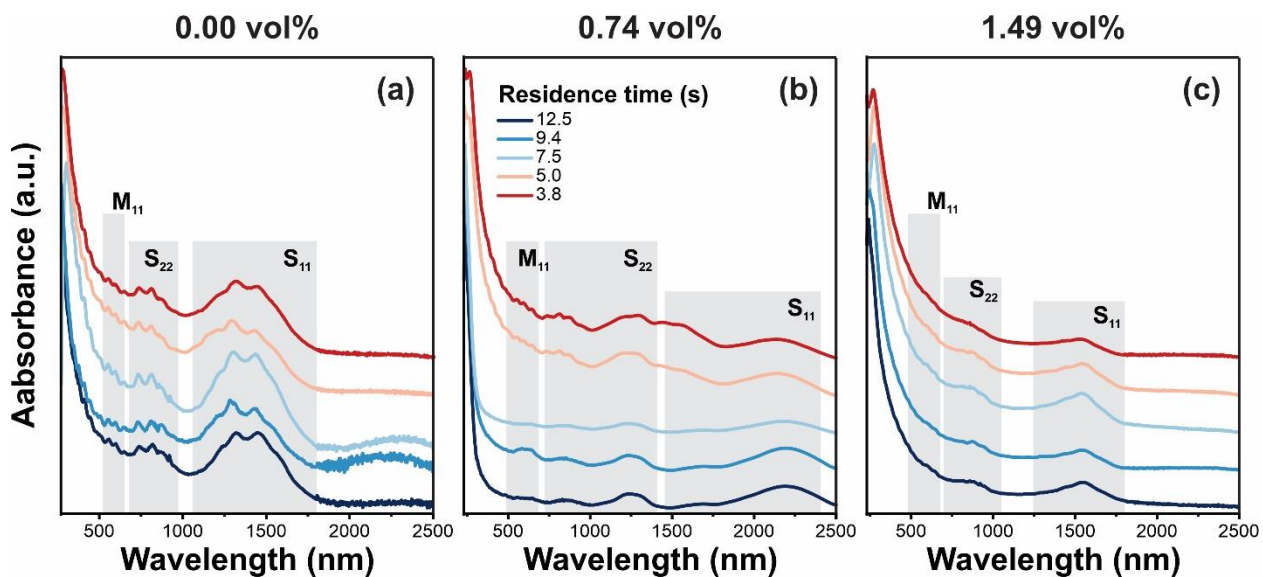


Figure A4. UV-vis-NIR (optical absorbance) spectra with highlighted transition peaks of SWCNTs synthesized at different residence times (shown in the legend) and CO_2 concentrations: (a) 0.00 vol%, (b) 0.74 vol%, (c) 1.49 vol%.

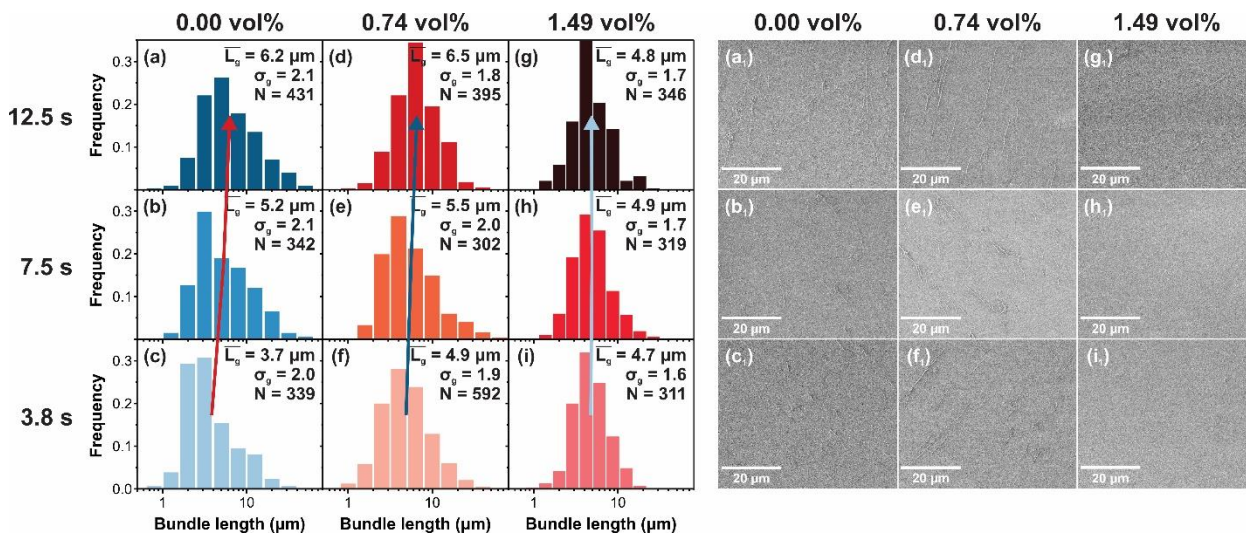


Figure A5. Bundle length distribution histograms of SWCNTs synthesized at different residence times (image rows) and CO₂ concentrations (image columns) indicated in figure: **(a)-(c)** 0.00 vol%, **(d)-(f)** 0.74 vol%, **(g)-(i)** 1.49 vol%. Arrows indicate a shift in geometric mean length with τ . **(a1-i1)** Corresponding typical SEM images of SWCNT bundles on Si/SiO₂ substrate.

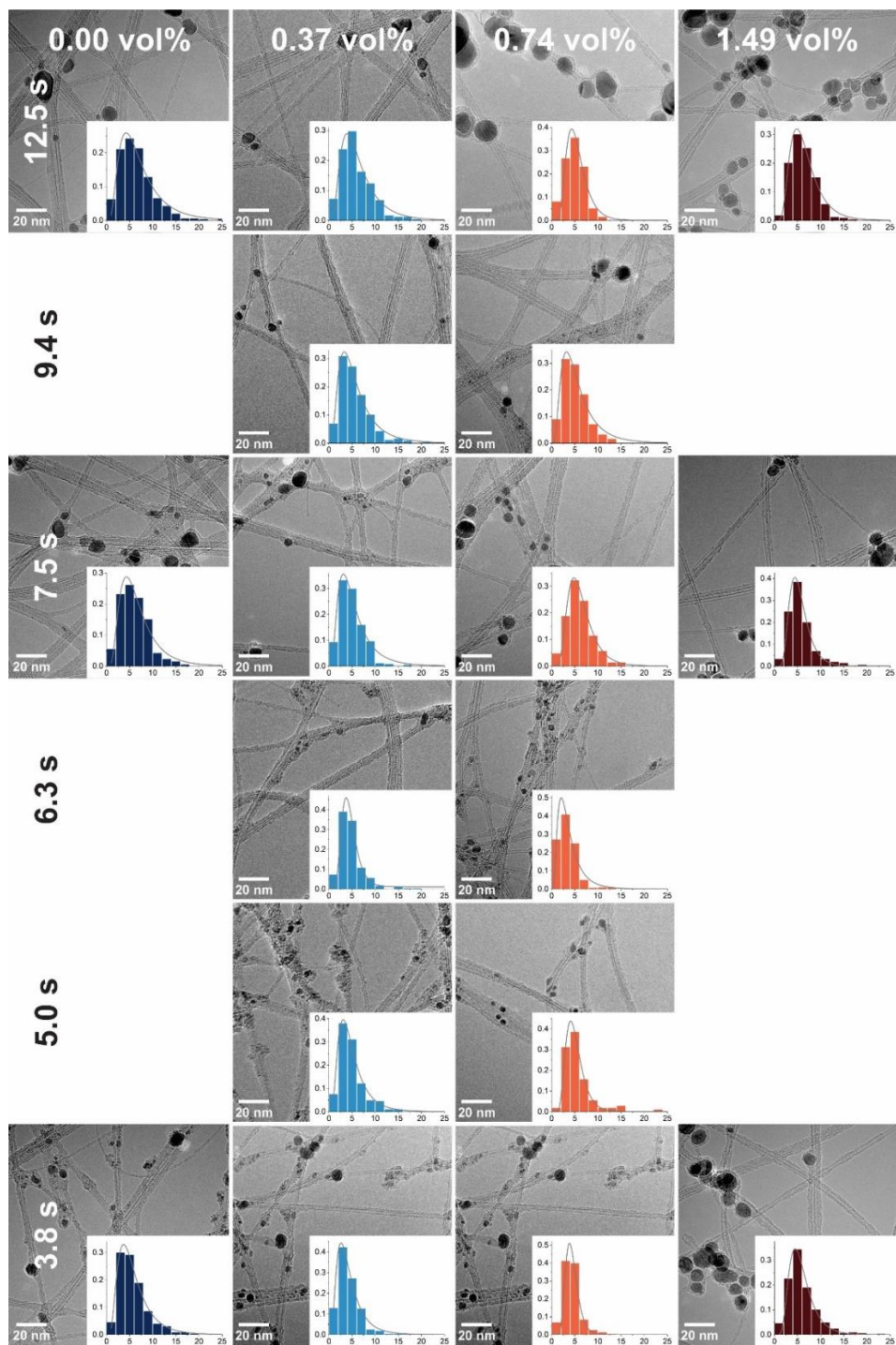


Figure A6. Typical TEM images of SWCNTs synthesized at different τ and $c(\text{CO}_2)$ (see indicated rows and columns, respectively) with corresponding bundle diameter distribution histograms.

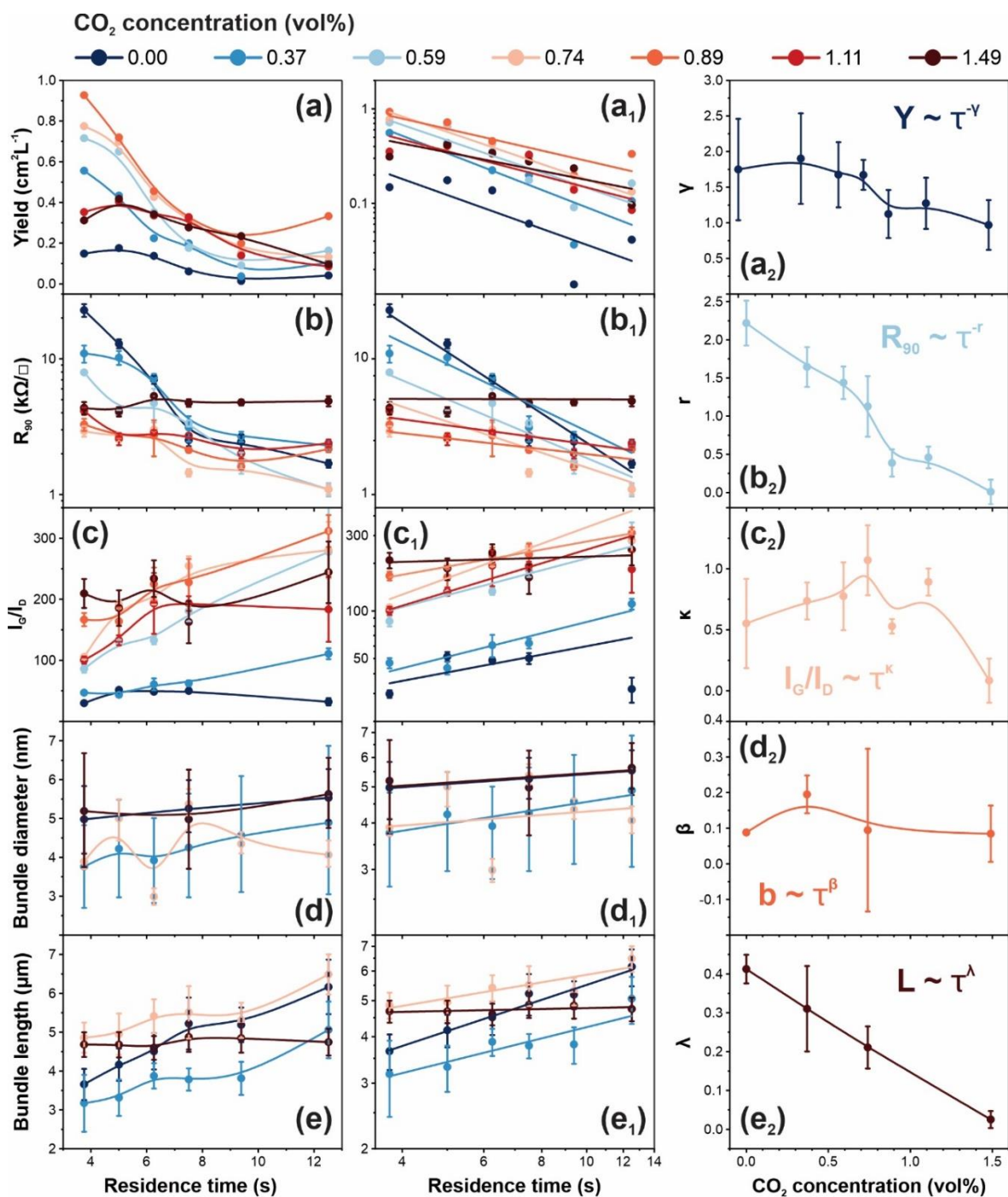


Figure A7. Dependencies of (a) yield, (b) R_{90} , (c) I_G/I_D , (d) bundle diameter, and (e) bundle length on residence time at different $c(\text{CO}_2)$ (shown in the legend at the top of the image); (a₁-e₁) the same dependencies plotted in log-log scales. Dependencies of exponents in scaling laws of (a₂) γ (Y -vs- τ), (b₂) r (σ_{90} -vs- τ), (c₂) κ (I_G/I_D -vs- τ), and (d₂) β (b -vs- τ), (e₂) λ (L -vs- τ) on $c(\text{CO}_2)$.

Table A2. The overall trends of residence time influence on the SWCNT parameters at different CO₂ concentrations (numbers of arrows qualitatively illustrate evolution rates with τ (parameters are derived from fitting the results)).

$c(\text{CO}_2)$	$r (R_{90})$	γ (Yield)	λ (length)	β (bundling)	κ (I_G/I_D)
0.00	2.22 ± 0.29	1.75 ± 0.71	0.41 ± 0.04	0.19 ± 0.05	0.55 ± 0.37
0.37	1.64 ± 0.26	1.90 ± 0.64	0.31 ± 0.11	0.09 ± 0.23	0.74 ± 0.15
0.74	1.13 ± 0.40	1.67 ± 0.21	0.21 ± 0.05	0.09 ± 0.01	1.07 ± 0.29
1.49	0.008 ± 0.16	0.97 ± 0.35	0.03 ± 0.02	0.08 ± 0.08	0.08 ± 0.18

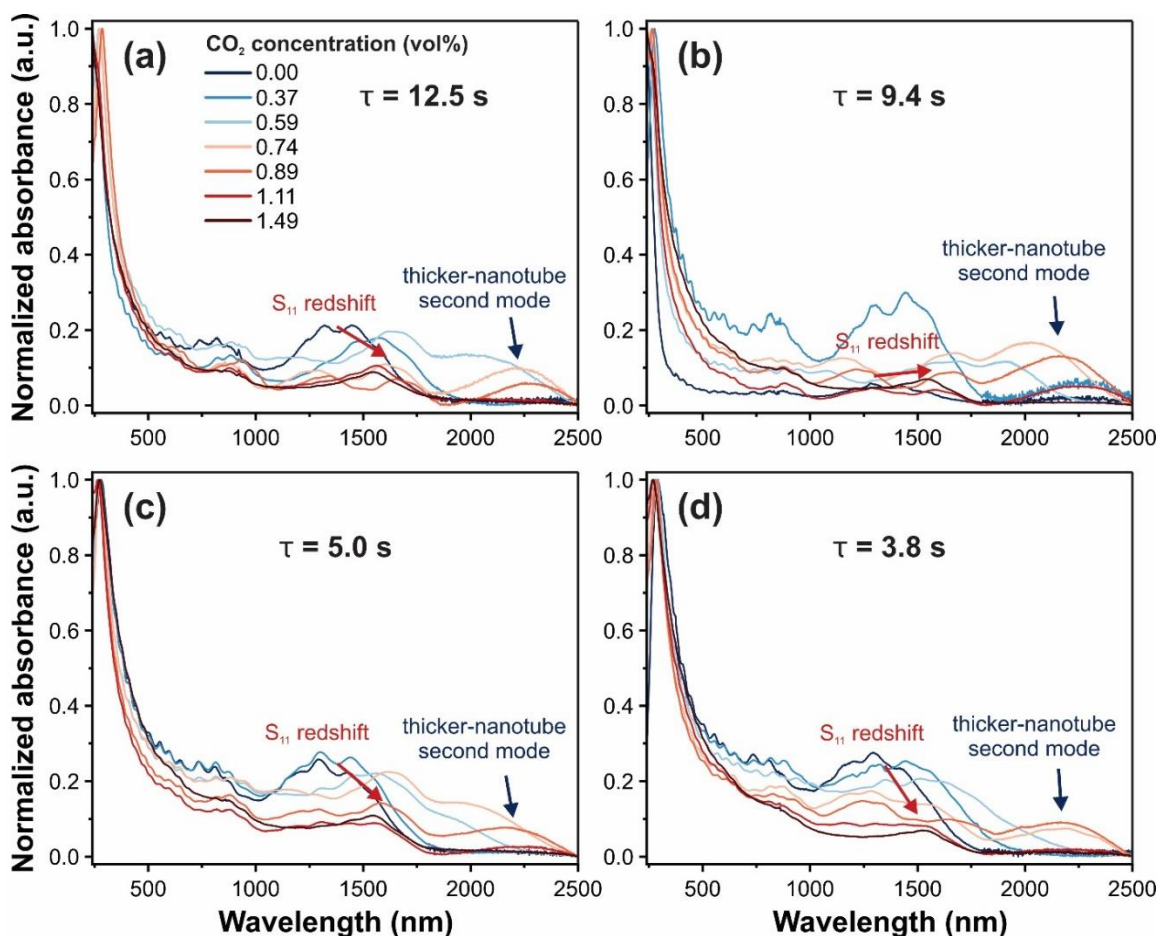


Figure A8. UV-vis-NIR spectra of the SWCNT films synthesized at 880 °C at different $c(\text{CO}_2)$ (shown in the legend) and at different residence times: (a) 12.5 s, (b) 9.5 s, (c) 5.0 s, (d) 3.8 s with the highlighted S₁₁ redshift and the formation of the second mode of thicker SWCNTs.

Appendix 5. Supporting figures for the investigation of SWCNT/polymer nanocomposites

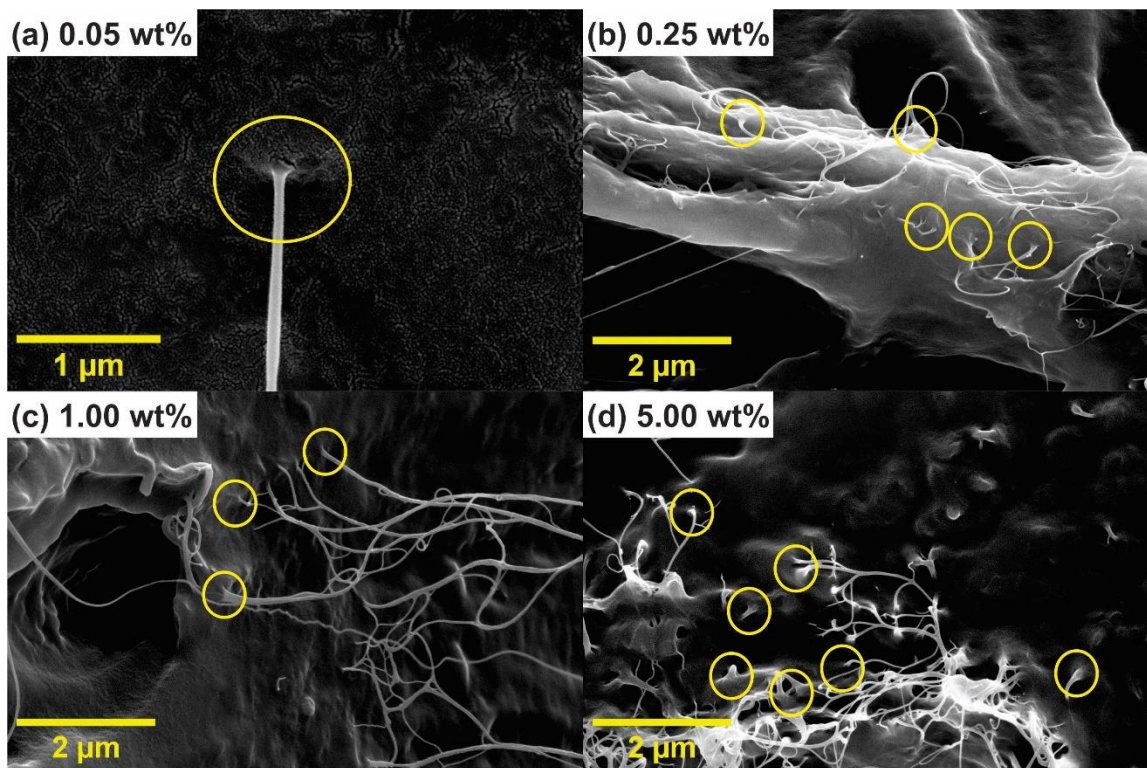


Figure A9. Additional SEM images of SWCNT/TPU nanocomposites fabricated with different concentrations of SWCNTs (indicated in the images) with highlighted regions of SWCNT bundles approaching the TPU surface indicating high TPU wetting.